Optical spectroscopy and fluorescence imaging for cancer diagnostics

Svenmarker, Pontus

2012

Optical spectroscopy and fluorescence imaging for cancer diagnostics

Pontus Svenmarker

Doctoral Thesis
2012

Lund University

Optical spectroscopy and fluorescence imaging for cancer diagnostics

Printed in Sweden by Media-Tryck, Lund, March 2012

Division of Atomic Physics
Department of Physics
Faculty of Engineering, LTH
Lund University
P.O. Box 118
SE–221 00 Lund
Sweden

http://www.atomic.physics.lu.se/
http://www.atomic.physics.lu.se/biophotonics

ISSN 0281-2762
Lund Reports on Atomic Physics, LRAP-453

ISBN 978-91-7473-294-8

Abstract

This work presents optical methods for diagnosing cancer. A complementary method for diagnosing eye cancer was investigated using a technique developed within this work named transscleral optical spectroscopy (TOS). Furthermore, nano-sized crystals doped with lanthanides were exploited as probes for fluorescence imaging with direct applications to preclinical cancer research.

Almost all intraocular malignancies can today be correctly diagnosed using techniques like ophthalmoscopy, ultrasonography and fluorescein angiography. Even with the rich flora of tools available, some tumors present non-typical behaviors and are difficult to diagnose. As a complementary diagnostic method, TOS was developed, which exploits the natural optical contrast in tissue for diagnosis. The method is particularly sensitive in identifying physiological changes characteristic of tumors, *i.e.* tissue hemoglobin (total, oxy- , and deoxy- forms), oxygen saturation, blood volume fraction, water content, melanin content and cellular structure. In a series of experiments on porcine eyes, TOS was successful in quantifying the blood and melanin content of tumor-phantoms placed in the choroid. It was also showed that TOS measurements did not cause any visible damage to the sclera, resulted in a significant temperature rise, or led to an unacceptable intra ocular pressure elevation. In further experiments on enucleated human eyes with a predetermined melanoma diagnosis, TOS measurements were found to correlated well with the degree of pigmentation in the melanoma. To summarize, TOS offers a tool to probe the physiology of intraocular tumor, which can be used in a complementary diagnosis.

Fluorescence imaging is a versatile tool for studying biology on the nanometer to centimeter length-scale through labeling tissue with fluorescent probes to induce the desired contrast. In this work, upconverting nanoparticles (UPNs) were evaluated as fluorescent probes for deep tissue fluorescence imaging. Efficient upconversion was achieved using a $NaYF_4$ host co-doped with Yb^{3+} and Tm^{3+} or Er^{3+} ions. In comparison to traditional fluorescent probes, UPNs were found to have the follow benefits: 1) they allow autofluorescence insensitive imaging through anti-Stokes shifted

emission. 2) they show no signs of photo-damage even at high intensities. 3) for deep tissue imaging, they provide higher resolution images. 4) they emit multiple line emissions with large Stoke shifts. To summarize, UPNs hold unique optical properties which make them attractive as fluorescent probes.

Populärvetenskaplig sammanfattning

Denna avhandling beskriver olika optiska metoder för att diagnostisera cancer. En sådan metod är optisk spektroskopi (att med hjälp av ljus bestämma fysiska och kemiska egenskaper hos ett prov) som har används för att undersöka cancer i ögat. Avhandlingen omfattar vidare studier av optiska kontrastmedel tillverkade av nanokristaller (nano = en miljarddels meter), vilkas innehåll av sällsynta jordartsmetaller ger unika optiska egenskaper. Dessa kontrastmedel är i huvudsak ämnade för forskningsmodeller.

Nästan alla olika ögoncancersjukdomar kan idag diagnostiseras med hjälp av standardiserade undersökningsmetoder som ögonspegling, ultraljud, kärlavbildning och magnetröntgen. Ögoncancer kan trots tillgång till dagens hjälpmedel ibland vara svår att diagnostisera. Som ett komplement till befintliga metoder har vi undersökt möjligheten att använda optisk spektroskopi för diagnos. Metoden är speciellt känslig för att kvantifiera innehållet av olika ämnen i mänsklig vävnad, som vatten och melanin och kan även tillämpas t.ex. för att mäta blodvärde och syremättnad. Synligt och nära-infrarött ljus kan belysa vävnad på flera centimeters djup, vilket kan användas för att söka ytligt liggande tumörer. I en serie experiment på grisögon har vi säkerställt att optisk spektroskopi kan med gott resultat kvantifiera mängden melanin och mängden blod i tumörliknande fantomer placerade i ögats åderhinnan. Vi har även kunnat visa att denna undersökning inte skadar ögat eller ger upphov till ökat ögontryck. Vidare har enuklerade ögon från människa med känd melanomdiagnos studerats. Optisk spektroskopi visade härvid relativt god träffsäkerhet i att mäta graden av pigmentering i melanomen. Sammanfattningsvis: optisk spektroskopi erbjuder ett gott komplement till nuvarande diagnosmetoder för ögoncancersjukdomar.

Optiska kontrastmedel inom forskning är ett starkt växande fält. En av anledningarna är att optiska markörer kan emitera upp till en miljard fotoner per sekund per markör. Detta är en mycket hög aktivitet jämfört med mer traditionella nukleära

markörer. Därutöver kan optiska markörer tillverkas av proteiner. Detta möjliggör fundamentala biologiska studier av genuttryck. På senare tid har nanomaterial med en storlek betydligt mindre än enstaka celler specialkonstruerats med unika optiska egenskaper. Vi har i en rad experiment studerat hur nanokristaller innehållande sällsynta jordartsmetaller kan utnyttjas som optiska markörer. Vi har funnit följande fördelar: 1) dess optiska signatur kan enkelt skiljas från den annars snarlika signaturen hos normal vävnad. Denna särskiljning är svår att uppnå med traditionella optiska markörer. 2) nanokristaller är stabila och faller inte sönder vid hög ljusintensitet. Detta är ett vanligt förekommande hos organiska markörer. 3) nanokristaller möjliggör avbildning med högre upplösning. 4) nanokristaller avger ljus med specifika färger. Sammanfattningsvis: nanokristaller innehållande sällsynta jordartmetaller uppvisar unika egenskaper vilket gör dem attraktiva som optiska markörer.

List of publications

This thesis is based on the following papers, which will be referred to by their roman numerals in the text.

I **A matrix-free algorithm for multiple wavelength fluorescence tomography**
A.D. Zacharopoulos, P. Svenmarker, J. Axelsson, M. Schweiger, S.R. Arridge and S. Andersson-Engels.
Optics Express **17**, 3025-3035 (2009).

II **Autofluorescence insensitive imaging using upconverting nanocrystals in scattering media**
C.T. Xu, N. Svensson, J. Axelsson, P. Svenmarker, G. Somesfalean, G. Chen, H. Liang, H. Liu, Z. Zhang and S. Andersson-Engels.
Applied Physics Letters **93**, 171103 (2008).

III **Use of nonlinear upconverting nanoparticles provides increased spatial resolution in fluorescence diffuse imaging**
P. Svenmarker, C.T. Xu and S. Andersson-Engels.
Optics Letters **35**, 2789-2791 (2010).

IV **High-Resolution Fluorescence Diffuse Optical Tomography Developed with Nonlinear Upconverting Nanoparticles**
C.T. Xu, P. Svenmarker, H. Liu, X. Wu, M.E. Messing L.R Wallenberg and S. Andersson-Engels.
Submitted for publication in ACS Nano.

V **Multispectral guided fluorescence diffuse optical tomography using upconverting nanoparticles**
P. Svenmarker, C.T. Xu, H. Liu, X. Wu and S. Andersson-Engels.
Manuscipt in preparation.

VI **Transscleral visible/near-infrared spectroscopy for quantitative assessment of melanin in a uveal melanoma phantom of ex vivo porcine eyes**
J. Krohn, C.T. Xu, P. Svenmarker, D. Khoptyar and S. Andersson-Engels.
Experimental Eye Research **90**, 330-336 (2010).

VII **Transscleral visible/near-infrared spectroscopy for quantitative assessment of haemoglobin in experimental choroidal tumours**
C.T. Xu, P. Svenmarker, S. Andersson-Engels and J. Krohn.
DOI: 10.1111/j.1755-3768.2010.02037.x (2010) *Acta Ophthalmologica.*

VIII **Effects of probe geometry on transscleral diffuse optical spectroscopy**
P. Svenmarker, C.T. Xu, S. Andersson-Engels and J. Krohn.
Biomedical Optics Express **2**, 3058-3071 (2011).

IX **Transscleral optical spectroscopy of uveal melanoma in enucleated human eyes**
J. Krohn, P. Svenmarker, C.T. Xu, S.J. Mörk and S. Andersson-Engels.
Submitted for publication in Investigative Ophthalmology & Visual Science.

X **Drug quantification in turbid media by fluorescence imaging combined with light-absorption correction using white Monte Carlo simulations**
H. Xie, H. Liu, P. Svenmarker, J. Axelsson, C.T. Xu, S. Gräfe, J.H. Lundeman, H.P.H. Cheng, S. Svanberg, Sune N. Bendsoe, P.E. Andersen, K. Svanberg, S. Andersson-Engels.
Journal of Biomedical Optics **16**, 066002 (2011).

Other related publications by the author:

Autofluorescence of pigmented skin lesions using a pulsed UV laser with synchronized detection: clinical results
H.P.H. Cheng, P. Svenmarker, H. Xie,
P. Tidemand-Lichtenberg, O.B. Jensen, N. Bendsoe,
K. Svanberg, P.M. Petersen, C. Pedersen,
S. Andersson-Engels and P.E. Andersen.
Proceedings of SPIE **7715**, 77151K (2010).

Transscleral optical spectroscopy in the diagnosis of choroidal tumours
J. Krohn, C.T. Xu, P. Svenmarker, D. Khoptyar and
Andersson-Engels, S..
Acta Ophthalmologica - meeting abstract **88**, p.41 (2010).

Abbreviations

CCD	charge-coupled device
CT	computed tomography
DLS	dynamic light scattering
EGF	epidermal growth factor
Er	erbium
ESA	excited state absorption
ETU	energy transfer upconversion
FDA	food and drug administration
FEM	finite element method
FP	fluorescent proteins
FRET	Förster (fluorescence) resonance energy transfer
FWHM	full width at half maximum
Gd	gadolinium
GFP	green fluorescent protein
GPU	graphics processing unit
Ho	holmium
ICG	indocyanine green
IR	infrared
Ln	lanthanide
LRET	luminescence resonant energy transfer
NADH	dehydrogenase
NIR	near-infrared
NIRS	near-infrared spectroscopy
NIRF	near-infrared fluorescence
MR	magnetic resonance

MRI	magnetic resonance imaging
QD	quantum dot
RPE	retinal pigment epithelium
RTE	radiative transport equation
SHG	second harmonic generation
TEM	transmission electron microscopy
Tm	thulium
TNM	tumor, node, metastasis
US	ultrasonography
UV	ultra-violet
WHO	world health organization
XCT	x-ray CT
Yb	ytterbium

Contents

Papers

Chapter 1

Introduction

The leading causes of death in the world are cardiovascular diseases, infectious and parasitic diseases, and cancer. In 2004, cancer accounted for 12% of the totals deaths world wide [1]. In 2008, the World Health Organization (WHO) reported 12.4 million new cancer cases and 7.6 million cancer deaths world wide, numbers that were estimated to grow to 26.4 million new cancer cases and 17 million deaths by year 2030 [2]. The most common cancers in the world in term of incidence were lung (1.52 million cases), breast (1.29 million cases) and colorectal (1.15 million cases). Lung cancer was also the most common cause of death (1.31 million), followed by stomach cancer (780 000 deaths) and liver cancer (699 000 deaths) [2].

Early cancer detection and diagnosis are key for survival. For most cancers, early detection (stage 1 on the TNM scale [3]) is associated with a >90% 5-year survival [4]. Today, clinical cancer diagnosis primarily relies on morphological observations. For detection, modern cancer management routinely employs anatomical imaging methods, *i.e.* x-ray computed tomography (CT), magnetic resonance imaging (MRI) and ultrasonography (US). All of these methods typically detect cancers when they are a centimeter or greater in diameter [5], and they do that by answering questions like, "is there a tumor?", "how large is it?" or "is it confined or has it spread through the lymph system?". For even earlier detection, new tools are in development, which seek to image the tumor physiology and the molecular signaling of tumors, rather than the tumor morphology [6, 7]. Two routes are explored for physiological and molecular imaging of cancer, either exploiting the natural contrast in the body, or, inducing the desired contrast by administrating specifically engineered contrast agents. The later have been popularized under the name *molecular imaging* [8, 9], and has been described by Ralph Weissleder as "In contradistinction to 'classical' diagnostic imaging, it sets forth to probe the molecu-

lar abnormalities that are the basis of disease rather than to image the end effects of these molecular alterations" [8]. Common to both approaches are that they seek answers to questions about the tumor function, like "what is the tumor metabolism?", "at which rate is angiogenesis occurring?" or "is apoptosis taking place?".

A rich flora of imaging technologies exist for visualizing tumor physiology and molecular signaling [7]. Positron emission tomography (PET) is typically applied in oncology for imaging glucose consumption as a measure of tumor metabolism [10]. MRI in conjunction with superparamagnetic nanoparticles has been applied to image lymph-node metastases in prostate cancer at increased contrast [11]. Optics have proved to be particularly suited for imaging cancer physiology, *e.g.* near-infrared (NIR) spectroscopy (NIRS) imaging of the physiological changes characteristic of tumors in breast, *i.e.* blood flow, oxygen consumption, and tissue structure [6, 12–16]. And fluorescence imaging (FI) have developed into being one of the cornerstone of molecular imaging [7, 17, 18], enabling *e.g.* to visualize tumor protease activity [19], angiogenesis [20] and apoptosis [21, 22]. A recent trend have been to combine imaging technologies to capitalize on their individual strengths [23]. Typically an anatomical and a functional imaging modality are paired together. Combinations include PET-CT [24], PET-MRI [25], FI-CT [26, 27] and FI-MRI [14, 28], which all improve the reconstruction and visualization of data.

This thesis makes contributions to physiological and molecular imaging of cancer using optics. Transscleral optical spectroscopy has been developed for diagnosing eye cancer. The technology exploits the natural contrast obtained from visible and NIR light to asses tumor physiology. Furthermore, upconverting nanoparticles have been investigated for the use as a fluorescent probe. With their unique optical properties, they hold the possibility to be an integral part of molecular probes shedding light onto tumor biomarkers.

1.1 Upconverting nanoparticles for use in fluorescence imaging

Fluorescence imaging in tissue can be performed at different length-scales, from nanometers to centimeters and every step in between, by employing different technologies, *i.e.* optical nanoscopy [29], optical projection tomography [30], two-photon fluorescence microscopy [31] and fluorescence diffuse optical tomography (fDOT) [32]. The fluorescent probe administrated to the tissue determines the image contrast. A wide diversity of contrast can be exploited, from gene expressions [33], to protein function [34], to Ca^{2+} concentration [35], to malignant glioma [36] can all be visualized through fluorescence.

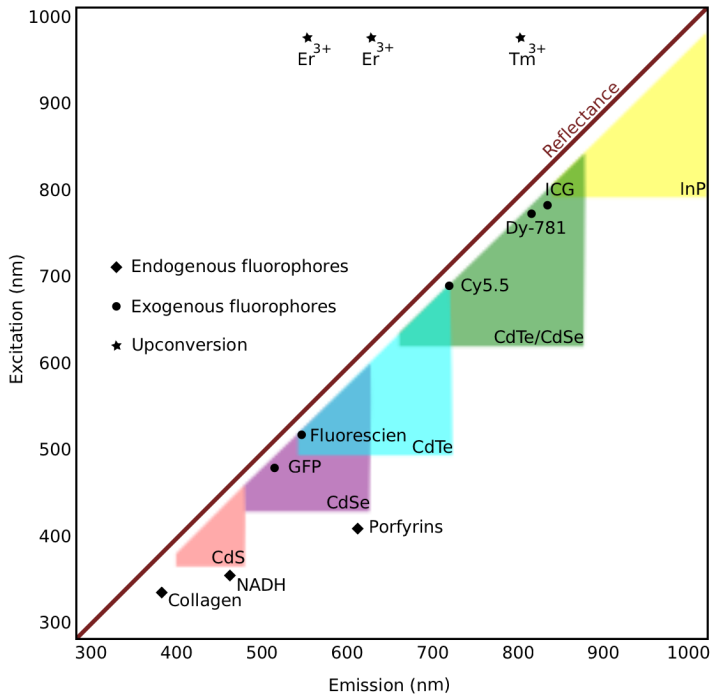

Figure 1.1. *Excitation-emission matrix for common endogenous [38] and exogenous fluorophores [34, 39, 40], quantum dots [41] and upconverting nanoparticles [42]. The quantum dots are indicated by the various types of semiconductor materials used. For each material, the emission peak can be tuned by the quantum dot diameter. Notice the unique positioning for the upconvering nanoparticles.*

Upconverting nanoparticles are crystals doped with rare earth ions [37], which can be used as fluorophores to give contrast in fluorescence imaging. In comparison to other common fluorophores (see Fig. 1.1), they have unique optical properties. For fluorescence imaging on the millimeter to centimeter length-scale using fDOT, upconverting nanoparticles have been found to have the follows benefits

(i) Autofluorescence insensitive. Due to its anti-Stokes shifted emission, the signal can be detected in a spectral region where no endogenous fluorophores emit. Paper **II**.

(ii) Non-bleachable. Even at intensities above $> \mathrm{kW/cm^2}$, upconverting nanoparticles have showed no sign of photodamage [43].

(iii) Increased resolution. Because of its quadratic power dependence, the particles will experience a more localized excitation field, which drives the resolution improvement. Papers **III** and **IV**.

(iv) Extreme anti-Stokes shifts. Multiple emission lines with shifts in excess of 8000 cm^{-1} are possible [42].

Paper **II** make use of the autofluorescence insensitive property of the upconverting nanoparticles. Papers **III** and **IV** describe how the resolution for fluorescence imaging and tomography can be increased using upconverting nanoparticles. And Paper **V** utilize the extreme anti-Stokes shifts available for precise depth localization.

1.2 Diagnosing eye cancer using transscleral optical spectroscopy

World wide statistics by the WHO are not specifically reported for eye cancer [2]. In the Nordic countries, however, for the time period 2005-2009, there were 310 new eye cancer cases and 56 eye cancer deaths annually, corresponding to 0.2% of all new cancer cases and 0.1% of all cancer deaths [44].

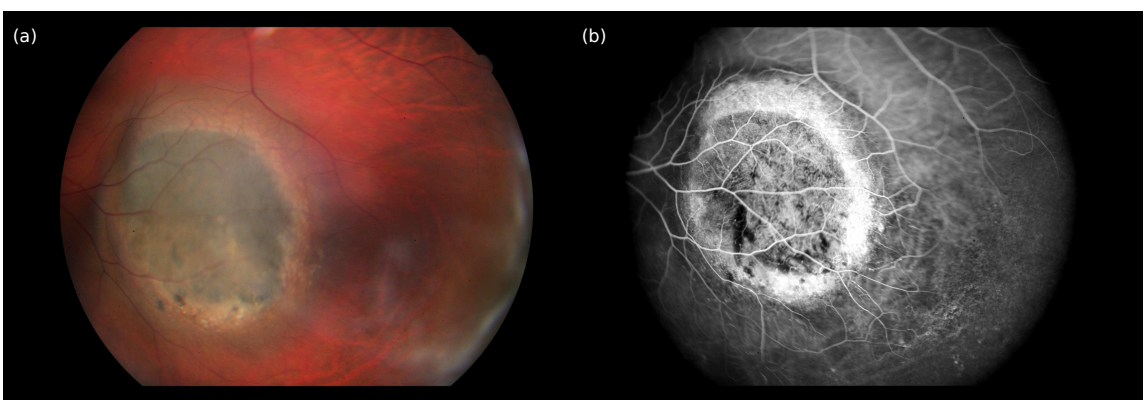

Figure 1.2. *(a) Fundus photograph and (b) fluorescein angiography of a choroidal melanoma in the left eye of a 22-year-old patient.*

Uveal melanoma is the leading primary intraocular malignancy in adults [45, 46]. Andrew Ferry could in 1964 show in a material of 539 enucleated eyes with clinically diagnosed melanoma, that 100 of the eyes contained a lesion different from that of melanoma [47]. Since then the diagnosis accuracy of melanoma has improved to be incorrect in less than 1% of the cases [48, 49]. The improved

diagnostic accuracy has been an effect of the combined contributions from an increased awareness of lesions that simulate malignant melanomas, improved diagnostic methods and the increased presence of units specializing on ocular tumors [46].

Common practice is to clinically diagnose an eye lesion using ophthalmoscopy (Fig. 1.2a). Supplementary techniques like ultrasonography (Fig. 1.3b) and fluorescein angiography (Fig. 1.2b) are also usually included in determining a diagnosis. In a few cases, a fine needle aspiration biopsy is needed to give a diagnose [45, 49]. Ultrasonography can determine the shape and size of intraocular tumors. It is also sensitive to melanoma, which typically presents a lower internal reflectivity [50]. Fluorescein angiography may visualize the blood flow into and within the tumors. By characteristic patterns, it helps differentiate the diagnosis. Fine needle aspiration biopsy is only employed when the diagnosis is not clearly established by noninvasive techniques. With a biopsy a histological diagnosis can be made [51].

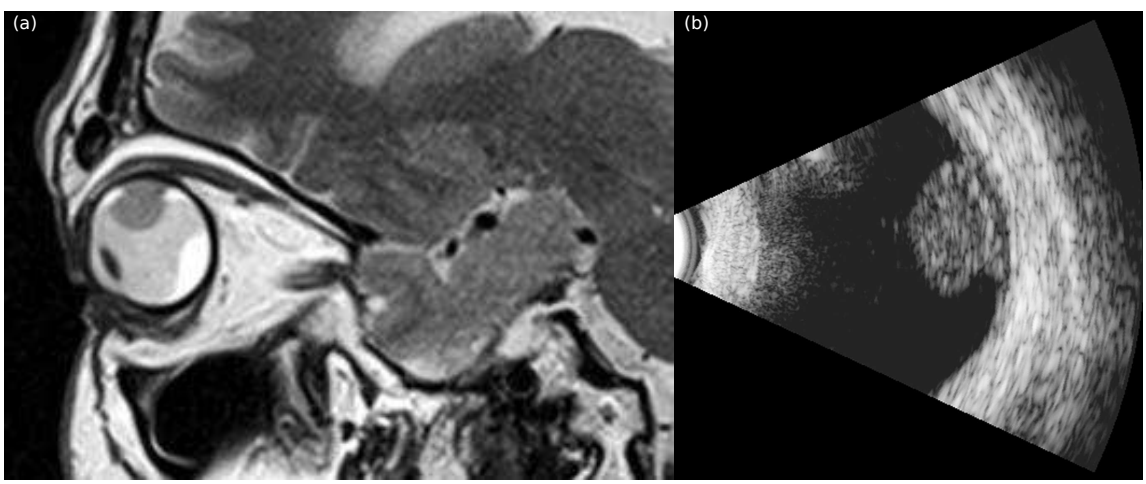

Figure 1.3. *(a) Sagittal T2-weighted MR image of a choroidal melanoma located superiorly in the right eye of a 52-year-old patient. (b) B-scan US image of the same uveal melanoma.*

As an alternative method, MRI (Fig. 1.3a) has been employed to study intraocular malignancies. T2-weighted images were sensitive, but did not significantly correlate to melanin content [52]. A significant differentiation of uveal melanomas to intraocular metastases could neither be found when investigated with magnetic resonance imaging [53]. Other alternative methods for diagnosing uveal melanomas include computed tomography [54, 55]. Size and shape could be retrieved from the images, but no distinct advantage over ultrasonography have been reported [51]. Even the combination of computed tomography and positron emission tomogra-

phy has been employed to diagnose uveal melanoma. In the that pilot study, only 60% of the cases could be correctly diagnosed [56].

We have studied the use of optical spectroscopy to diagnose intraocular tumors. Optical spectroscopy is a non-invasive or minimally invasive technique for measuring tissue chromophores, *e.g.* oxy- and deoxyhemoglobin, melanin, carotenes, lipids, and water [57]. A lesion can be characterized by quantifying the tissue chromophores and thereby a diagnosis can be made. Four Papers **VI**, **VII**, **VIII** and **IX** are presented within this thesis, investigating the possibilities of using optical spectroscopy for diagnosing intraocular tumors. Papers **VI** and **VII** report on melanin and hemoglobin spectroscopy in a uveal phantom of *ex vivo* porcine eyes. Paper **VIII** looks into the design of a probe suitable for *in vivo* measurements and Paper **IX** report the first clinical data from 9 enucleated eyes.

1.3 Aim and outline of the thesis

Three general aims can be stated:

(i) To improve and develop fluorescence imaging and tomography for the use of deeply seated fluorescent probes.

(ii) To investigate the benefits of upconverting nanoparticles to traditional dyes as fluorophores.

(iii) To develop transscleral optical spectroscopy for diagnosing intra-ocular tumors.

Detailed descriptions of the contribution towards these goals are given in the peer-reviewed scientific articles enclosed at the end of the thesis. The purpose of the thesis chapters are to give an introduction to the field and to put the scientific articles into a broader context. The chapters are organized as follows:

Chapter 2 outlines the physical models of light-tissue interactions. Scattering is given a central role since it governs all the work presented within this thesis. Absorption and fluorescence are introduced from a quantum mechanics view-point and examples of tissue absorption and fluorescence are given.

Chapter 3 describes how to model photon migration in tissue. The radiative transport equation is introduced and different approaches for solving it are presented. Special focus is given to the diffusion approximation to the radiative transport equation. Fluorescence photon migration is introduced, which highlights the use of the reciprocity theorem of the radiative transport equation.

Chapter 4 presents fluorescence imaging and tomography in scattering media. The different ways used for measuring the fluorescencent signal are presented, together with the different measuring geometries used. Fluorescence tomography is introduced as a model-based optimization problem. Different ways of regularization the optimization problem is discussed together with different approaches of solving the optimization problem.

Chapter 5 is devoted to upconverting nanoparticles. A small review and the basic concepts are presented. The efficiency of upconverting nanoparticles are discussed in some detail and characterization of the particles used are given.

Chapter 6 covers transscleral optical spectroscopy. A brief overview of the anatomy of the eye is given. The tumor model developed is presented. Improvements to the spectroscopy equipment used are outlined. Different approaches to evaluate the data are discussed and future directions are given.

Chapter 2

Light-tissue interactions

This chapter outlines the different light-tissue interactions commonly encountered. It begins by introducing scattering, which is a center-piece of this thesis. Thereafter, absorption and fluorescence in tissue are presented.

2.1 Scattering

Scattering is the process where a propagating wave is interrupted by an object, whereby this object makes the wave change its path. The object can be anything from an atom to a water droplet or something more complex like a cell. The wave considered here is an electromagnetic wave with a wavelength corresponding to visible and NIR light. Only elastic scattering is considered, *i.e.* when the energy of the wave, and thus its frequency is conserved.

2.1.1 Scattering from a single object

To begin the discussion about scattering, a single particle or object is considered with a plane wave incident onto the particle. If the particle is much smaller than the wavelength of the wave, *e.g.* an atom, the scattering process can be described according to Lord Rayleigh's writing from 1871 [58, 59]. The wave will drive the electron cloud surrounding the nucleus in an oscillatory motion. Accelerating charges, *i.e.* electrons in the presence of a wave, emit radiation perpendicular to the oscillatory motion. The willingness of the electron cloud to move in a certain direction is described by its polarization. Similarly, the wave has a polarization, describing in which direction it is oscillating. Depending on if the polarization of the wave overlaps with the polarization of *e.g.* an atom, the wave will change its path or pass undisturbed. The strength of the scattering depends on how close the frequency of the wave is to the resonant frequency of the electron cloud.

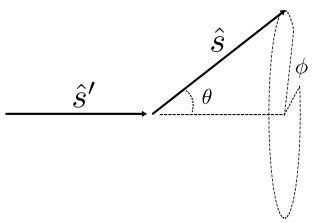

Figure 2.1. *Scattering from direction $\hat{\boldsymbol{s}}'$ into direction $\hat{\boldsymbol{s}}$. The in-plane angle θ and aximuthal angle ϕ are indicated.*

In the other limit, when the object is much larger than the wavelength of the wave, *i.e.* a mirror or a piece of glass, the process is not longer named scattering, but referred to as refraction or reflection. In this regime, scattering can be seen as a distortion to the wavefront, forcing the wave to propagate in a new direction. The law governing refractions, Snell's law, is named after Willebrord Snellius, a Dutch astronomer and mathematician, who was born in 1580.

In-between, when the approximation of a point or an infinite scatterer cannot be made, no simple solutions are available. The exception is for the case of perfectly spherical particles, where Gustav Mie presented a solution in his paper from year 1908 [60].

Irregardless in which regime the scattering takes place, it may be characterized by the *differential scattering cross section* $\partial\sigma_s$, which describes the angular distribution of the power of the wave after interacting with a scatterer. Integrating over all solid angles, yields the *scattering cross section* σ_s.

$$\sigma_s = \int_{4\pi} \partial\sigma_s d\omega' \tag{2.1}$$

The scattering cross section thus describes the strength of the interaction, *i.e.* how much of the power of the wave that will be scattered. Even though not explicitly noted in Eq. (2.1), the differential scattering cross section and thus also the scattering cross section will dependent on the wavelength of the incident wave. Normalizing the differential scattering coefficient with the scattering cross section, yields the *scattering phase function*.

$$p(\hat{\boldsymbol{s}}', \hat{\boldsymbol{s}}) = \frac{\partial\sigma_s}{\sigma_s} \tag{2.2}$$

It describes the power of a wave propagating in the direction $\hat{\boldsymbol{s}}$ after interacting with the scatterer from the direction $\hat{\boldsymbol{s}}'$. Usually, the phase function is assumed to depend only on the deflection angle θ and not on the azimuthal angle ϕ; see Fig. 2.1.

$$p(\hat{\boldsymbol{s}}', \hat{\boldsymbol{s}}) \approx p(\hat{\boldsymbol{s}}' \cdot \hat{\boldsymbol{s}}) = p(\cos\theta) \tag{2.3}$$

For macroscopic objects, *i.e.* a mirror, the phase function can be calculated geometrically. In the case of Rayleigh scatters, the phase function is isotropic. For Mie scatters, the phase function depends on the size and refractive index of the spherical particles, and is dominantly forward scattering, with side-lobes caused by interference effects, see Fig. 2.2.

2.1.2 Ensemble of scatterers

For an ensemble of scatterers, the contribution of each scatterer needs to be considered. If the number of scatterers are few, the

first Born approximation may be applied. It assumes that the individual scatterers do not affect each other, *i.e.* the wave reaching every scatterer will be a plane wave undisturbed by any previous scattering events. For more densely located scatterers, the interactions between all scatterers needs to be considered, which leads to an immense problem to solve. To treat every scatterer individually for a large ensemble is therefore not feasible.

At this point, the deterministic view on scattering is abandoned in favor of a statistical approach. Instead of describing scattering properties of a medium by a collection of scattering centers, where the position and shape of each scatterer is known, a density of scatterers ρ_s is introduced. In this way, the *scattering coefficient* μ_s can be written as

$$\mu_\mathrm{s} = \sigma_s \rho_s \tag{2.4}$$

It describes the probability of interacting with scatterers per unit path length. By looking at scattering as a statistical collection of scatterers, calculations are made easy, but the description of light is compromised. No longer can interference of waves be expressed, since only the intensity is considered.

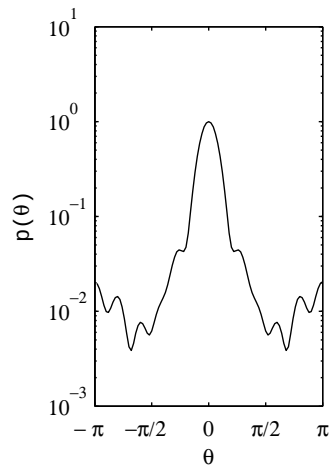

Figure 2.2. *Mie phase function plot for 1 μm in diameter spheres with refractive index 1.5 and at a wavelength of 632.8 nm. Data generated with the Mie Scattering Calculator [61].*

2.1.3 Scattering in tissue

Scattering in tissue is complex. Tissue consist of structures on many different length scales, from surfaces between tissue types, over cell with a typical size of several micrometers, through organelles, such as mitochondria and nuclei with a size of micrometers, to, proteins on the nanometer length scale. All of these structures carry different refractive indices and are not located in any regular patterns. Thereby a statistical approach to describe scattering is motivated.

The spectral variation of the scattering coefficient in tissue is usually approximated with a simple power law [62, 63]. It hold similarities with both Mie and Rayleigh theory of scattering, which both have a wavelength power dependence of the scattering cross section, $\sigma_s \sim \lambda^{-2}$ and $\sigma_s \sim \lambda^{-4}$, respectively.

$$\mu_\mathrm{s} = a\lambda^{-b} \tag{2.5}$$

The coefficients a and b are linked with the structure of the tissue. In Mie theory, the coefficient b is related to the particle size and coefficient a to the scatter density. Attempts have been made to describe the particle size through Mie theory [64] of breast tissue by measuring the scattering spectrum. Alternatively, the scattering coefficient can be written as a sum of the Mie and Rayleigh contributions [65],

$$\mu_\mathrm{s} = A\mu_\mathrm{s}(\mathrm{Mie}) + B\mu_\mathrm{s}(\mathrm{Rayleigh}) \tag{2.6}$$

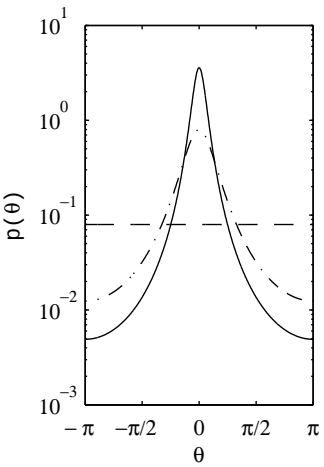

Figure 2.3. *Henyey-Greenstein phase function plots with anisotropy values g=0, g=0.6 and g=0.8, represented by dashed, dashed-solid and solid lines, respectively.*

A scattering phase function commonly adopted to describe tissue is the *Henyey-Greenstein* [66] function. It can be seen as an approximation to a Mie scattering phase function.

$$p(\cos\theta) = \frac{1}{4\pi}\frac{1-g^2}{(1+g^2-2g\cos\theta)^{3/2}} \tag{2.7}$$

Here g is the anisotropy factor equal to the average of the cosine for the scattering angle $g = \langle\cos(\theta)\rangle$. See Fig. 2.3 for a visualization of the scattering pattern for different anisotropy factors.

2.2 Absorption

Absorption of electromagnetic waves is best described from a semi-classical and semi-quantum mechanical view point. The absorbing object, *e.g.* an atom or a molecule, is understood from a quantum mechanical perspective, whereas the electromagnetic wave is treated classically. In this way, the energy of *e.g.* a molecule, may be quantized into discrete energy states described by *e.g.* its electronic, vibrational and rotational configuration. The energy carried by the electromagnetic wave is described by its frequency. Absorption occurs if the energy of the electromagnetic wave exactly matches the energy difference between two different states in *e.g.* a molecule.

In environments were atoms or molecules may move freely, *i.e.* gases, the energy states are well defined and precise. This is what makes gases transparent, since most frequencies of the electromagnetic spectra will not be resonant with any of the individual molecular energy states. Measuring the energy states of a freely moving atom or molecule may with ease be done with six digits precision. In tissue, neither atoms nor molecules may move freely. They will constantly be interfered by the surrounding environment, transforming the otherwise narrow energy states to broad-band features. Typical absorption features in tissue are several nanometers wide and a measurement precision of four digits is sufficient to capture the relevant information.

Once the energy of the electromagnetic wave is absorbed, or from *e.g.* an atoms point of view, once it is excited, several events may follow. A common outcome is that the energy is transformed into heat. Another that the absorbed energy is re-emitted as an electromagnetic wave, so called fluorescence. Fluorescence is discussed in more detail in Section 2.3. A third possibility is that the absorbed energy is transferred non-radiatively to an nearby atom or molecule. This phenomena is exploited for the upconverting process, which is the topic of Chapter 5.

To describe absorption in tissue, an *absorption coefficient* μ_a is introduced. It represents the probability of photon absorption per unit path length and is defined as

$$\mu_{\mathrm{a}} = \sigma_a \rho_{abs} \tag{2.8}$$

where σ_a is the absorption cross-section and ρ_{abs} is the density of absorbers. A statistical representation of the absorbers in terms of a density is sufficient, since the energy absorbed is considered lost. The relation between absorption and the intensity, I_0, of a light source is given by the famous Beer-Lambert law, which forms the basis for optical absorption spectroscopy.

$$I = I_0 \exp(-\mu_{\mathrm{a}} L) \tag{2.9}$$

Here I is the intensity after a propagation length L. As discussed previously, the absorption coefficient will take on different values depending on the frequency of the probing electromagnetic wave. This may also be expressed as a wavelength dependent absorption coefficient, $\mu_{\mathrm{a}}(\lambda)$. Every molecule will have its own absorption spectrum, *i.e.* the variation of the absorption coefficient with wavelength, giving rise to a signature that can be used to identify it. In tissue, the molecules of interest are so large that only part of it will be involved in giving its absorption properties. The subset of molecules involved is called a chromophore. Typically, more than one chromophore is present, then the total absorption coefficient is the sum of the contribution form each chromophore. At this point it is convenient to express the absorption coefficient in terms of the chromophore absorption, rather than an absorption density, which yields

$$\mu_{\mathrm{a}}(\lambda) = \sum_i \epsilon_i(\lambda) C_i \tag{2.10}$$

where ϵ_i is the extinction coefficient and C_i the chromophore concentration. Knowing the extinction coefficient and measuring the absorption coefficient, the chromophore concentration can be computed.

2.2.1 Absorption in tissue

A range of chromophores have been identified in tissue, of which some are presented in Fig. 2.4. In the ultraviolet and visible spectral range, tissue is highly scattering and absorbing. In the spectral range beyond 1300nm, the water absorption is very strong. Both effects yield a limited penetration depth of electromagnetic radiation. In the middle part of the spectra, bounded by hemoglobin absorption at the blue side and water absorption at the red side of the spectra, the so called tissue-optical-window lays. In this region electromagnetic radiation may propagate millimeters to centimeters in tissue. The main absorbing chromophores are presented below.

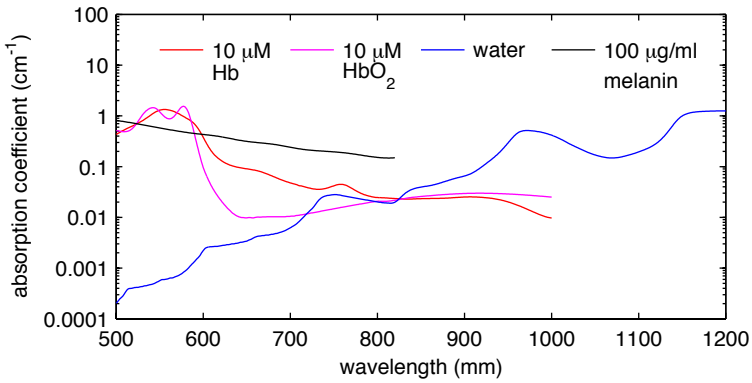

Figure 2.4. *Absorption spectra of a few common tissue chromophores: Oxygenated and deoxygenated hemoglobin [67], water [68] and melanin [69].*

Hemoglobin is an iron-containing and oxygen-carrying protein, which makes up about 35% of the human blood cell's mass. Both oxyhemoglobin and deoxyhemoglobin have distinct absorption spectra. Hemoglobin is an easily accessible chromophore to measure, and is especially important since the oxygen saturation can be deduced. For an extensive introduction to hemoglobin spectroscopy, the reader is referred to book by Zijlstra *et al.*[67]. Near-infrared spectroscopy of hemoglobin is further discussed in Section 6.5.2.

Water makes up approxemtly 2/3 of the human body weight. As such, it is a chromophore that will have a strong influence of the overall absorption in tissue. Liquid water is most transparent in the same spectral region where the human eyes are most sensitive, namely in the green region. Both at longer and shorter wavelengths, water absorb strongly. Within the tissue-optical-window water has a characteristic absorption features at 980 nm.

Melanin is dark brown or black pigments. It is present in many parts of the human body, with the skin [70] being the most common organ. It can also be found in other organs, *i.e.* the eyes [71] or the brain [72]. Melanin is known to protect the skin from photo damage induced by the sun [71]. Since natural shape of melanin is as a particle, its absorption properties are difficult to distinguish from its scattering properties, and as a result, any precise measurement of the absorption coefficient by traditional means does not exist.

Lipids is a collective name for fat, phospholipids, fat-soluble vitamins and others. Phospholipids are the building blocks of the

cell membrane and fat is used as energy storage. The absorption of lipids is similar but weaker than that of water.

2.3 Fluorescence

Fluorescence or more generally, luminescence, is the emission of light from a molecule upon decaying from an electronically excited state [73]. Two different decaying pathways are distinguished and named fluorescence or phosphorescence. The difference arise from which state the excited electron decays from - either a singlet or a triplet state. A singlet or a triplet state denotes the degeneracy of the excited energy level and depends on the orientation of the spin of two paired electrons. If the spins are anti-parallel, a singlet is formed, and consequently, if the spins are parallel, a triplet is formed. The ground state of most molecules is as a singlet (molecular oxygen is a famous exception). Thus, an excited singlet state electron returns rapidly to the the ground state by emission of a photon, since the transition preserves the total spin. In contrast, phosphorescence emission violates the quantum mechanics selection rules by changing the total spin, and therefore, the decay time is slow.

A Jablonski diagram is a common way of illustrating the processes involved between absorption and emission of light. A typical Jablonski diagram is shown in Fig. 2.5. It depicts the electronic potentials S_0, S_1 and S_2, corresponding to the ground and excited electronic potentials. Every electronic potential have a number of vibrational energy levels, depicted as $v = \{1, 2, 3 \dots\}$. The absorption transition occurs on the femtosecond timescale and usually lifts one of the electrons to a higher vibrational state in either S_1 or S_2. Following absorption, the molecule may undergo internal conversion, a processes on the picosecond timescale, where the electron falls down the ladder structure of vibrational levels, until the population between the vibrational levels are in thermal equilibrium. The energy lost is dissipated as heat. Most electrons will have sufficient time to reach all the way to the bottom of the electronic potential, since the fluorescence lifetime is on the nanosecond timescale, three orders of magnitude slower than the internal conversion process. Once at the bottom, the molecule may return to the ground electronic potential via the emission of a fluorescent photon. Upon returning, the molecule typically relaxes to a higher vibrational state in S_0, and then internal conversion occurs until thermal equilibrium is reached. Molecules in the excited state S_1 may also convert its spin and cross over to the first excited triplet state T_1. Emission from T_1 yields phosphorescence and have an characteristic timescale of milliseconds to seconds.

An alternative way to a Jablonski diagrams of illustrating fluorescence, is by its absorption and emission spectra. Typcial spectra

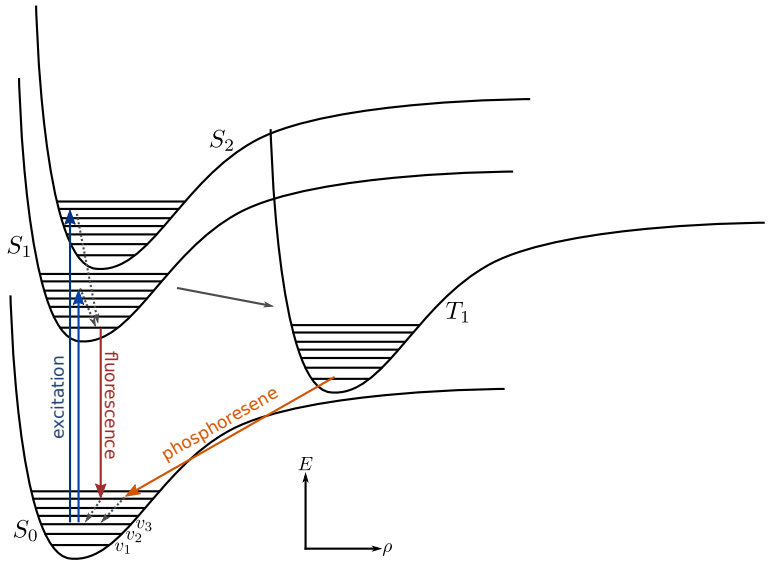

Figure 2.5. *Jablonski diagram displaying the ground electronic potential S_0, and the first and second excited state potentials S_1 and S_2, all with vibrational levels $v = \{1, 2, 3 \dots\}$. The triplet state potential T_1 is also indicated. Solid colored arrows indicate photon excitation/emission. Black dotted arrows show internal conversion and the solid black arrow transfer between a singlet and triplet state.*

are presented in Fig. 2.6. Notice how the absorption spectrum is close to a mirror image of the emission spectrum. This can be understood by that the vibrational levels in the ground state has not been greatly altered between excitation and emission. As such, the absorption and emission spectra both reflect the vibrational energy levels in the ground state. Also, following the cycle in the Jablonski diagram, it is apparent that the fluorescent photon is of lower energy compared to the excitation photon. The spectral shift corresponding to the energy difference is called a Stokes shift. Another property of fluorescence is that the emission spectrum is usually independent of excitation energy. This is due to the fast internal conversion occurring from higher excited states to the first electronic state and its lowest vibration energy level.

A useful quantity for the continued discussion about the fluorescence is the *quantum yield*. It is defined as the number of photons emitted divided by the number of photons absorbed.

$$\gamma = \frac{\#\text{ photons emitted}}{\#\text{ photons absorbed}} \tag{2.11}$$

A related quantity is the *fluorescence yield*, which can be written

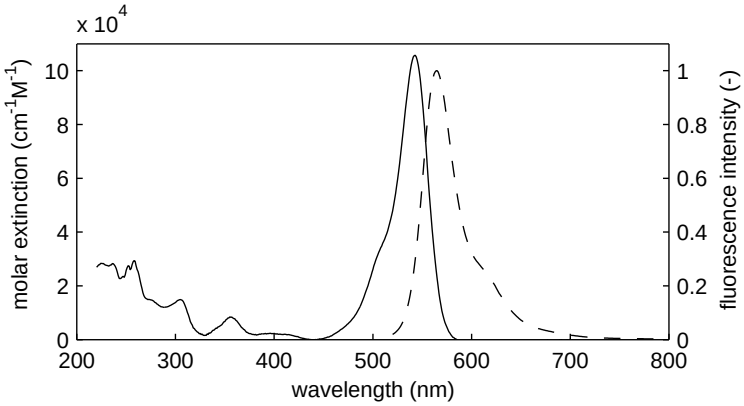

Figure 2.6. *Extinction and emission spectrum for rhodamine B. Data from ref [74].*

as

$$\eta = \mu_{\text{af}}\gamma \tag{2.12}$$

and is the product of the absorption coefficient of a fluorophore μ_{af} and the quantum yield. It can thus be used to describe the fluorescence intensity, I_f, irradiated upon excitation with an intensity I_x.

$$I_f = \eta I_x \tag{2.13}$$

2.3.1 Endogenous fluorophores

Endogenous fluorophores is the name given to natural tissue constituents which emit *autofluorescence*. A range of biological structures, including mitochondria to connective tissue, emit autofluorescence upon ultra-violet (UV) excitation. The need of UV excitation to induce fluorescence limits the penetration depth, since tissue is highly scattering and absorping in this wavelength region. All the different autofluorescent biological structures have overlapping absorption and emission spectra, making it a challenge to separate the individual responses. Still, considerable efforts are being made to develop autofluorescence spectroscopy [38, 75, 76] and imaging [77]. More recently, the use of multiphoton techniques have extended the penetration depth of autofluorescent imaging considerable, and have been applied for *in vivo* skin diagnostics [78]. Typical autofluorescent biological structures include:

Collagen and **elastin** are the building blocks for connective tissue. By assessing the autofluorescence from collagen and elastin in the extracellular matrix, the skin age can be estimated [79].

NADH is involved in the cell metabolism. Indications obtained from autofluorescence images suggest that an increased amount of NADH would be present in the cell mitrocondia [80]. NADH content have also been hypothesized to increase in dysplastic cervix tissue [81].

2.3.2 Exogenous fluorophores

Exogenous fluorophores are fluorescent agents that have been administered externally to the the tissue. Currently there are only three fluorophores approved for clinical use by the food and drug administration (FDA) in the United States of America: indocyanine green (ICG) , fluorescein and methylene blue. For preclinical use, a range of different fluorophores are available for *in vivo* imaging [82]. Here follows some common exogenous fluorophores.

Non-targeting probes include among others ICG and fluorescein. ICG is used for hepatic function diagnostics [83] and ophthalmic angiography [84]. It has also been investigated for use in breast cancer imaging [14, 15] and lymphatic imaging [85]. Fluorescein is used in many application, *e.g.* as laser gain medium or for dye tracing. In medicine, it is mainly used for ophthalmic angiography [86].

Active targeting probes consist of a fluorophore conjugated to a ligand that binds to a specific molecular target [87, 88]. The use of targeting probes leads to an increased accumulation of the contrast agent at the target site, since non-bounded probes are cleared by the body. Ligands can be small molecules, peptides, proteins and antibodies. Fluorophores can be cyanine dyes, fluorescein, ICG and others. Targeting was first demonstrated with monoclonal antibodies conjugated to cyanine dyes in nude mice [89, 90] and later also clinically for colon carcinomas [91]. Small peptides ligands have been used for imaging epidermal growth factor (EGF) receptors in breast cancer xenografts [92]. In a further example, Gao *et al.*[93] used quantum dots as fluorophore together with antibodies for *in vivo* tumor imaging.

Fluorescent proteins (FPs) brings a new type of contrast to fluorescence imaging, since they can be used as reporter genes. Simply put, gene expression can be visualized by fluorescence emission [33]. Green FP was first discovered in jellyfish *Aequorea victoria* [94] and have since been modified through genetic engineering to give FPs with red-shifted excitation/emission wavelengths [95, 96]. An overview of the present available FPs are given by

Shaner *et al.*[97]. In cancer research, FPs have been used for visualizing tumor cell mobility, invasion, metastasis and angiogenesis [20].

Nanoparticles is a new class of emerging fluorophores. Quantum dots (QDs) are semiconductor structures with typical sizes of 2-8 nm in diameter emitting fluorescence [41, 98]. Compared to organic dyes and fluorescent proteins, QDs offer several advantages, *i.e.* size- and composition-tunable emission from visible to infrared wavelengths, large extinction coefficients, narrow band fluorescence with large Stokes shifts and resistance to photobleaching. They are suitable for multiplexing, since multiple emission bands can be excited simultaneously. Biocompatable QDs are readily available, and their size with a large surface to volume, give them interesting properties for bioconjucation [99]. Toxicity of QDs is a concern and have recently been reviewed [100]. Upconverting nanoparticles is a different class of nanocrystal fluorophores and are presented in Chapter 5.

Chapter 3

Photon migration in turbid media

This chapter describes how to model photon migration in tissue. The radiative transport equation is introduced and different approaches for solving it are presented. Special focus is given to the diffusion approximation to the radiative transport equation. Fluorescence photon migration is introduced, which highlights the use of the reciprocity theorem of the radiative transport equation.

3.1 Radiative transport theory

3.1.1 Radiometric quantities

This section introduces the radiometric quantities used to describe photon migration in tissues with radiative transport theory. They are based on the concept of a *photon distribution function*, which describes the number of photons per unit volume at position $\bar{\boldsymbol{r}}$ traveling in the direction $\hat{\boldsymbol{s}}$ at a given time t, and is defined as follows.

$$N(\bar{\boldsymbol{r}}, \hat{\boldsymbol{s}}, t) \equiv \text{number of photons per unit volume at position } \bar{\boldsymbol{r}}\text{, propagating in the direction } \hat{\boldsymbol{s}} \text{ at time } t. \ [1/\mathrm{m}^3\mathrm{sr}]$$

Disregarding the propagation direction of the photons, the concept of *photon density* can be introduced. It states the number of photons per unit volume at a given position $\bar{\boldsymbol{r}}$ and time t and is found by integrating the photon distribution function over all solid angles.

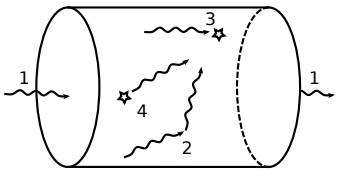

Figure 3.1. *Events involed in the radiative transport equation:*

1: Flux across boundary
2: Scattering
3: Absorption
4: An internal source

$$\rho(\bar{\boldsymbol{r}},t) \equiv \int_{4\pi} N(\bar{\boldsymbol{r}},\hat{\boldsymbol{s}},t)\; d\hat{\boldsymbol{s}} \quad [1/\mathrm{m}^3] \tag{3.1}$$

Another useful quantity is the *radiance*. It describes the power propagating in direction $\hat{\boldsymbol{s}}$ at positions $\bar{\boldsymbol{r}}$ and time t per unit area, and is defined as the photon distribution function times the photon energy and speed.

$$L(\bar{\boldsymbol{r}},\hat{\boldsymbol{s}},t) \equiv h\nu \cdot c \cdot N(\bar{\boldsymbol{r}},\hat{\boldsymbol{s}},t) \quad [\mathrm{W/m^2sr}] \tag{3.2}$$

Here h is Plank's constant, ν the frequency of the photons and c the speed of light in the medium. Similarly to the photon density, the *fluence* or *fluence rate* is defined by the integral of the radiance over all solid angles.

$$\Phi(\bar{\boldsymbol{r}},t) \equiv \int_{4\pi} L(\bar{\boldsymbol{r}},\hat{\boldsymbol{s}},t)\; d\hat{\boldsymbol{s}} \quad [\mathrm{W/m^2}] \tag{3.3}$$

The fluence rate may be interpreted as the power incident onto a sphere divided by its cross-section area. It is the intensity of the radiation. This is a very useful quantity since it easily can be measured. Note also that the fluence rate can be expressed with the help of the photon density as

$$\Phi(\bar{\boldsymbol{r}},t) = c \cdot h\nu \cdot \int_{4\pi} N(\bar{\boldsymbol{r}},\hat{\boldsymbol{s}},t) d\hat{\boldsymbol{s}} = c\, h\nu \cdot \rho(\bar{\boldsymbol{r}},t) \tag{3.4}$$

Talking about the fluence rate or the photon density is very similar, the only difference is if the power of the photons are accounted for. Also of interest is the photon flux, which can be seen as a photon current

$$\boldsymbol{F}(\bar{\boldsymbol{r}},t) \equiv \int_{4\pi} L(\bar{\boldsymbol{r}},\hat{\boldsymbol{s}},t)\hat{\boldsymbol{s}}\; d\hat{\boldsymbol{s}} \quad [\mathrm{W/m^2}] \tag{3.5}$$

3.1.2 Radiative transport equation

Radiative transport is the foundation for photon migration theory. It describes photon propagation as a transport problem, first developed to study neutron beams in nuclear reactors, it is nowadays extensively applied to bring understanding of light propagation i tissue. The radiative transport equation is derived from the principle of energy conservation and by considering the photon interactions in a small volume. Thus it neglects the wave properties of light and cannot *e.g.* model interference effects. It takes the form

$$\frac{1}{c}\frac{\partial L(\bar{\boldsymbol{r}},\hat{\boldsymbol{s}},t)}{\partial t} = -\hat{\boldsymbol{s}}\cdot\nabla L(\bar{\boldsymbol{r}},\hat{\boldsymbol{s}},t) - (\mu_{\mathrm{a}}+\mu_{\mathrm{s}})L(\bar{\boldsymbol{r}},\hat{\boldsymbol{s}},t) + \mu_{\mathrm{s}}\int_{4\pi} p(\hat{\boldsymbol{s}}',\hat{\boldsymbol{s}})L(\bar{\boldsymbol{r}},\hat{\boldsymbol{s}}',t)d\hat{\boldsymbol{s}}' + q(\bar{\boldsymbol{r}},\hat{\boldsymbol{s}},t) \tag{3.6}$$

Here all of the notation have been introduced earlier in Sections 3.1.1 and Chapter 2, except for $q(\bar{\boldsymbol{r}},\hat{\boldsymbol{s}},t)$ $[1/sm^3sr]$, which describes a source emitting photons per unit volume, steradian and time. The lefthand side of Eq. (3.6) is the change in radiance over time, which may be caused by four different events.

(i) $\hat{\boldsymbol{s}}\cdot\nabla L(\bar{\boldsymbol{r}},\hat{\boldsymbol{s}},t)$ Photon loss due to crossing the boundary.

(ii) $(\mu_{\mathrm{a}}+\mu_{\mathrm{s}})L(\bar{\boldsymbol{r}},\hat{\boldsymbol{s}},t)$ Absorption or scattering losses.

(iii) $\mu_{\mathrm{s}}\int_{4\pi} p(\hat{\boldsymbol{s}}',\hat{\boldsymbol{s}})L(\bar{\boldsymbol{r}},\hat{\boldsymbol{s}}',t)d\hat{\boldsymbol{s}}'$ Photons scattered into the direction $\hat{\boldsymbol{s}}$ from all other directions.

(iv) $q(\bar{\boldsymbol{r}},\hat{\boldsymbol{s}},t)$ Photons created.

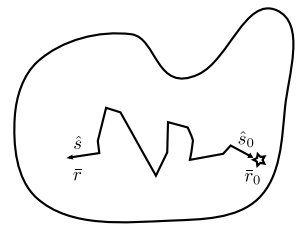

Figure 3.2. *An illustration of the reciprocity theorem for volume Ω with boundary $d\Omega$. A photon at $\bar{\boldsymbol{r}}$ traveling in the direction $\hat{\boldsymbol{s}}$ originating for from a soruce at $\bar{\boldsymbol{r}}_0$ launched in the direction $\hat{\boldsymbol{s}}_0$ may be reversed.*

3.1.3 Reciprocity theorem

A useful relation for the radiative transport equation is the reciprocity theorem, as illustated in Fig. 3.2. It states that the radiance rate at $\bar{\boldsymbol{r}}$ in the direction $\hat{\boldsymbol{s}}$ from a source at $\bar{\boldsymbol{r}}_0$ in the direction $\hat{\boldsymbol{s}}_0$ is the same as the radiance at $\bar{\boldsymbol{r}}_0$ in the direction $-\hat{\boldsymbol{s}}_0$ from a source at $\bar{\boldsymbol{r}}$ in the direction $-\hat{\boldsymbol{s}}$ [101].

$$L(\bar{\boldsymbol{r}},\hat{\boldsymbol{s}};\bar{\boldsymbol{r}}_0,\hat{\boldsymbol{s}}_0) = L(\bar{\boldsymbol{r}}_0,-\hat{\boldsymbol{s}}_0;\bar{\boldsymbol{r}},-\hat{\boldsymbol{s}}) \tag{3.7}$$

By integrating Eq. (3.7) over all solid angels for the source, the reciprocity for a point source can be written as

$$L(\bar{\boldsymbol{r}},\hat{\boldsymbol{s}};q_0(\bar{\boldsymbol{r}}_0)) = \Phi(\bar{\boldsymbol{r}}_0;\bar{\boldsymbol{r}},-\hat{\boldsymbol{s}}) \tag{3.8}$$

where q_0 is the point source. In this way, the radiance at $\bar{\boldsymbol{r}}$ in the direction $\hat{\boldsymbol{s}}$ due to an isotropic source at $q_0(\bar{\boldsymbol{r}}_0)$ is equal to the fluence at $\bar{\boldsymbol{r}}_0$ from a source at $\bar{\boldsymbol{r}}$ in the direction $\hat{\boldsymbol{s}}$. This forms the basis for the adjoint formulation used for simplifying computations. It will be applied to fluorescence migration, which is introduced in Section 3.3.

3.1.4 Solving the radiative transport equation

Solving the radiative transport equation is not straight-forward. A range of methods can be used, of which some are presented here.

Monte Carlo

A preferred method of solving the radiative transport equation is by Monte Carlo simulations. It is widely considered the gold standard. Finding a solution to the equation is done by a statistical approach, where numerous of fictional particles are launched and tracked in a geometry in which they have to obey the laws governed by the radiative transport equation. In the limit of simulating infinite many particles, the Monte Carlo simulation will be an exact solution.

The use of Monte Carlso simulations to model photon migration in tissue was first introduced by Wilson and Adam in 1983 [102]. Since then several implementations of the Monte Carlo method have been presented by various research groups. The MCML code by Wang *et al.*[103] is probably the best known and have become a standard tool for solving the RTE in layered structures. This implementation was used in Paper **VI**. Another example is the tMCimg code by Boas *et al.*[104], capable of calculating the time response for an arbitrary 3D media.

To speed up the otherwise slow performance of Monte Carlo simulations, white Monte Carlo simulations can be made for simple geometries, *i.e.* infinite and semi-infinite geometries. The color white refers to the implementation strategy of making a single zero absorption simulation. The real absorption can be added afterwards using the Beer-Lambert law. The scattering coefficient may be rescaled with the spatial and temporal coordinates [105–107].

More recently, a major step in speed up was achieved by using parallel computing on graphics processing units (GPU). Monte Carlo simulations are regard as an embarrassingly parallel problem, thereby benefiting for an enormous speed up with parallel execution compared to serial execution. For a semi-infinite media, a $\sim$ 1000$\times$ speed up was reported [108]. For a 3D representation, voxel mesh [109] and triangular mesh [110] descriptions can now also be computed using a GPUs. GPU-powered Monte Carlo simulations were used in Paper **III**.

Spherical harmonics

This method involves expanding the radiance, the source and the phase function in spherical harmonic functions. Through this expansion, the radiative transport equation can be rewritten as an infinite set of coupled equations. Truncating the series expansion after N terms yield the P_N-approximation. Depending on the numbers of terms included, the computational cost for finding a numerical solution increases rapidly [111].

Only recently, analytical solutions for an infinite isotropically scattering medium have been derived by Liemert and Kienle

[112, 113]. They write the solution as an infinite sum of Legendre polynomials and in the limit $N \to \infty$, it gives the exact solution to the radiative transport equation.

Diffusion theory

The diffusion approximation to the radiative transport equation is the most common solution method. It provided simple analytical solutions for relevant geometries and is in many cases a sufficiently good model for photon migration in tissue. Section 3.2 will in more detail present the diffusion theory.

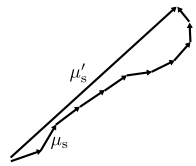

Figure 3.3. *Representation of the reduced scattering coefficient, μ_s', in terms of the scatter coefficient μ_s.*

3.2 Diffusion theory

For a complete derivation of the diffusion equation, the reader is referred to Ref [101]. In essence, it involves expanding the radiance, the source and the phase function in spherical harmonics. The series are inserted to the radiative transport equation, Eq. (3.6), yielding an infinite set of coupled equations. The P1-approximation is applied, truncating the series to only include the first-order terms. Using the quantities introduced in Sections 3.1.1, the radiance may be written as

$$L(\bar{\boldsymbol{r}}, \hat{\boldsymbol{s}}, t) \approx \frac{1}{4\pi}\Phi(\bar{\boldsymbol{r}}, t) + \frac{3}{4\pi}\boldsymbol{F}(\bar{\boldsymbol{r}}, t) \cdot \hat{\boldsymbol{s}} \tag{3.9}$$

and for the first order approximation, the phase function has no relevance.

$$p(\hat{\boldsymbol{s}}', \hat{\boldsymbol{s}}) \approx 1 \tag{3.10}$$

Further, an isotopic source is assumed

$$q(\bar{\boldsymbol{r}}, t) \approx \frac{1}{4\pi} q_0(\bar{\boldsymbol{r}}, t) \tag{3.11}$$

Inserting Eq. (3.9) into the radiative transport equation (3.6) and integrating over all solid angles, two coupled differential equations are obtained

$$\left(\frac{1}{c}\frac{\partial}{\partial t} + \mu_\mathrm{a}(\bar{\boldsymbol{r}})\right)\Phi(\bar{\boldsymbol{r}}, t) + \nabla \cdot \boldsymbol{F}(\bar{\boldsymbol{r}}, t) = q_0(\bar{\boldsymbol{r}}, t) \tag{3.12}$$

$$\left(\frac{1}{c}\frac{\partial}{\partial t} + \frac{1}{3D(\bar{\boldsymbol{r}})}\right)\boldsymbol{F}(\bar{\boldsymbol{r}}, t) + \frac{1}{3}\nabla\Phi(\bar{\boldsymbol{r}}, t) = 0 \tag{3.13}$$

where $D = 1/3(\mu_\mathrm{a} + \mu_\mathrm{s}')$ is the diffusion coefficient and $\mu_\mathrm{s}' = (1-g)\mu_\mathrm{s}$ the reduced scattering coefficient. The reduced scattering coefficient is the equivalent to the scattering coefficient with isotropic scattering (g=0), see Fig. 3.3. Now assuming that the

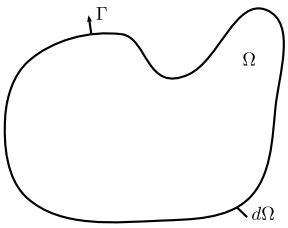

Figure 3.4. *A volume Ω with boundary dΩ with excitance Γ.*

temporal flux is negligible, *i.e.* $\partial \boldsymbol{F}(\bar{\boldsymbol{r}},t)/\partial t = 0$, Eq. (3.13) reduces to Fick's first law of diffusion

$$\boldsymbol{F}(\bar{\boldsymbol{r}},t) = -D(\bar{\boldsymbol{r}})\nabla\Phi(\bar{\boldsymbol{r}},t) \tag{3.14}$$

Now inserting Eq. (3.14) into Eq. (3.12), yields the diffusion equation,

$$\frac{1}{c}\frac{\partial\Phi(\bar{\boldsymbol{r}},t)}{\partial t} - \nabla D(\bar{\boldsymbol{r}})\nabla\Phi(\bar{\boldsymbol{r}},t) + \mu_{\mathrm{a}}(\bar{\boldsymbol{r}},t)\Phi(\bar{\boldsymbol{r}},t) = q_0(\bar{\boldsymbol{r}},t) \tag{3.15}$$

with the steady-state equation given as

$$-\nabla D(\bar{\boldsymbol{r}})\nabla\Phi(\bar{\boldsymbol{r}}) + \mu_{\mathrm{a}}(\bar{\boldsymbol{r}})\Phi(\bar{\boldsymbol{r}}) = q_0(\bar{\boldsymbol{r}}) \tag{3.16}$$

3.2.1 Simplifications

Two simplifications were made to reach the diffusion equation, which will constrain its applicability. The first approximation, that the temporal photon flux is negligible, is automatically fulfilled for steady-state photon migration and for time-dependent migration it has been shown that the requirement $\mu_{\mathrm{s}}' c \gg \omega$ must be fulfilled [114]. It is stating that the photon scattering frequency must be much larger than the source modulation frequency. The second approximation was to consider only isotropic sources. For a source to be regarded as isotropic, sufficiently many scattering events must have taken place to make it appear isotropic before the approximation is valid. This requirement is fulfilled after a propagation distance of $1/\mu_{\mathrm{s}}'$, at which the photon migration can be approximated as diffuse photon migration. Furthermore, for the diffusion equation to be valid, an albedo close to unity is required, $\mu_{\mathrm{s}}' \gg \mu_{\mathrm{a}}$.

3.2.2 Boundary condition

For a volume Ω with boundary $d\Omega$ the exitance through a point $\xi \in d\Omega$, see Fig. 3.4, on the boundary is given by [115]

$$\Gamma(\xi,t) = -cD(\xi,t)\hat{\boldsymbol{n}}\cdot\nabla\Phi(\xi,t) \tag{3.17}$$

where $\hat{\boldsymbol{n}}$ is the normal to $d\Omega$. A common type of measurement $M(\xi)$ is to integrate the exitance over time.

$$M(\xi) = \int_0^\infty \Gamma(\xi,t)dt \tag{3.18}$$

Imposing a Dirichlet boundary condition is straight-forward

$$\Phi(\xi,t) = 0 \tag{3.19}$$

but is not a good physical description in many cases, since it describes a boundary of perfect absorbers. A more realistic approach is a Robin-type boundary condition

$$\Phi(\xi,t) + 2D\hat{\boldsymbol{n}} \cdot \nabla\Phi(\xi,t) = 0 \tag{3.20}$$

which can be thought of as having a non-scattering medium surrounding the volume Ω. To incorporate a refractive index mismatch at the boundary, a modified Robin-type boundary condition is used

$$\Phi(\xi,t) + 2AD\hat{\boldsymbol{n}} \cdot \nabla\Phi(\xi,t) = 0 \tag{3.21}$$

where A is a parameter deduced from Fresnel's equations [116] and given as

$$A = \frac{2/(1-R_0) - 1 + |\cos(\theta_c)|^3}{1 - |\cos(\theta_c)|^2} \tag{3.22}$$

$$R_0 = \frac{n_1 - n_0}{n_1 + n_0} \quad , \quad \sin(\theta_c) = \frac{n_0}{n_1} \tag{3.23}$$

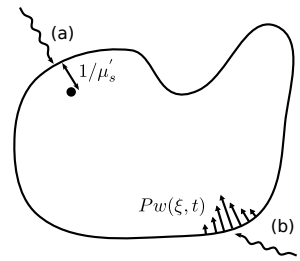

Figure 3.5. *Illustration of two possible ways of representing a source. (a) A point source at depth $1/\mu_s'$ or (b) as a photon current $Pw(\xi,t)$.*

3.2.3 Source representation

Two source discriptions are presented in Fig. 3.5. Since the diffusion equation is excellent at describing isotropic point sources, an attractive approach for modeling any type of light source is to describe it with points. A commonly used geometry is a collimated laser beam normally incident on the tissue surface or that of an optical fibre in contact with the tissue surface. Both these types of geometries are good examples where the source can be approximated as a point positioned at a depth $1/\mu_s'$ from the surface [117]. At large distances compared to the transport mean free path length, the influence of the source description on the solution to the diffusion equation is weak and a point source description is usually sufficient. At closer distances, or where the geometry is more complex, an alternative source description can be used for trying to extent the validity of the diffusion equation. One way is to modify the boundary condition in Eq. (3.21) to incorporate a photon flux[115] as the source.

$$\Phi(\xi,t) + 2AD\hat{\boldsymbol{n}} \cdot \nabla\Phi(\xi,t) = -Pw(\xi,t) \tag{3.24}$$

Here P is the strength of the source and $w(\xi,t)$ a weighting function describing the source shape on the boundary.

3.2.4 Solutions to the diffusion equation

For simple geometries, analytical solutions to the diffusion equation exist. Here the cases for an infinite homogenous medium as well as a semi-infinite homogenous medium are presented.

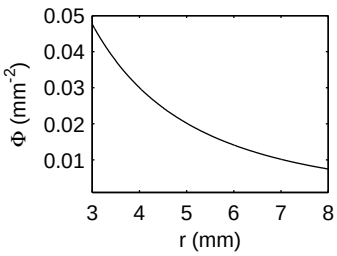

Figure 3.6. *Solution to the diffusion equation for an inifite homogenous medium with paramters* $\mu_s' = 1mm^{-1}$ *and* $\mu_a = 0.01mm^{-1}$.

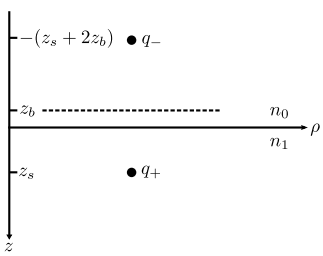

Figure 3.7. *Semi-infinite geometry with extrapolated boundary conditions.*

Infinite homogeneous medium

For an infinite isotropically scattering medium, an analytical solution to the diffusion equation can be found. Given a point source with power P_0, the source term can be expressed as $q_0 = P_0\delta_r$. Under these conditions, the steady-state diffusion equation, Eq. (3.16), reduces to.

$$-D\nabla^2\Phi(\bar{\boldsymbol{r}}) + \mu_a\Phi(\bar{\boldsymbol{r}}) = P_0\delta_r \tag{3.25}$$

The solution is plotted in Fig. 3.6 and given by

$$\Phi(r) = P_0\frac{1}{4\pi Dr}\exp(-\mu_{\text{eff}}\, r) \tag{3.26}$$

where the μ_{eff} is the *effective attenuation coefficient* and is given by

$$\mu_{\text{eff}} = \sqrt{\frac{\mu_a}{D}} \tag{3.27}$$

Similarly, for a point source both in time and space, $q_0 = E_0\delta_r\delta_t$, a time-dependent analytical solution can be found.

$$\Phi(r,t) = cE_0\left(\frac{1}{4\pi Dct}\right)^{3/2}\exp\left(\frac{-r^2}{4Dct} - \mu_a ct\right) \tag{3.28}$$

There are only a few geometries which may be considered as an infinite homogenous medium. Interstitial measurements of large liquid tissue phantoms is a good example where it may be applied. It is also useful expressions for making back of the envelop calculations.

Semi-infinite homogeneous medium

A frequent encountered geometry is a the semi-infinite, where only half the space consists of a scattering medium and the second half is usually assumed to be air. In this geometry, diffuse reflections can be modeled. Here the boundary will be treated with extrapolated boundary condition, where a positive source q_+ is placed at a depth $z_s = 1/\mu_s'$ inside the scattering medium, and a second source q_-, which is a negative mirror image of the first, is placed outside the scattering medium at $z = -(z_s + 2z_b)$ to enforce the boundary. To account for a refractive index mismatch between the scattering medium and the surrounding, an extrapolated boundary at $z_b = 2AD$, at which the fluence is zero, is introduced. The fluence can thereby be written as a sum of two point sources.

$$\Phi(\bar{\boldsymbol{r}}) = \frac{P_0}{4\pi D}\left[\frac{1}{r_+}\exp(-\mu_{\text{eff}}\, r_+) - \frac{1}{r_-}\exp(-\mu_{\text{eff}}\, r_-)\right] \tag{3.29}$$

where

$$\begin{cases} r_+ = \sqrt{\rho^2 + (z - z_s)^2} \\ r_- = \sqrt{\rho^2 + (z + z_s + 2z_b)^2} \end{cases} \tag{3.30}$$

A solution to the diffusion equation can also be obtained for the more general case of an N-layered geometry. In the Fourier domain, an analytical solution of the fluence rate can be found for all layers. An inverse Fourier transform for the N-layered fluence rate have not been presented, but a numerical computation can swiftly be performed [118, 119].

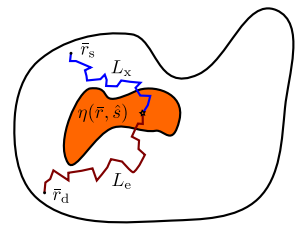

Figure 3.9. *A illustration of fluorescence migration.*

Finite element methods

For even more complex shapes and for describing heterogeneities, the finite element method (FEM) is typically applied. By describing the geometry using a mesh composed of triangular and or tetrahedral elements, realistic models of, for example, small animals may be made. See Fig. 3.8 for an example. For solving the diffusion equation for photon migration using the FEM, several software packages have been made available by the research community. In the work presented here TOAST [115, 120, 121] and NIRFAST have been used [122, 123].

3.3 Fluorescence migration

All of the theory of photon migration applies to fluorescence migration. To describe the fluorescence emitted by a fluorophore embedded in a turbid media, both the excitation and emission photon migration needs to be considered. See Fig. 3.9 for an illustration of a general case. Given an excitation a detector placed at $\bar{\boldsymbol{r}}_\mathrm{d}$ and a fluorophore distribution given by $\eta(\bar{\boldsymbol{r}}, \hat{\boldsymbol{s}})$, the emission fluence rate at the detector position can be written as

$$\Phi_\mathrm{e}(\bar{\boldsymbol{r}}_\mathrm{d}) = \int_V L_\mathrm{x}(\bar{\boldsymbol{r}}, \hat{\boldsymbol{s}}; q_\mathrm{x}(\bar{\boldsymbol{r}}_\mathrm{s}))\eta(\bar{\boldsymbol{r}}, \hat{\boldsymbol{s}})\Phi_\mathrm{e}(\bar{\boldsymbol{r}}_\mathrm{d}; \bar{\boldsymbol{r}}, \hat{\boldsymbol{s}})\, dV \tag{3.31}$$

where $L_\mathrm{x}(\bar{\boldsymbol{r}}, \hat{\boldsymbol{s}}; q_\mathrm{x}(\bar{\boldsymbol{r}}_\mathrm{s}))$ describes the excitation radiance from a source $q_\mathrm{x}(\bar{\boldsymbol{r}}_\mathrm{s})$ located at $\bar{\boldsymbol{r}}_\mathrm{s}$ and $L_\mathrm{e}(\bar{\boldsymbol{r}}_\mathrm{d}; \bar{\boldsymbol{r}}, \hat{\boldsymbol{s}})$ the emission radiance received at the detector position. An integration is performed to account for fluorescence emission contributions from the entire volume. To evaluate the integral, the escape route for every fluorophore location needs to be calculated, something that becomes tedious to compute. Instead, the reciprocity theorem is used, giving

$$\Phi_\mathrm{e}(\bar{\boldsymbol{r}}_\mathrm{d}; \bar{\boldsymbol{r}}, \hat{\boldsymbol{s}}) = L_\mathrm{e}(\bar{\boldsymbol{r}}, -\hat{\boldsymbol{s}}, q_\mathrm{e}(\bar{\boldsymbol{r}}_\mathrm{d})) \tag{3.32}$$

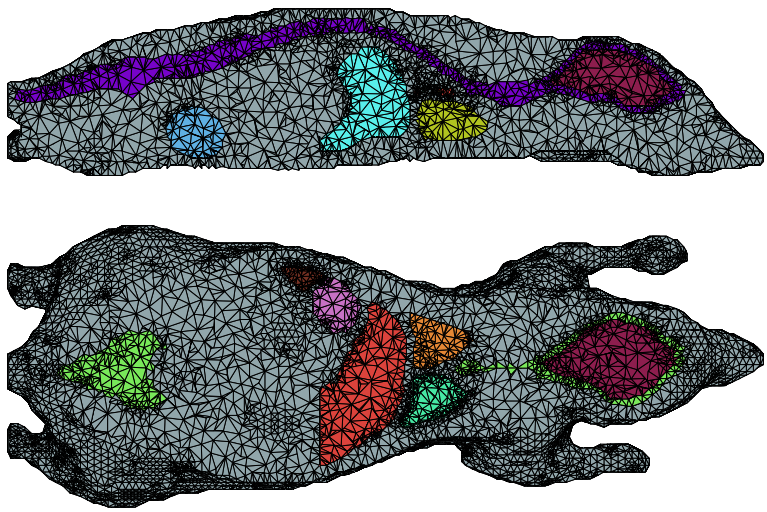

Figure 3.8. *FEM mesh of the freely available Digimouse [124].*

which simplifies the integration tremendously. It states that the emission photon migration contributions from any location in the volume reaching detector position $\bar{\boldsymbol{r}}_{\mathrm{d}}$, will be equal to the emission reaching back to that location from a source located at the detector position $q_{\mathrm{e}}(\bar{\boldsymbol{r}}_{\mathrm{d}})$. Using reciprocity, Eq. (3.31) can now be expressed as

$$\Phi_{\mathrm{e}}(\bar{\boldsymbol{r}}_{\mathrm{d}}) = L_{\mathrm{x}}(\bar{\boldsymbol{r}}, \hat{\boldsymbol{s}}; q_{\mathrm{x}}(\bar{\boldsymbol{r}}_{\mathrm{s}}))\eta(\bar{\boldsymbol{r}}, \hat{\boldsymbol{s}})L_{\mathrm{e}}(\bar{\boldsymbol{r}}, -\hat{\boldsymbol{s}}, q_{\mathrm{e}}(\bar{\boldsymbol{r}}_{\mathrm{d}})) \tag{3.33}$$

which is fast to compute in comparison to Eq. (3.31). In essence, solving the fluorescence migration boils down to solving the photon migration for the excitation source and the emission photon migration from a virtual source place at the detector position. For solving the radiative transport equation, any of the method presented in Section 3.1.4 may be used.

Chapter 4

Fluorescence imaging and tomography

Fluorescence imaging in tissue [17, 18, 125, 126] can be performed at different length-scales, from nanometers to centimeters and every step in between, by employing different technologies, *i.e.* optical nanoscopy [29], optical projection tomography [30], two-photon fluorescence microscopy [31] and fluorescence diffuse optical tomography (fDOT) [32]. Fluorescent probes were introduced in Chapter 2 and this chapter will deal with how to measure fluorescence in the diffuse domain.

4.1 Measureables

A fluorescence signal may be measured in several different ways. Straightforward is to collect the emitted intensity, which is a measure of the fluorescent yield. A slightly more sophisticated approach is to conduct a time-resolve measurement of the fluorescence intensity, by which the fluorescence lifetime may by quantified. By varying the excitation wavelength, or by dispersing the fluorescence emission, the absorption or emission spectra of a fluorophore can be found, respectively. For exotic fluorophors like upconvering nanoparticles, a non-linear intensity dependence can be measured. Here follows an overview of the different fluorescence measureables.

4.1.1 Intensity

Measuring the intensity is the most sensitive approach of reading the fluorescence signal, since all of the the collected fluorescence induced photons contribute to the signal and the fluorophore is continuously excited. Early examples of macroscopic fluorescence

imaging for medical applications include work by Alfano *et al.*[127], Montán *et al.*[128] and Andersson *et al.*. [129]. For a early example of fluorescent imaging of inclusions embedded deeply in a scattering medium, Oleary *et al.*[130] measured and modeled the reemitted signal. Early tomographic imaging of fluorescence was presented by Chang *et al.*[131].

4.1.2 Lifetime and time-gated detection

By measuring the fluorescence intensity on the timescale relevant for fluorescence emission processes, usually in the nanosecond regime for dye fluorophores, the fluorescence lifetime can be retrieved. A measurement of the fluorescent lifetime can be used to map parameter such as pH and Ca^{2+} [132]. Advantages of measuring the fluorescent lifetime, compared to the intensity, include that it is independent of the fluorophore concentration and that the difference in propagation lengths induced by the scattering can usually be neglected. For diffuse imaging, a number of phantom experiments measuring the fluorescent lifetime have been performed[133–137].

Through fluorescent lifetime measurements at multiple wavelength, the Förster (or fluorescence) resonance energy transfer (FRET) can be retrieved. The FRET process occurs via non-radiative transfer from a donor fluorophore to an acceptor fluorophore. FRET is sensitive to molecular associations and separations in the 1-10 nm range, a length scale relevant to most biomolecules [138]. In diffuse imaging, a couple of different demonstration of FRET imaging have been reported [139–141].

Another approach to using the time-dependence of the fluorescent signal have been to collect only the early arriving photons, *i.e.* snake photons. Here time-gates faster then the fluorescence lifetime is used to separately detect photons traveling in semi-straight path. This method was first exploited for absorption diffuse imaging [142, 143], where today the complete time characteristics is used instead [144, 145], but have lately gain attraction for fluorescence diffuse imaging [146, 147].

4.1.3 Emission/excitation spectra

A third alternative is to measure the fluorescence emission spectrum or indirectly probe the extinction spectrum of a fluorophore through measurements of the fluorescence emission at different excitation wavelengths. For fluorescent organic molecules, the extinction and emission spectra of the fluorophore itself are usually mirror images, as discussed in Section 2.3, thereby making simulationus excitation and emission measurements redundant. However, the tissue optical properties may vary between the two different wavelength regions and can thereby indirectly provide information

about the tissue. For non-organic fluorophores, the mirrored extinction/emission spectra does not hold any more.

The fluorescence emission at different wavelength can for example be used to separate the signal originating from a fluorescent probe from that of tissue autofluorescence [128]. For bioluminescence tomography, recordings of the emission spectrum have improved the image quality [148, 149]. Cherry *et al.*[150] hypothesized that measuring the fluorophore emission spectrum could improve on the fluorescence tomography image quality, something that have been explored in Paper **I** and later also investigated by Cherry *et al.*[151]. In two papers, Klose reports on the use of quantum dots for excitation-resolved fluorescence tomography [152, 153], where the wide absorption band of quantum dots have been utilized.

4.1.4 Non-linear intensity

All the fluorescent measureables mentioned until now have assumed a linear relationship between the excitation intensity and the emission intensity.

$$I_f \propto I_x^{\beta} \tag{4.1}$$

That corresponds to $\beta = 1$ in Eq. (4.1), where I_f is the fluorescence intensity and I_x the excitation intensity. In some particular cases one can obtain non-linear intensity dependences, corresponding to for instance $\beta = 2$, which takes place in *e.g.* 2-photon fluorescence or while using upconverting crystals. The direct 2-photon excited fluorescence yield is most often very weak in comparison to the efficiency of upconverting materials. Thereby, for diffuse tissue imaging, characterized by low excitation fluence rates, upconverting materials is the only feasible option today for producing non-linear fluorescence emission.

Papers **II**, **III**, **IV** and **V** all make use of the non-linear induced fluorescence. Other reports on upconverting materials for diffuse fluorescence imaging include references: [154–165]. In a letter by Liu *et al.*[166], an original use of the non-linearity was exploited by using two spatially displaced excitation sources, thereby creating a third virtual source, given by the cross-product of the two real sources.

4.1.5 Alternative measurebles

An alternative fluorescent measure is dynamic imaging. By measuring the time evolution of a fluorescent probe administrated to an animal, uptake in individual organs can be followed [167–170]. Dynamics on the a second timescale can be resolved, which is a relevant timescale for biological processes.

4.2 Imaging geometries

The different imaging geometries used for collecting fluorescent light can be divided in three categories, epi-illumination, transillumination and projection geometries. No universal imaging geometry exist, partly due to the heavy scattering of light in the NIR spectral region, which limits the use of straight-path projections, and partly because different applications can benefit from different imaging setups.

4.2.1 Epi-illumination

Epi-illumination refers to a geometry were both the source and detectors are placed on the same side of the tissue. Either wide-field illumination, raster scanning of a point source, or something in between the two, *i.e.* a line source, is employed. Detection is preferable done by imaging, but could also be performed point-by-point.

An epi-illumination geometry will be sensitive to superficial signals. It is also the geometry which will generate the highest flux of fluorescent photons. Using a combination of wide-field illumination and imaging-based detection will allow high speed imaging. On the other hand, an epi-illumination geometry is extra sensitive to excitation light leakage and autofluorescence from the tissue, two common issues encountered with florescence imaging systems.

4.2.2 Transillumination

A transillumination geometry is where the source and detector have been placed on opposite sides of the tissue. Similar illumination and detection scheme to that of epi-illumination are incorporated. A common combination is a point source together with imaging-based detection [171, 172].

A transillumination geometry cannot always be used, simply because the tissue might be too thick. In contrast to an epi-illumination geometry, issues like excitation light leakage and autofluorescence are naturally minimized due to the attenuation of the tissue itself. Also, a more even sensitivity throughout the whole tissue is achieved, even though the depth-sensitivity is usually limited. Moreover, raster scanning of a point source allows for tomographic image evaluations.

4.2.3 Projection

A projection imaging geometry seeks to mimic the approach of x-ray computed tomography by illuminating the tissue from 360 degrees. Commonly this is done by point sources and an imaging detector [173–175] or by point sources and point detectors [28, 176].

A projection imaging geometry requires the most complex instrumentation and the imaging speed is slow compared to other imaging geometries. In return it gives close to an even sensitivity for the whole tissue and excitation light leakage and autofluorescence can be avoided equally well as in a transmission geometry.

4.2.4 Spatial frequency domain imaging

Illumination patterns employed in fluorescence imaging are usually simple, either point sources or wide-field illumination. An exception is the use of spatial frequency illumination patterns. First introduced for absorption imaging [177], it has also later been applied for fluorescence imaging and tomography [178–180].

4.3 Tomographic imaging

Tomographic imaging seeks to describe the interior of a scattering media only using light exiting across the boundary. By constructing a model of the media, that is as close to the reality as possible, and calculating the light propagation through it, simulated measurements that resembles the real measurements are created. This is called the *forward model*, and can written as

$$\mathcal{F}(\boldsymbol{\eta}) = \mathcal{M}(\Phi(\boldsymbol{\eta})) \tag{4.2}$$

where the vector $\boldsymbol{\eta} = [\eta_1, \eta_2, \cdots, \eta_N]$ represent the fluorophore distribution in N image voxels, Φ is the fluence generated by the given fluorophore distribution and $\mathcal{M}$ is the measurement operator, describing in which way the fluorescent signal was measured. This model may be constructed in many ways as discussed in Section 3.1.4, but can generally be noted with $\mathcal{F}(\boldsymbol{\eta})$. Within a model-based framework, the *inverse problem*, which seeks to create a tomographic image is possed as an optimization problem. By comparing the forward model to a set of M measurement $\mathbf{y} = [y_1, y_2, \cdots, y_M]$, the level of agreement between the two can be stated with an objective function, usually on the form

$$\chi^2 = \frac{1}{2}\|\mathbf{y} - \mathcal{F}(\boldsymbol{\eta})\|^2 \tag{4.3}$$

Here χ^2 denotes the goodness of the fit between the model and the measurements. A reconstructed image, $\hat{\boldsymbol{\eta}}$, can then be found by minimizing the objective function with respect to the fluorophore distribution.

$$\hat{\boldsymbol{\eta}} = \arg\min_{\eta} \frac{1}{2}\|\mathbf{y} - \mathcal{F}(\boldsymbol{\eta})\|^2 + \lambda\frac{1}{2}\|L(\boldsymbol{\eta})\|^2 \tag{4.4}$$

To find a valid solution, the objective function is modified to include a regularization term, $L(\boldsymbol{\eta})$, with regularization parameter

λ. The regularization may be chosen in many ways, something that is disused in Section 4.3.1.

The standard norm, in which Eq. (4.4) is evaluated, is the Euclidean norm and a minimization and thus a solution, is found where the derivative with respect to η is zero.

$$\nabla \left(\frac{1}{2}(\mathbf{y} - \mathcal{F}(\boldsymbol{\eta}))^2 + \lambda \frac{1}{2} L(\boldsymbol{\eta})^2 \right) = 0 \tag{4.5}$$

Expanding both the forward model and the regularization in a Taylor series around $\boldsymbol{\eta}_0$ and truncating it to only include the first order terms gives

$$\mathcal{F}(\boldsymbol{\eta}) \approx \mathcal{F}(\boldsymbol{\eta}_0) + \nabla \mathcal{F}(\boldsymbol{\eta}_0) \Delta \boldsymbol{\eta} \tag{4.6}$$

$$L(\boldsymbol{\eta}) \approx L(\boldsymbol{\eta}_0) + \nabla L(\boldsymbol{\eta}_0) \Delta \boldsymbol{\eta} \tag{4.7}$$

Putting equations Eq. (4.6) and Eq. (4.7) into Eq. (4.5), and introducing the Jacobian matrix as

$$\mathbf{J} = \begin{pmatrix} \frac{\partial \mathcal{F}_1}{\partial \eta_1} & \cdots & \frac{\partial \mathcal{F}_1}{\partial \eta_N} \\ \vdots & \ddots & \vdots \\ \frac{\partial \mathcal{F}_M}{\partial \eta_1} & \cdots & \frac{\partial \mathcal{F}_M}{\partial \eta_N} \end{pmatrix} \tag{4.8}$$

yeilds

$$\Delta \boldsymbol{\eta} = (\mathbf{J}^{\mathrm{T}} \mathbf{J} + \lambda \mathbf{L}^{\mathrm{T}} \mathbf{L})^{-1} \mathbf{J}^{\mathrm{T}} (\mathbf{y} - \mathcal{F}(\boldsymbol{\eta}_0)) \tag{4.9}$$

where the regularization matrix $\mathbf{L}$ is formed similar to $\mathbf{J}$. Solving Eq. (4.9) gives an update of the fluorophore distribution. In calculating the derivative $\nabla \mathcal{F}(\boldsymbol{\eta})$, the first order Born-approximation is usually applied, assuming that the excitation field and the emission field are not dependent on the fluorophore distribution, which holds for low concentration of the fluorophore [133]. In this way, the derivative simplifies to

$$\nabla \mathcal{F}(\boldsymbol{\eta}) = \nabla (\Phi_{\mathrm{x}} \boldsymbol{\eta} \Phi_{\mathrm{e}}) = \Phi_{\mathrm{x}} \Phi_{\mathrm{e}} \tag{4.10}$$

Two common modifications to this approach of forming the inverse problem, is firstly, the use of a normalized Born-approximation [181, 182], where the fluorescence measurement is normalized with the transmitted excitation,

$$\Gamma_{\mathrm{e}} \to \frac{\Gamma_{\mathrm{e}}}{\Gamma_{\mathrm{x}}} \quad , \quad \mathbf{J} \to \frac{1}{\Gamma_{\mathrm{x}}} \mathbf{J} \tag{4.11}$$

and secondly, to use the logarithm of the emission data [183]

$$\Gamma_{\mathrm{e}} \to \log \Gamma_{\mathrm{e}} \quad , \quad \mathbf{J} \to \frac{1}{\boldsymbol{\eta}} \mathbf{J} \tag{4.12}$$

4.3.1 Regularization

For diffuse imaging, the inverse problem is ill-posed, that is, a small change in the parameter $\boldsymbol{\eta}$ may give a large difference to the simulated data $\mathcal{F}(\boldsymbol{\eta})$. This is a property inherent from the strong scattering. It can be understood from the point that a particular fluorophore may contribute to the fluorescence existence for many detectors. Also, the problem is usually under-determined, that is, there a fewer measurements than unknowns (image pixels or voxels). This clearly dependence on the reconstruction basis used and the number of measurements acquired. But even with the use of mega-pixel CCD camera as detectors, the problem may remain under-determined, since it is only the number of linearly independent measurements that counts.

To stabilize the solution, regularization is incorporated, which, can be viewed as a smoothing of the solution. With regularization added to the objective function, a reconstructed image is now a solution to the sum of the data objective function and the regularization objective function. The regularization parameter decides how much of the regularization terms that should be added to the total objective function. A small value puts trust in the data, and a large value finds a solution to the regularization term and not the data.

A straightforward way of regularizing the objective function is to use the identity matrix $\mathbf{L} = \mathbf{I}$. This is called a Tikhonov regularization. It will add an equal penalty or smoothing to all voxels in the image. An alternative, introduced by Levenberg-Marquardt, use $\mathbf{L} = \text{diag}(\mathbf{J}^{\mathrm{T}}\mathbf{J})$, which will add regularization in correspondence with the sensitivity profiles. In voxels with a high sensitivity a high regularization is added, and for low sensitivity voxels a low regularization is added. This type of regularization thus compensates for the inhomogeneous sensitivity profiles always present in diffuse imaging. In an other approach to compensate for the high surface sensitivity of a cylinder geometry, Pogue *et al.*[184], used a radial scaling regularization.

Data-driven regularization

The data itself may also be used to create a regularization matrix. Axelsson *et al.*[185] presented a method where the ratio of two emission wavelengths were used to form the regularization matrix. The idea originates from a paper by Swartling *et al.*[186], who quantifies the fluorescence emission spectral change as a function of propagation distance. The inverse, that is, a depth estimation dependent on the fluorescence spectral data was used to create a spatially varying regularization. This approach was also investigated in Paper **VIII**, now in conjunction with upconverting nanoparticles.

Multi-modality regularization

A recent track of development have been to combine functional low resolution fluorescence imaging with high-resolution anatomical images captured with X-ray computed tomography (XCT) [27, 187, 188] or magnetic resonance imaging (MRI) [189]. The anatomical data is used to improve on the forward model by taking the tissue heterogeneity into account. For the inverse problem, the anatomical data can be incorporating into the regularization, and thereby improve on the image quality. A couple of different approaches have been investigated. Davis *et al.*[189] introduced a segmented regularization matrix corresponding to the anatomical data. All segments were given an individual weight and borders between segments were smoothed with a Laplace filter. Hyde *et al.*[187] have added to this concept by using weighted segment regularization. Here the miss-match in resolution between the two imaging modalities was taken into account by using weighted segments (a pixel in the fluorescence image may overlap with more than one tissue type in the anatomical image).

4.3.2 Solving the tomographic problem

Finding a solution to the tomographic problem boils down to solving a set of linear equation, which is done numerically. In the way the least square optimization is posed in Eq. (4.9), the Hessian takes the size $[N \times N]$. Typically the Hessian is dense and non-symmetrical. If the number of voxels in the reconstruction image are few, the inverse can be computed with a direct method like LU-factorization. If a lot of measurements are used, or if the voxels in the reconstruction image are many, the size of the Jacobian $[M \times N]$ may be too large to hold in the memory[1]. To avoid construction of the complete Jacobian, gradient methods can be used to solve the inverse. Typically Krylov methods like conjugate gradient or generalized minimal residual methods are employed. A Krylov solver, especially design for the fluorescence tomography inverse problem, was design in Paper **I**. It was implemented with a generalized minimal residual method and has the benefit of having the same computational cost irregardless of the number of measurements used.

4.4 Applications

Fluorescence imaging have been applied for preclinical applications, such as, visualizing tumor-associated lysosomal protease activity in xenograft mice by activatable NIRF probes [19]. In improving the binding affinity, multivalent nanoparticles with multiple legends and a conjugated fluorescent probe were used to image

[1] On 32-bits machines: $2^{32} \sim$ 4GB, and on 64-bits machines: $2^{64} \sim$ 20EB

pancreatic cancer models in mice [190]. Other examples include the use of peptide-labeled quantum dots for imaging tumor vasculature [191] and protein-protein interaction visualized through bioluminescence imaging[192]. Mice expressing GFP have also been imaged [193]. Recently, atherosclerotic plaques in a rabbit animal model were reported to have an increased uptake of ICG [194].

Translation of fluorescence imaging for whole-body clinical use should be regarded as infeasible, even though otherwise have been suggested [195]. However, at locations with optical access, *i.e.* skin, eyes, blood vessels, the bladder, and others, fluorescence imaging have shown to be applicable. Clinical examples of fluorescent imaging already undertaken include among others, ICG imaging of breast cancer [14, 15, 196] and lymph nodes [197].

Chapter 5

Upconverting nanoparticles

Upconversion is a nonlinear process where anti-Stokes shifted luminescence is generated [37, 198–202]. Emission at a shorter wavelength than the excitation wavelength is created through stepwise exciting intermediate long-lived energy states. The birth of the idea is usually contributed Bloembergen[203] for his paper in 1959, where he describes the design of an infrared photon counter. Bloembergen was, however, only considering photo-excitation. Today it is known that a far more efficient upconversion processes is non-radiative transfer of energy. This concept was recognized and formulated independently by Auzel [204], and Ovsyankin and Feofilov [205] in 1966.

It was not until colloidal nano-sized upconverting particles had been fabricated [206] and the efficiency increased sufficiently [42] that their use for biomedical applications were considered. Soon after, the importance to keep a hexagonal crystal phase of the particles was pointed out [207, 208]. A discovery that gave approximately a ten-fold increase of the luminescence intensity. An other major step forward included synthesis of monodispersive nanoparticles [209, 210]. More recently, particles with an encapsulating shell have been created [211–213]. It has the benefit of shielding the active core from surface quenching, something which becomes increasingly prominent with smaller particle size [212]. Also, with decreasing particle size, the crystal phase has a tendency to transform from hexagonal into cubic phase [214]. To simultaneously control the phase and the particle size, Wang *et al.*[215] have successfully made use of Gd^{3+} doping to keep the hexagonal phase for ultrasmall nanoparticles.

The use of Gd^{3+} have also opened the door for multimodality particles. To combine optical upconversion and magnetic contrast have attracted a lot of attention. Two different pathways are persuied, either upconverting nanoparticles are co-doped with Gd^{3+} [161, 216–218], or an iron-oxide shell is grown onto the particles

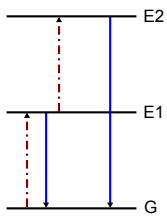

Figure 5.1. *Excited state absorption. The dashed/doted and the full lines represent photon excitation and photon emission, respectively.*

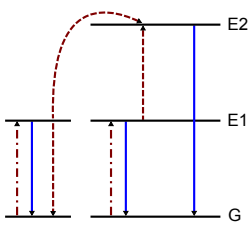

Figure 5.2. *Energy transfer upconversion. The dashed/doted, doted and full lines represent photon excitation, energy transfer and photon emission, respectively*

[157, 158].

During the last years, upconverting nanoparticles have started being used for *in vivo* studies. First demonstration was made by Chatteriee *et al.*[219]. A stream of work have since then been published, mostly presenting *in vivo* lymph node staining [158, 160, 220, 221], but also tumor-targeted imaging [163, 164]. Common to all *in vivo* studies mentioned is subcutaneous imagining. Trying to reach deeper is cumbersome, but a few non *in vivo* attempts have been made [155, 156, 165, 222], where perhaps the most drastic idea was to change the excitation wavelength from the common 980 nm to 915 nm [165].

5.1 Upconversion processes

To begin the discussion about upconverting nanoparticles, the different upconversion processes are outlined and explained. A comparison to more common nonlinear processes, such as second harmonic generation and two-photon absorption, are also made.

5.1.1 Excited state absorption

Excited state absorption (ESA), as depicted in Fig. 5.1, is the process when an ion in the excited state absorbs one more photon and is promoted to an even higher energy state.

5.1.2 Energy transfer upconversion

Energy transfer upconversion (ETU), see Fig. 5.2, resembles ESA in the way that the ion is sequentially excited. The difference is that the excitation step utilizes energy transfer between two neighboring ions, one donor and one acceptor, instead of photo-excitation. The donor ion promotes the acceptor ion to the energy level E2 by non-radiative energy transfer, while itself relaxes back to the ground state.

5.1.3 Cooperative upconversion

Cooperative upconversion, schematically drawn in Fig. 5.3, can be categorized into cooperative sensitization and cooperative luminescence. Either two sensitizers ions give their energies simultaneously to an activator ion (cooperative sensitization) or two sensitizers ions combine to give emission of a photon (cooperative luminescence).

5.1.4 Other nonlinear processes

Common other nonlinear processes, exemplified in Fig. 5.4, are second harmonic generation (SHG) and two-photon absorption.

Both involve two-photon excitation through a virtual intermediate energy level to give a photon emission of twice the energy of the excitation photon. The difference is the presence of an excited state or not. SHG does not require the presence of an excited state, whereas two-photon absorption does.

5.2 Dopants and host materials

Inorganic crystals do not naturally exhibit upconversion emission. Only carefully engineered crystals with lanthanide dopants have so far showed bright upconverting emission. For obtaining strong luminescence, two types of dopants are required; activator and sensitizer ions. The activator ion emits the luminescence, while the sensitizer ion transfers its energy to a nearby activator. Also important for bright luminescence is the host crystal. Here follows a quick look at each component.

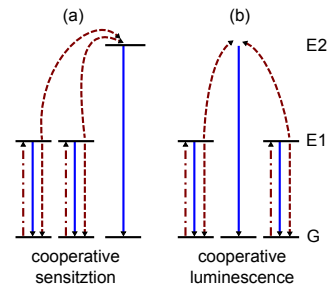

Figure 5.3. *(a) Cooperative sensitaztion and (b) cooperative luminescence. The dashed/doted, doted and full lines represent photon excitation, energy transfer and photon emission, respectively*

5.2.1 Activators

Characteristic for activators are a sharp ladder-like energy structure with meta-stable energy levels. Lanthanides offers both these features. The unique electronic configurations of lanthanides give these distinct properties. Lanthanide ions Ln^{3+} fill there electronic states $5s^2$ and $5d^6$, before the 4f-states, thereby creating a shield against electron-phonon coupling for the 4f states. This phenomena give rise to sharp and narrow f-f transitions that lay in the visible and NIR region of the spectrum. Additionally, the f-f transitions are Laporte forbidden (parity is not inverted for the transition), generating long life-times in the order of 100 ms [37]. Even though all lanthanides exhibit these properties, only a few happen to have a ladder-like energy structure within its 4f-states. Most suited are Tm^{3+}, Er^{3+} and Ho^{3+}, which all have a ladder-like energy structure. See Fig. 5.5 for an example of Tm^{3+} and Er^{3+} ions energy structure.

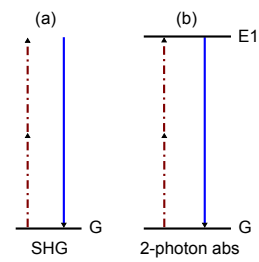

Figure 5.4. *(a) Second harmonic generation and (b) 2-photon absorption. Dashed/dotted and full lines represent photon excitation and photon emission, respectively.*

5.2.2 Sensitizers

The luminescence brightness obtainable from upconverting nanoparticles is strongly effected by the absorption cross-section and the proximity of the activator ions. Lanthanides in general do not have a large absorption cross-section. And the outlined activator ions from the previous section are not even among the strongest absorbing lanthanides. Compensating the low absorption cross-section, with an increased dopant concentration, would unfortunately, move the activator ions in too close proximity, and induce quenching by cross-relaxation. Introducing a second, sensitizer dopant will partly overcome some of these issues.

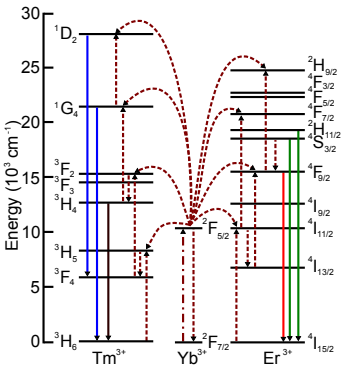

Figure 5.5. *Proposed energy transfer and excitation processes for Er^{3+} and Tm^{3+} activators with a Yb^{3+} sensitizer. Excitation is done at 980 nm. The dashed/doted, doted and full lines represent photon excitation, energy transfer and photon emission, respectively*

Typically, Yb^{3+} ions are used as sensitizers. They have approximately a two-fold larger absorption cross-section compared to Er^{3+} ions at 980 nm [223]. Additionally, Yb^{3+} ions are less susceptible to concentration-dependent quenching effects compared to other lanthanides. The reason being its simplistic 4f energy levels, with only one excitable state. Thus the dopant concentration can be increased from a few percent, the quenching threshold for non-sensitized doping, to around 20 percent [198]. And as it so happens, the $^2F_{7/2} \rightarrow {}^2F_{5/2}$ transition in Yb^{3+} corresponds well with the f-f transitions for the common activators, thereby facilitating efficient energy transfer between the ions.

5.2.3 Host materials

To accommodate the activator and sensitizer ions, a host material is needed. As with all doping, the host material needs to be lattice matched to the dopants, in this case the lanthanide ions. Suitable host materials with a similar ionic size include trivalent rare-earth ions ($Y^{3+}, La^{3+}, Gd^{3+}, Sc^{3+}$), alkali earth ions ($Ca^{3+}, Sr^{3+}, Ba^{3+}$) and certain transition metals (Zr^{3+}, Ti^{3+}) [198].

Also favorable, is a host crystal with low phonon energies to reduce multi-phonon relaxation and thereby increase the intermediate state life-times of the dopants. The lowest phonon energies are attributed with heavy halides like chlorides or bromides, but they are impracticable to use due to their hygroscopic nature. Among the halides, only the lightest fluorides like ($LaF_3, YF_3, NaYF_4$) remain a practical choice. Oxide-based crystals are also common. They are chemically more stable, but the phonon energies are typically higher [224]. By far the most common host used is $NaYF_4$, which with its low phonon energies [225] provides a suitable environment for upconvertion luminescence.

Another important parameter is the crystal structure. Kramer *et al.*[207] have shown that a hexagonal crystal structure (β-phase) is favorable to a cubic (α-phase) in terms of luminescence intensity. They observed about one order of magnitude increase in the lumiescence signal between the two crystalline structures.

5.2.4 Nanosized particles

Nanosized particles are a necessary for biological applications. The particle size will greatly influence the kinetics and distribution of the particles in biological tissue. When the physical dimension of the upconverting nanoparticles are shrunk to the nanometer scale, additional complications rise. With a smaller size, the surface to volume fraction increases fast, making a larger portion of the dopants be placed close to a surface. At the surface, the likelihood of interaction with the surrounding media is far greater, thereby easier causing quenching of the dopant ions [42, 226]. An-

other issue with the smaller size is surface tensions, which triggers phase transformation from the favorable hexagonal phase to the less beneficial cubic phase [215].

To avoid surface interaction and to shield to dopant ions, one strategy is to grow an extra shell that incapsulate the particles, see Fig. 5.6. Yi *et al.*[227] have grown ultra-small particles with an average diameter of only 10 nm, which with an extra incapsulating shell increased its luminescence intensity by 30 times. Similarly, Boyer *et al.*[228] managed to three-fold increase the luminescence intensity with 30 nm in diameter particles. In a more comprehensive study, Wang *et al.*[212] systematically changed the particle size and compared the luminescence intensity of core-shell to core-only particles. The surface quenching effect became more apparent the smaller the particles were, manifested as a larger difference in luminescence intensity. For 10 nm in diameter core particles, with or without a shell, a 450-fold increase in luminescence intensity was measured.

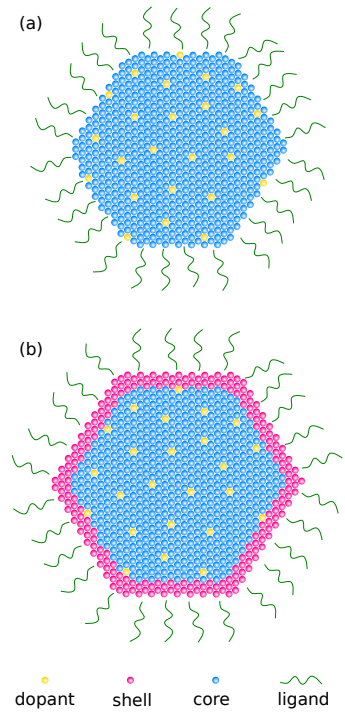

Figure 5.6. *Cartoon of a lanthanide doped nanoparticle without (a) and with (b) an encapsulating shell. With the shell, all of the dopants are situated far from the surface and can thus efficiently contribute to the upconversion process.*

5.3 Intensity dependence for upconversion luminescence

There are a variety of upconverting processes. In this section the intensity dependence for ESA and ETU will be examined with rate equation for a simplified three-level system. Following the analysis made by Pollnau *et al.*[229], helpful expression can be derived in two regimes; at low and high pump intensities. A very similar analysis is also made by Suyver *et al.*[230]. For the analysis, the following is assumed:

(i) The ground state population is constant, $dN_G/dt = 0$.

(ii) The system is pumped by continues wave (CW) light, which is resonant with the first level.

(iii) Upconversion is either ESA or ETU.

(iv) The excited states have lifetimes τ_1 and τ_2, respectively.

5.3.1 Intensity dependence for ESA

For ESA, the three-level system depicted in Fig. 5.1 is considered. The rate equations can be written as

$$\frac{dN_1}{dt} = \rho\sigma_0 N_G - \rho\sigma_1 N_1 - N_1/\tau_1 \quad (5.1)$$

$$\frac{dN_2}{dt} = \rho\sigma_1 N_1 - N_2/\tau_2 \quad (5.2)$$

where $\rho = \lambda I/hc$ is the pump-constant, which is proportional to the I, the excitation intensity and h denotes Plank's constant, c the vacuum speed of light and λ the wavelength of the excitation light. Further, σ_0 is the cross-section for ground state absorption, σ_1 the cross-section for excited state absorption and $N_{\mathrm{G},1,2}$ the population in state G, 1, 2, respectively. From Eq. (5.2), it is found that $N_2 \propto IN_1$.

Initially, the case with low pump intensity is considered. That is to say $\rho\sigma_1 N_1 < N_1/\tau_1$. It means that the spontaneous decay is dominating over ESA. In this case, the term $\rho\sigma_1 N_1$ can be neglected in Eq. (5.1) and $N_1 \propto I$ is found. Thereby, $N_2 \propto I^2$, stating that the upconverting fluorescence emission will have a quadratic power dependence.

In the other case, at a high pump intensity, meaning that $\rho\sigma_1 N_1 > N_1/\tau_1$, the spontaneous decay is instead neglected. Then from Eq. (5.1), $N_1 \propto N_{\mathrm{G}}$ is found, giving $N_2 \propto IN_1 \propto I$. Thus the upconverting fluorescence emission will have a linear power dependence.

5.3.2 Intensity dependence for ETU

For ETU, as illustrated in Fig. 5.2, the rate equations become

$$\frac{dN_1}{dt} = \rho\sigma_0 N_{\mathrm{G}} - 2WN_1^2 - N_1/\tau_1 \tag{5.3}$$

$$\frac{dN_2}{dt} = WN_1^2 - N_2/\tau_2 \tag{5.4}$$

where W describes the strength of the non-radiative energy transfer between two neighboring ions. From Eq. (5.4) it is found that $N_2 \propto N_1^2$. Similarly to the analysis of the ESA, the ETU can also be viewed in two regimes. Firstly, when the spontaneous decay from state 1 is dominating. Secondly, when the energy transfer between ions is more frequent than the spontaneous decay.

In the limit of dominating spontaneous decay, that is to say the energy transfer is inefficient, the term $2WN_1^2$ in Eq. (5.3) can be neglected. Then, $N_1 \propto I$ and thereby $N_2 \propto I^2$. Again, a quadratic power dependence for the fluorescence emission is found. In the other limit, when energy transfer is dominating, the term N_1/τ_1 is neglected in Eq. (5.3). This gives, $N_1 \propto I^{1/2}$ and consequently $N_2 \propto N_1^2 \propto I$. Hence the fluorescence emission will have a linear power dependence.

5.3.3 Summarizing the intensity dependence

The attractive processes for highly efficient and bright upconverting materials are ESA and ETU. Interestingly, both dominate in the limit of neglectable spontaneous decay. It means that long-lived intermediate states are preferable for efficient upconversion.

Process	Material	$\eta_{2p}(\mathrm{cm}^2/\mathrm{W})$
ETU	$YF_3 : Yb, Er$	$\sim 10^{-3}$
ESA	$SrF_2 : Er$	$\sim 10^{-5}$
Cooperative sensitization	$YF_3 : Yb, Tb$	$\sim 10^{-6}$
Cooperative luminescence	$Yb : PO_4$	$\sim 10^{-8}$
Second harmonic generation	KDP	$\sim 10^{-11}$
2-photon absorption	$CaF_2 : Eu^{2+}$	$\sim 10^{-13}$

Table 5.1. *Slope efficiency comparison between different multi-photon processes. Adopted from [231].*

The intensity dependence was evaluated in two limits, finding either a quadratic or a linear dependence. Naturally there will be a transition between the two regions where the power dependence will turn from quadratic into linear. The turning point would give an indication of the intermediate state life-time and thus also about the overall conversion efficiency. Saturating the intermediate state at a low intensity, that is to say finding a linear intensity dependence, would hence suggest efficient upconversion. Therefore the turning point could possible be used as in indicator for quality control.

5.4 Efficiency of the upconverting processes

To compare the different processes involved in upconversion, it is interesting to look at the efficiency of each process. In contrast to linear processes, the efficiency is not given as a quantum yield (percentage), since the absolute conversion fraction depends on the excitation intensity. Instead the slope efficiency is usually reported and it is defined as

$$\eta_{2p} = \frac{I(\lambda_f)}{I(\lambda_e)^2} \tag{5.5}$$

where $I(\lambda_f)$ and $I(\lambda_e)$ is the fluorescence and excitation intensity, respectively. For a comparison of the slope efficiency between the different multi-photon processes outlined earlier, see Table 5.1. The slope efficiency tells which nonlinear process that will dominate at moderate intensities, rather than give the maximum photon conversion possible. As an example, second harmonic generation conversion above 80% in KDP at an excitation intensity of ~ 100 GW/cm^2 have been reported[232], even though the slope efficiency is low. The 80% conversion efficiency is with regards to the energy.

For upconverting materials intended for biological use, the intensity needs to be kept much lower, typically not exceeding ~ 100 mW/cm^2 to not harm the tissue. In this regime, ETU is regarded as the most efficient multi-photon process [37, 198]. Only

Activator	wavelength (nm)
Er^{3+}	411 (W)
	523 (S)
	542 (S)
	656 (S)
Tm^{3+}	450 (S)
	475 (S)
	647 (W)
	800 (S)
Ho^{3+}	540 (S)
	750 (W)
	800 (W)

Table 5.3. *Common emission wavelength for typical activator ions used for upconverting nanoparticles. Excitation was done at 980 nm in all cases. Values are taken from Ref. [198, 234]*

Material	Emission color	Excitation intensity (W/cm^2)	Peak efficiency conversion (%)	η_{2p} (cm^2/W)	Ref
$NaYF_4 : Yb, Er$	green	$\sim$ 100	4	$\sim 10^{-2}$	[43]
$NaYF_4 : Yb, Tm$	blue	$\sim$ 100	2	-	[43]
$\beta - NaYF_4 : Yb, Er$	all	$\sim$ 20	3	-	[228]
$\alpha - NaYF_4 : Yb, Er$	green	-	6	-	[233]

Table 5.2. *Peak conversion and slope efficiency comparison between different upconverting materials.*

a few reports exist on the conversion efficiency for upconverting materials, see Table 5.2. Usually the peak conversion efficiency is reported and not the efficiency at different excitation intensities. One exception is Page *et al.*[43], where the conversion efficiency for a range of excitation intensities are given. For an intensity of ~ 100 mW/cm^2 a conversion of the order of a few percent is given for both Tm^{3+} and Er^{3+} dopants. One should note that the samples used were not in pure hexagonal phase and contained quite a lot of impurities, both known to decrease the conversion efficiency [207, 208].

5.5 Multi-color luminecence emission

To address biologically relevant question using upconverting nanoparticles, a necessary feature is the ability to multiplex the signal. By multiplexing, several biological pathways can be monitored simultaneously, giving the possibility to more in-depth studies. A straight-forward way to multiplex the signal is to shift the emission wavelength. This can be done in different ways, the most common being the use of different doping ions. Typically Er^{3+} or Tm^{3+} and sometimes Ho^{3+} are used as activators, all giving slightly different emission lines. A summery of the emission wavelengths accessible can be seen in Table 5.3.

To further multiplex the signal, more sophisticated constructions can be made. For example, Cheng *et al.*[221] have manipulated the concentrations ratios of the sensitizer and the activator ions to vary the strength of the emission lines. By doing so, the use of only two activator ions can be turned into a three-level multiplex. Yet another approach is the to introduce Li^{3+} doping, which also will shift the ratio of the emission lines [235]. A slightly different route is to combine the upconverting nanoparticles with either quantum dots [211] or organic dyes [159, 236]. A non-radiative transfer of energy between the upconverting nanoparticles and the quantum dot or the organic dye occurs, enabling fluorescence emission from the quantum dot or the organic dye. This processes is usually named luminescence resonant energy transfer (LRET) and make it possible to reach more and new emission wavelengths.

Host crystal	Sensitizer dopant	Activator dopant	Shell encapsulated	Paper
$NaYF_4$	Yb^{3+}	Tm^{3+}	no	**II**
$NaYF_4$	Yb^{3+}	Tm^{3+}	no	**III**
$NaYF_4$	Yb^{3+}	Tm^{3+}	yes	**IV**
$NaYF_4$	Yb^{3+}	Er^{3+}	yes	**V**

Table 5.4. *Properties of the different upconverting nanoparticles used in this thesis.*

5.6 Toxicity

One critical question to address with new contrast agents is the toxicity. This also holds for upconverting nanoparticles. To begin with, the particles themselves are inert nano-sized crystal and as such they have no tendency to react with its environment at atmospheric pressure and body temperature. Therefore they are very unlikely to be biodegradable. Still the particles may induce toxicity by its presence. A cell cannot hold an infinite amount of particles. Parameters plausible to affect the toxicity are dose, particle size and coating. Until today no study have screened for all these parameters, but a few reports exits related to the toxicity of upconverting nanoparticle[162, 237–239].

Nam *et al.*[239] have demonstrated internalization of upconverting nanoparticles in living cells and were able to track the particles within the cell for 6 hours without inducing necrosis. Lim *et al.*[238] feed upconverting nanoparticles to *C. elegance* for up to 6 hours and compared survival to both a control and carboxylated gold nanoparticles. They observed a marginal decrease of survival for a high dose (10 mg/ml). Otherwise no toxicity could be noted. A more relevant model for investigating toxicity is mice. Until today, two reports exist on toxicity in mice [162, 237]. Both followed mice for a time-period of at least 3 months and evaluated the toxicity by performing histology, hematology and serum biochemistry. None found any indication of evident toxic effects.

To summarize, no apparent toxic effect of upconverting nanoparticles have yet been showed. More studies are needed to determine the precise characteristics attributed to non-toxic upconverting nanoparticles.

5.7 Particles used in this work

A summery of the different particles used throughout this work is given in Table 5.4. The core particle have been produced with a coprecipitation method following a recently reported user-friendly synthetic procedure [240]. All have incorporated the same host crystal, $NaYF_4$. With its low phonon energies, it has proven to be one of the most efficient upconverting hosts available [225]. Also

only one type of sensitizer dopant have been used, Yb^{3+}. It is the a common choice of sensitizer [42, 207, 215], due to its large absorption cross-section and absence of multiple excitable f-states. Two different activator dopants were explored, with Tm^{3+} being the primary choice for its superior tissue-penetrating emission. The second option, Er^{3+}, was utilized for its dual emission lines within the tissue-optical window.

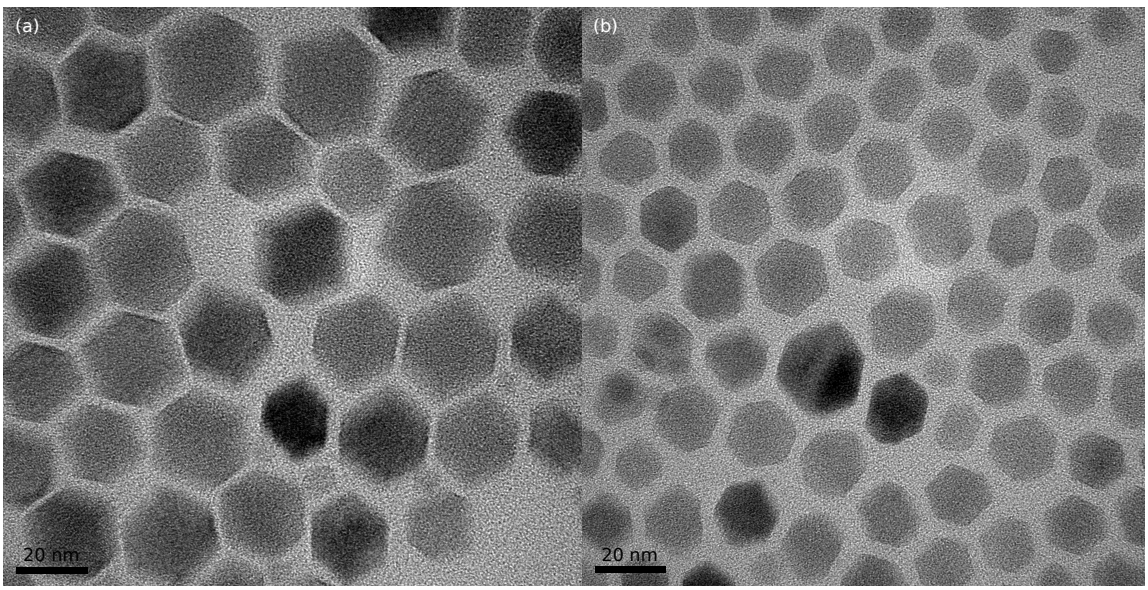

Figure 5.7. *TEM image of Er^{3+} and Yb^{3+} doped nanoparticles with a $NaYF_4$ host. (a) core-only particles and (b) core-shell particles. The shell is also made of $NaYF_4$.*

With an constant development of the particle production, our second-generation particles featured a shielding shell of undopted $NaYF_4$. It was added in order to reduce the non-radiative losses caused by surface effects. A recently reported method [213] was followed for the fabrication. Fig. 5.7 show transmission electron microscopy (TEM) images of core-only and core-shell particles. It can be seen how the particles have grown slightly in size while maintaining their shape. The controlled growth was confirmed by dynamic light scattering (DLS) presented in Fig. 5.8. The mean diameter from the DLS measurements were 17 nm and 27 nm for the core-only and core-shell particles. DLS measured the hydrodynamic diameter and can thus not be directly compared to the TEM images.

All particles employed have been characterized in terms of their intensity dependence and luminescence emission spectrum. Fig. 5.9 shows the intensity-dependent luminescence signal in a

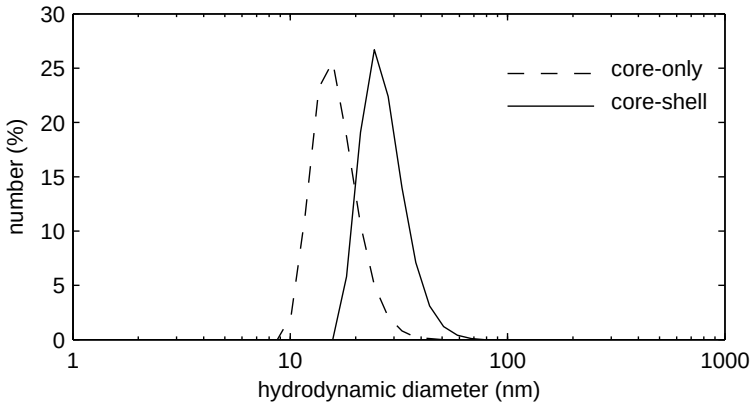

Figure 5.8. *DLS measurements of core-only and core-shell particles. It is the same particles as presented in Fig. 5.7. Mean hydrodynamic diameter of the core and the core-shell particles were 17 nm and 27 nm, respectively.*

double logarithmic plot for core-only Tm^{3+} doped nanoparticles and its emission at 800 nm. The slope of the linear regression is two, suggesting it is a two-photon process. Fig. 5.10 displays the luminescence spectrum for core-shell co-activator-doped Tm^{3+} and Er^{3+} nanoparticles. With two activators in the same crystal, three luminescence emission bands could be generated when excited at 980 nm. However, single-activator-doped crystal was found preferable for its brighter luminescence emission and higher dynamic range in terms of excitation intensity. The co-doped nanoparticles had a tendency to not have a quadratic intensity dependence over the entire excitation intensity range. It shifted from being less than two at low excitation intensities to become larger than two at higher intensities.

5.8 Summarizing and looking towards the future

Upconverting nanoparticles have potential to become a widely adapted fluorescent probe. The ability to emit anti-Stokes shifted emission even at moderate excitation intensities make them well suited for deep-tissue fluorescence imaging. Paper **II** exploited this property for demonstrating autofluorescence insensitive fluorescence imaging. Circumventing the autofluorescence may eventually push the detection-limit of exogenous fluorophores in deep-tissue fluorescence imaging, since background-free detection can be performed. Stokes shifted fluorophores are all limited by back-

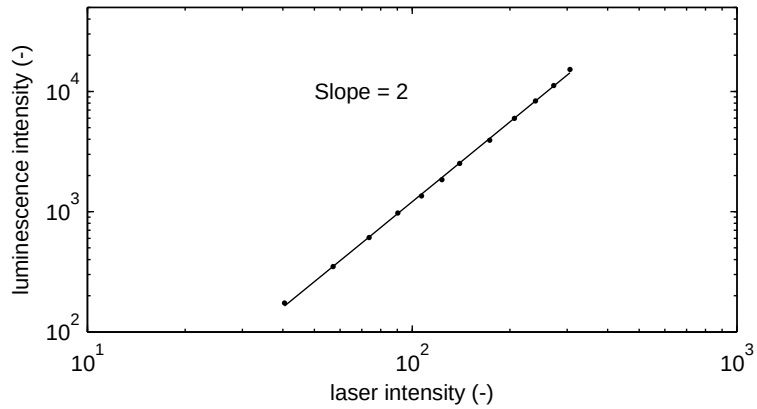

Figure 5.9. *Excitation intensity-dependent luminescence signal in a double logarithmic plot. The sample measured was core-only Tm^{3+} doped nanoparticles. The luminescence signal was filtered to only collect the 800 nm emission.*

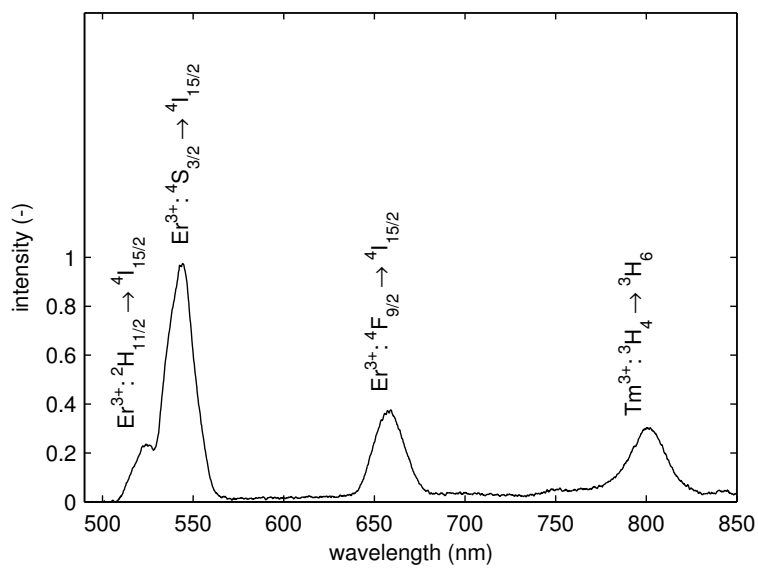

Figure 5.10. *Luminescence emission spectra generated with 980 nm excitation. Co-activator-doped Er^{3+} and Tm^{3+} core-shell nanoparticles are measured. The different emission bands are identified with corresponding activator-ion and transition. See Fig. 5.5 for the transitions involved.*

ground autofluorescence for detection. The amount of autofluorescence induced depends heavily on the excitation wavelength. In comparison to other types of fluorescent probes with quantum efficiencies > 80 %, upconverting nanoparticles have a low quantum efficiency (presently a few percent maximum), which would argue against an increased detection-limit using upconverting nanoparticles. A further comparison between Stokes and anti-Stokes shifted fluorophores for the lowest detection-limit would depend on the tissue type, excitation and emission wavelengths and quantum yield of the fluorophores. In essence, this remains an open question, where the answer probably will depend on the application.

Upconverting nanoparticles are photo-stable using moderate excitation intensities, a property which enables pro-longed interaction times and which could be a door-opener for new types of experiments. The non-photo-bleaching ability of quantum dots is usually put forward as one of their greatest properties [41], and this is a property shared by unconverting nanoparticles. In contrast to quantum dots, upconverting nanoparticles are excited at 975 nm instead of the the UV, thereby facilitating a deeper penetration of the excitation light in tissue.

Papers **III**, **IV** and **V** all present methods for improving the image quality using upconverting nanoparticles with a focus on image resolution. Improvements in image quality, especially for tomographic imaging are essential, if fluorescence imaging as a modality is going to compete with other functional imaging techniques like PET and SPECT.

Chapter 6

Transscleral optical spectroscopy

6.1 Anatomy of the eye

A simplified drawing of the eye anatomy is presented in Fig. 6.1. The posterior part of the eye, comprising the sclera, choroid and retina, has been the focus of in this work. In between the choroid and the retina is the retinal pigment epithelium (RPE) located. It is composed of a single cell layer, which is heavily pigmented and appears black or dark brown in color. The outer white layer of the

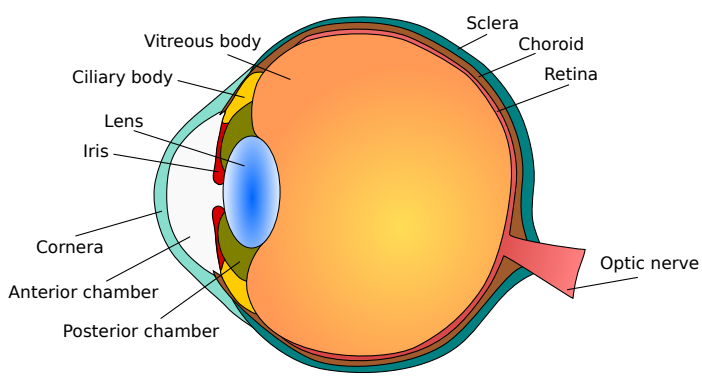

Figure 6.1. *A simplified layout of the eye. In this theses, the three tissue layers encapsulating the vitreous body have been of special interest; from the outside in, sclera, choroid and retina. In between the choroid and the retina and not drawn in the figure is the RPE. The uveal tract consising of the iris, ciliary body and choroid make up a vascular coat surrounding the vitreous body.*

Tissue	(mm^{-1}) μ_a	(mm^{-1}) μ_s'
Sclera	0.2	9
Choroid	5-20	3-8
RPE	90	19
Retina	0.1	0.8

Table 6.1. *Optical properties of the posterior tissue layers in the eye at 600nm. Numbers are from Ref. [243]*

eye is the sclera, which is rich in collagen and elastic fibers. Its thickness varies from about 1mm at the optic nerve to 0.5mm at the eye equator [241]. A healthy choroidal tissue layer has a thickness of about 0.3 to 0.2mm, again being thicker at the posterior parts of the eye [242]. Its main function is to supply nutrition to the retina. The choroid together with the ciliary body and the iris form the uveal tract.

Intraocular tumors have a tendency to grow in the posterior part of the eye in the choroidal tissue layer [45, 48]. For optical access, two pathways are plausible, either through the cornea, lens, vitreous body, retina and RPE, or from the outside only passing through the sclera to reach the choroid. We have been choosing the latter approach; accessing the choroid through the sclera from the outside of the eye.

Optical properties of the posterior part of the eye are presented in Table 6.1. So far, only a few reports on posterior eye tissue optical properties exists [243–245]. They all reported heavily scattering with low absorption for the scleral tissue layer. Hammer *et al.*[243], also investigated the choroidal tissue layer, which had a range of different optical properties strongly dependent on the hemoglobin content. Overall, a high absorption coefficient was reported in the choroidal tissue layer. The RPE presented extreme optical properties, with high absorption and scattering.

6.2 An intraocular tumor-model in porcine eyes

The initial work have been carried out on intraocular tumor models in porcine eyes to investigate the feasibility and accuracy of transscleral optical spectroscopy for quantifying both melanin (Paper **VI**) and hemoglobin (Paper **VII**). The same tumor model was also employed in Paper **VIII**.

Fig. 6.2 displays images of the tumor model. Fresh porcine eyes no older than 5 days post-mortem hosted the tumor-model. Porcine skin gelatin, titanium dioxide and natural melanin or human blood made a mixture simulating either a uveal melanoma or a hemoglobin rich, vascularized choroidal tumor. The mixture was gently injected into the suprachoroidal space where it was left to complete the gelation. The combination of titanium dioxide and gelatin is a standard recipe to simulate optical properties of tissue [246]. The addition of whole blood provided a realistic absorption spectra. Natural melanin, isolated from the ink sac of cuttlefish (Sepia officinalis), was used because it resembles the melanin found in the human body [71]. One limitation of the tumor-model is that real tumors will not present themselves equally homogenous as the tumor phantoms.

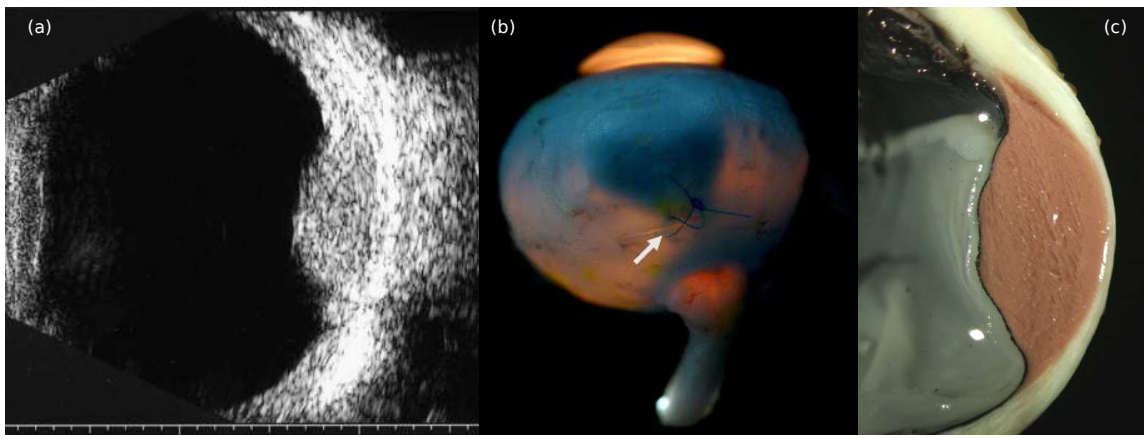

Figure 6.2. *Images of the intraocular tumor-model in porcine eyes. (a) Ultrasonography image showing the tumor-model protruding into the vitreous body. (b) Transillumination image displaying the shadow casted on the sclera by the tumor-model. Light was injected through the pupil. (c) Color photograph of the tumor-model. Note that it is a different eye in all three images.*

6.3 Instrument development

A series of three different instruments have been used for transscleral optical spectroscopy. In the beginning, in Paper **VI**, a Xe lamp was used as the light source, which produced a bright wide spectrum with very sharp spectral features, see Fig. 6.3. The peaks limited the dynamic range of the measurement. Also, the particular lamp and power supply employed caused quite large intensity fluctuations, not making it an ideal choice for diffuse reflectance measurements.

The second generation setup improved on the light source. The Xe lamp was replaced with a tungsten halogen lamp, producing a much smoother spectrum as dispayed in Fig. 6.4. This setup was used in Paper **VII** and allowed for higher dynamic range measurements. Unfortunately, the source itself contain a filter blocking the wavelengths beyond 950nm. The limited spectral range made it unsuitable for measuring water content in tissue, which has its main absorption profile within the tissue optical window at 980nm. With the aim of Paper **VII** to quantify hemoglobin content, this was not a major concern, but rather a capability desired.

In the third generation instrument, both source and detector were exchanged. Still a tungsten halogen lamp was employed, but in a version that extended the spectrum far into the near infrared region, see Fig. 6.5. With this source, the spectral range was further limited by the sensitivity of the detector, and not the source itself. In conjunction with a stable power supply, it produced a stable intensity spectrum, very much suited for diffuse reflection

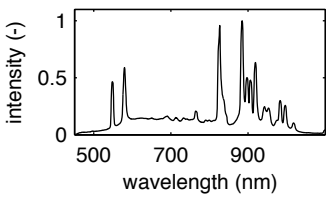

Figure 6.3. *Reference spectrum measured with the first generation instrument. A Xe lamp was used in conjunction with an imaging spectrometer. The peaks are all characteristic to Xe.*

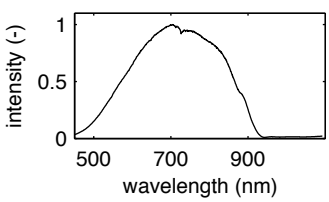

Figure 6.4. *Reference spectrum measured with the second generation instrument. A tungsten halogen lamp was used together with an imaging spectrometer. A filter within the lamp cut the spectrum at longer wavelengths.*

spectroscopy. A new detector, which was correctly calibrated, increased the spectral precession substantially. This setup was used in Papers **VIII** and **IX**.

6.4 Probe development

The geometry is an important factor to consider for intensity measurements. A change of the diffuse intensity by 10% typically corresponds to a geometrical difference of 0.5mm (assuming an infinite homogeneous tissue with a $\mu_{\text{eff}} = 2\text{cm}^{-1}$). Keeping a standardized geometry is therefore a key for being able to compare measurements.

Two different probes have been used, depicted in Fig. 6.6. The first one, used in Papers **VI** and **VII**, had the simplest imaginable design. It was made of two optical fibers spaced 6mm apart (center-to-center distance). One fiber delivered and one fiber collected the light. With such a small probe-tissue contact, only the cross-section area of the two fibers, a high pressure on the tissue could easily be applied, leading to a deformed curvature of the scleral surface. In an attempt to standardize this procedure, the pressure applied was monitored and kept constant. Still the curvature deformation of the sclera made a complex geometry.

In the second generation probe, which was the focus of Paper **VIII**, a suitable version for being handheld during for *in vivo* measurements was developed. It featured a cylinder shaped probe with two slightly protruding fibers. With this design, the pressure exerted by the probe formed an even and smooth surface of the sclera. By noticing when the probe made an aplanatic contact with the sclera, the pressure could be standardized. The main motivation for designing a handheld probe have been to find a suitable instrument for *in vivo* characterization of intraocular tumors.

The most important parameter in the design of both probes has been the source-detector distance, which strongly influenced the probe volume. An optimization for sensitivity to the choroidal tissue layer has always been strived for. Initially, an estimation of the optimal source-detector distance was made using a cylindrical symmetrical layered tissue-model with optical properties from the literature [243]. A distance of 6mm was found optimum and this was used in Papers **VI** and **VII**. Thereafter, an experimental verification was made in Paper **VIII**, which found a slightly shorter distance of 5mm to be preferable.

6.5 Evaluating diffuse reflectance spectra

There are several ways of interpreting and analyzing the measured spectra. Since the measured attenuation is a combination of scatter and absorption a pure absorption spectrum is not obtained

directly. With the type of steady-state measurement performed, a separation of the two quantities is neither feasible. Thereby, direct access to the absorption spectrum is not permissible, which would have been the favorable, and other ways of interpreting the spectra must be made. Two chromophores have been of particular interest, hemoglobin and melanin, and they are discussed in detail below.

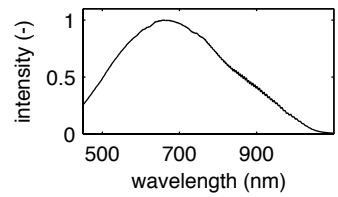

Figure 6.5. *Reference spectrum measured with the third generation instrument. A halogen lamp was used together with a fiber-based miniaturized spectrometer. Notice that the sensitivity at longer wavelength has increased substantially to the previous setup.*

6.5.1 Melanin spectroscopy

The current knowledge about melanin is actually somewhat limited for being such an important chromophore. Neither the chemical composition and its structure, nor the absorption or extinction coefficients are precisely known. Melanins is usually divided into three categories; allomelanin found in the plant kingdom, eumelanin and pheomelanin found in humans. Eumelanin consists of dark brown and black pigments, while pheomelanin has a yellow and red-brown color [71]. Eumelanin is the more common form, and exists, for example, in the RPE of human eyes. Its natural shape is as a particle. Typically, it presents itself either as single particles ($\sim$ 30nm), or as larger aggregates [71]. The particle nature of eumelanin makes it difficult to distinguish its absorption and scattering properties.

The extinction spectrum for eumelanin can relatively easily be measured [247]. It has the shape of an exponentially decaying function without any distinct spectral features, see Fig. 6.7. The smooth spectrum makes it cumbersome to identify melanin. Also more quantitative measurements of eumelanin have been made. The absorption coefficient of melanosomes in the epidermis (μ_a = 296cm^{-1} at 694nm) and retinal pigmented epithelium (μ_a = 2370cm^{-1} at 532nm) have been measured using explosive vaporization [248, 249].

A range of experiments based on diffuse reflectance spectroscopy have been conducted to quantify melanin concentration in skin. Early attempts include the work by Kollias *et al.*[70, 250], who estimated the melanin content by fitting an exponential function to the ratio of two measurements, one on the dorsal part of the forearm and one on the ventral side. Model-based approaches, where the spectrum is fitted to a diffusion or an empirical model, have also been reported [251, 252]. The most extensive material is presented by Marchesini *et al.*[253], who has investigated more than 1500 patients with different stages of melanoma. They analyzed the spectra in a similar way to Kollias *et al.*by calculating the slope to the function $\log(R_s/R_l)$, where R_l is the diffuse reflectance from the lesion and R_s from a near-by site. By performing this analysis, they assumed an exponential extinction of melanin.

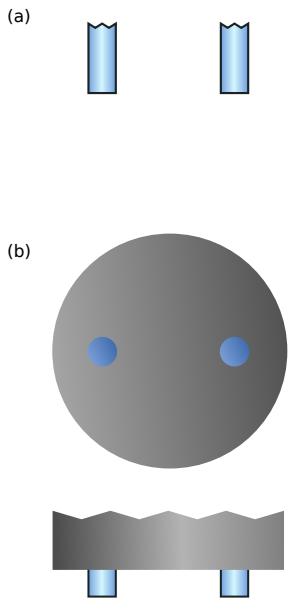

Figure 6.6. *(a) First generation probe with two bare fibers. (b) Second generation probe with two slightly protruding fibers from a cylinder shaped housing.*

6.5.2 Hemoglobin spectroscopy

Hemoglobin is an iron-containing and oxygen-carrying protein, which makes up about 35% of the human red blood cells mass. Both oxyhemoglobin and deoxyhemoglobin have distinct absorption spectra within the tissue optical window, see Fig. 6.8. This makes it the most accessible chromophore to measure, as it easily can be identified and the oxygen saturation can be deduced. For an extensive introduction to hemoglobin spectroscopy, the reader is referred to Ref [67].

The absorption coefficient for both oxyhemoglobin and deoxyhemoglobin are well characterized. Its less common states and forms, methemoglobin and myoglobin are also well documated. Small differences in the absorption coefficient for hemoglobin between mammals have also been studied [67].

During the last years, a great interest in the measurement of hemoglobin by near-infrared spectroscopy (NIRS) has been reported [254–257]. The first *in vivo* NIRS measurement was made over 30 years ago by Frans Jöbsis [258]. He reported tissue blood flow changes and saturation measurement in the brain and the heart. Since then, NIRS has been applied to evaluate brain function [259], breast cancer diagnosis [6], and others. Typically a model-based evaluation is adopted to evaluate the NIRS signals.

6.5.3 Evaluation with partial least squares analysis

In the present studies, a model-based evaluation was not performed. Instead we asked the question if it is possible to distinguish between different types of lesions by measuring its diffuse reflection in the NIR. To do so, we employed partial least squares regression. It is an evaluation method, which has a strong resemblance to principle component analysis, in the way that the data and the predicted values are transformed into a new space. This new space is of a lower dimensionality, where the basis are formed from combinations of the spectral channels. Choosing the basis and the dimensionality is a key for successful differentiation between the variables.

When performing this type of evaluation, a training set needs to be feed to the algorithm. This training set contains the spectrum for each type of lesion that should be classified. In this way, the algorithm is taught to recognize the different lesion types. After successful teaching, the algorithm can classify an unknown sample and tell its contains.

This is a very powerful method as it can transform the data to a space where the differences between the variables are more visible. There are obvious drawbacks as well. Any unknown measurement outside the parameter set used for training cannot be classified correctly. In addition, the algorithm cannot differentiate between

differences imposed by the lesion or for instance a change made to the instrument. It means that exactly the same measurement condition must be maintained for use of this type of evaluation.

6.6 Future directions

6.6.1 Model-based evaluation

To make a model-based evaluation of the spectra would be one step forward. Then the optical properties of the tissue could be extracted. With the optical properties determined, the concentration of the tissue chromophores could be retrieved. This type of analysis would thus give a quantitative measure of the tissue constituents. One possible way to proceed would be to make a semi-infinite model of the eye. An semi-infinite geometry is far from the true geometry of the eyes investigated, but from a computational viewpoint it is a convenient first approximation. Different tissue chromophores as hemoglobin, water and melanin could be included to simulate the absorption coefficient. An appropriate scattering level could be found in the literature and its spectral shape could be assumed by a combination of Mie and Raylight scattering. This could perhaps be realized, but would still be challenging as the measurements are influenced by a mixture of attenuation from both absorption and scattering. Also, a semi-infinite model might prove to be a too simplistic, and a more realistic geometry is probably needed.

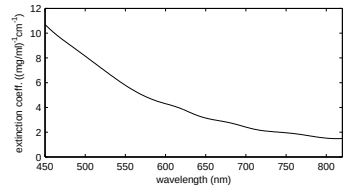

Figure 6.7. *Extinction spectrum for melanin in the NIR region. Note the lack of features. Data from Ref: [69]*

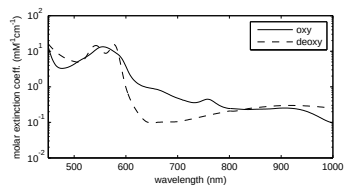

Figure 6.8. *Molar extinction spectrum for oxy- and deoxyhemoglobin in the NIR region. Values taken from Ref: [67]*

6.6.2 Alternative measurement geometries

The goal of the measurement geometry is to maximize the signal from the lesion. This have, as described earlier, been implemented by optimizing the source-detector distance to become sensitive to the choroidal tissue layer. Alternative measurement geometries to consider would be transillumination and in-contact-choroidal measurements with a single fiber.

A transillumination geometry could be accomplished by illuminating through the pupil and detecting the transmitted light on the sclera, much like the image shown in Fig. 6.2 (b). Since eye tissue is very forward scattering [243], with g values above 0.9, a transillumination geometry could be beneficial to increase the sensitivity to the choroidal tissue layer. Still the light needs to propagate through the retina, RPE and sclera in addition to the choroid, which is not ideal.

A single fiber in-contact-choroidal measurement would be another alternative. By gently pushing the fiber-tip directly on the scleral surface, it can locally displace the tissue fluid, making the sclera effectively transparent. This is a reversible processes and

can be made without harming the scleral tissue. Placing an optical probe, which transmit and receive light through the same fiber, onto the sclera and applying a gentle pressure would put the optical fiber in very close contact with the choroidal tissue layer. Since the choroidal tumors are relatively large (millimeters in diameter and height), most of the sampled signal would originate from the tumor tissue. This is of course attractive.

6.6.3 In vivo characterization of intraocular tumors

The finding in Paper **VIII** indicated that our method of transscleral spectroscopy is a safe procedure that does not cause damage to the eye. In future work, we intend to apply this probe for *in vivo* characterization of various types of intraocular tumors. Transscleral *in vivo* spectroscopy is probably most suitable for choroidal tumors located at or anterior to the equator. In order to probe more posteriorly situated lesions, a minimal invasive procedure in form of a small conjunctival incision may be needed to allow free access to the sclera. And as demonstrated by Papers **VI** and **VII**, hemoglobin quantification is more specific then that of melanin.

Comments on the papers

I **A matrix-free algorithm for multiple wavelength fluorescence tomography**
A.D. Zacharopoulos, P. Svenmarker, J. Axelsson, M. Schweiger, S.R. Arridge and S. Andersson-Engels.
Optics Express **17**, 3025-3035 (2009).

This paper reported on a new method to solve the inverse fluorescence diffuse optical tomography problem. It was especially adapted for CCD-based detection as the cost of the inverse calculation could be made invariant to the number of detector used. Further, it presented a method of for multispectral fluorescence diffuse optical tomography. Experimental investigations in tissue phantoms verified the proposed method.

I designed the experiment, performed the experimental work, assisted in implementing the new code and wrote minor parts of the manuscript.

II **Autofluorescence insensitive imaging using upconverting nanocrystals in scattering media**
C.T. Xu, N. Svensson, J. Axelsson, P. Svenmarker, G. Somesfalean, G. Chen, H. Liang, H. Liu, Z. Zhang and S. Andersson-Engels.
Applied Physics Letters **93**, 171103 (2008).

This letter was the first correspondence from our group on upconverting nanoparticles. It showed how anti-Stokes shifted fluorescence emission from upconverting nanoparticles could be used to perform autofluorescence insensitive imaging in scattering media. Experiments were performed in tissue phantoms using $NaYF_4 : Yb^{3+}, Tm^{3+}$ particles and compared to a fluorescent dye.

I prepared the diffuse imaging experimental setup and was involved in the discussion regarding the data evaluation.

III **Use of nonlinear upconverting nanoparticles provides increased spatial resolution in fluorescence diffuse imaging**
P. Svenmarker, C.T. Xu and S. Andersson-Engels.
Optics Letters **35**, 2789-2791 (2010).

This letter reported on how upconverting nanoparticles could be used to increase the resolution in fluorescence diffuse imaging. Experiments were performed in tissue phantoms using $NaYF_4 : Yb^{3+}, Tm^{3+}$ particles and compared to a fluorescent dye.

I designed the experiment, performed the diffuse tissue imaging, did the data analysis and wrote the manuscript.

IV **High-Resolution Fluorescence Diffuse Optical Tomography Developed with Nonlinear Upconverting Nanoparticles**
C.T. Xu, P. Svenmarker, H. Liu, X. Wu, M.E. Messing
L.R Wallenberg and S. Andersson-Engels.
Submitted for publication in ACS Nano.

This article is an continuation of Paper **III**, were the resolution of fluorescence diffuse optical tomography using upconverting nanoparticles was investigated in tissue phantoms. In addition, characterizations of the in-house developed $NaYF_4 : Yb^{3+}, Tm^{3+}$ particles used were presented.

I designed the experiment, performed the diffuse tissue imaging and was involved in the discussion regarding the data evaluation.

V **Multispectral guided fluorescence diffuse optical tomography using upconverting nanoparticles**
P. Svenmarker, C.T. Xu, H. Liu, X. Wu and
S. Andersson-Engels.
Manuscipt in preparation.

This manuscript presented how to make use of the large anti-Stokes shifted fluorescence emission from $NaYF_4 : Yb^{3+}, Er^{3+}$ nanoparticles to guide the tomographic inversion. Experiments were performed in tissue phantoms.

I designed the experiment, performed the diffuse tissue imaging, did the data analysis and wrote the manuscript.

VI **Transscleral visible/near-infrared spectroscopy for quantitative assessment of melanin in a uveal melanoma phantom of ex vivo porcine eyes**
J. Krohn, C.T. Xu, P. Svenmarker, D. Khoptyar and S. Andersson-Engels.
Experimental Eye Research **90**, 330-336 (2010).

This article was the first report on transscleral diffuse optical spectroscopy. It presented the use of diffuse reflectance spectroscopy through the sclera of porcine eyes to quantify melanin content in the choroid.

I performed the spectroscopy, participated in the discussions regarding the data evaluation and wrote minor parts of the manuscript.

VII **Transscleral visible/near-infrared spectroscopy for quantitative assessment of haemoglobin in experimental choroidal tumours**
C.T. Xu, P. Svenmarker, S. Andersson-Engels and J. Krohn.
DOI: 10.1111/j.1755-3768.2010.02037.x (2010) *Acta Ophthalmologica*.

This article is an continuities of Paper **VI**. Here the hemoglobin content in the choroid was quantified using transcleral diffuse optical spectroscopy.

I performed the spectroscopy and participated in the discussions regarding the data evaluation.

VIII **Effects of probe geometry on transscleral diffuse optical spectroscopy**
P. Svenmarker, C.T. Xu, S. Andersson-Engels and J. Krohn.
Biomedical Optics Express **2**, 3058-3071 (2011).

This paper reported on the development of a probe suitable for *in vivo* transcleral diffuse optical spectroscopy. The geometry and the safety were to two main parameters evaluated.

I performed the spectroscopy, made the data evaluation and wrote major parts of the manuscript.

IX **Transscleral optical spectroscopy of uveal melanoma in enucleated human eyes**
J. Krohn, P. Svenmarker, C.T. Xu, S.J. Mörk and S. Andersson-Engels.
Submitted for publication in Investigative Ophthalmology & Visual Science.

This manuscript reported the initial experiences of diffuse optical spectroscopy measured through the sclera of enucleated human eyes to characterize uveal melanomas. In total 9 patients were included. Clear indications of sensitivity to melanin in the melanomas were found.

I performed the data analysis and wrote minor parts of the manuscript.

X **Drug quantification in turbid media by fluorescence imaging combined with light-absorption correction using white Monte Carlo simulations**
H. Xie, H. Liu, P. Svenmarker, J. Axelsson, C.T. Xu, S. Gräfe, J.H. Lundeman, H.P.H. Cheng, S. Svanberg, Sune N. Bendsoe, P.E. Andersen, K. Svanberg, S. Andersson-Engels.
Journal of Biomedical Optics **16**, 066002 (2011).

This paper reported a method for correction of the fluorescence emission intensity due to different tissue optical properties. By using a look-up-table of optical properties for different tissue types, the emitted fluorescence intensity can be compensated for different absorption and scattering found in different tissue types.

I participated in designing the experiment, build the experimental setup and participated in the diffuse tissue imaging.

Acknowledgements

First of all, I am truly thankful to my supervisor Stefan Andersson-Engels for guiding me through my Ph.D. studies. Your positive attitude and your courage to pursue new research topics are sincerely inspirational. At the same time, I deeply appreciate the opportunities given to me to interact with fellow scientist across the globe and for the freedom received to pursue my own ideas. I will always be grateful for your support.

My strong admiration also goes to my co-supervisors: Katarina Svanberg for your enthusiasm and for being an excellent host during measurement campaigns and conferences. And Sune Svanberg for your never-ending energy and for sharing your passion for science. Warmest of thanks also to Peter Andersen for organizing the wonderful summer school at Hven.

In pursuit of this thesis, I have been fortunate to collaborate with experts from different scientific fields, to whom I am all thankful. In particular, I would like to mention: Jørgen Krohn for making the choice to travel to Lund and present your ideas on spectroscopy for ophthalmology, and for cod fishing in the North Sea. Niels Bendsoe for support during measurement campaigns, especially while visiting the Department of Dermatology in Lund. Prof. Zhang and his group at Harbin Institute of Technology for fabricating the first upconverting nanoparticles we used. Gabriel Somesfalean for eminent connections to Harbin Institute of Technology. Simon Arridge, Martin Schweiger and Athanasios Zacharopoulos for interesting and fruitful collaborative work. Ilya Turchin for hosting me in Nizhny Novgorod.

I moreover owe sincere and earnest thankfulness to my colleagues and friends in the Biophotonics group: Erik Alerstam for sharing delicious food and for having interesting discussions. Johan Axelsson for being an excellent traveling companion and introducing me to diffuse optics. Can Xu for outstanding collaborations and for being a linux-guru. Haiyan Xie, Haichun Liu, Tomas Svensson, Emilie Krite Svanberg, Dmitry Khoptyar, and Arman Ahamed - past and present members of the group, thank you all for your friendship and exciting work.

I also wish to thank colleagues at the Atomic Physics Division, both former and present members, for providing a friendly and stimulating environment. In particular, Mikkel Brydegaard Sørensen for playing drums together, Marcus Dahlström for showing me his hometown, Miguel Miranda for being a good friend and Ralf Nüske for helping me with Linux. Teaching together with Nina Reistad has been inspiring and rewarding - thank you.

A successful completion of this thesis would not have been possible without the support and encouragement from my friends. Thank you for reminding me about the importances in life.

And finally, I deeply appreciate the unconditional support and encouragement received from my beloved family.

References

1. Colin Mathers, Ties Boerma and Doris Ma Fat. The global burden of disease 2004 update. World Health Organization (2008).

2. Peter Boyle and Bernard Levin. World Cancer report 2008. International Agency for Research on Cancer (2008).

3. LH Sobin, MK Gospodarowicz and C Wittekind. *TNM Classification of Malignant Tumours*. Wiley-Blackwell 7th ed edition (2009).

4. R. Etzioni, N. Urban, S. Ramsey, M. McIntosh, S. Schwartz, B. Reid, J. Radich, G. Anderson and L. Hartwell. *The case for early detection*. Nature Reviews Cancer **3**, 243–252 (2003).

5. R. Weissleder. *Semiconductor nanocrystals as fluorescent biological labels*. Science **312**, 1168–1171 (2006).

6. B. J. Tromberg, N. Shah, R. Lanning, A. Cerussi, J. Espinoza, T. Pham, L. Svaasand and J. Butler. *Non-invasive in vivo characterization of breast tumors using photon migration spectroscopy*. Neoplasia **2**, 26–40 (2000).

7. R. Weissleder and M. J. Pittet. *Imaging in the era of molecular oncology*. Nature **452**, 580–589 (2008).

8. R. Weissleder and U. Mahmood. *Molecular imaging*. Radiology **219**, 316–333 (2001).

9. T. F. Massoud and S. S. Gambhir. *Molecular imaging in living subjects: seeing fundamental biological processes in a new light*. Genes & Development **17**, 545–580 (2003).

10. M. E. Juweid and B. D. Cheson. *Current concepts - Positron-emission tomography and assessment of cancer therapy*. New England Journal of Medicine **354**, 496–507 (2006).

11. M. G. Harisinghani, J. Barentsz, P. F. Hahn, W. M. Deserno, S. Tabatabaei, C. H. van de Kaa, J. de la Rosette and R. Weissleder. *Non-invasive detection of clinically occult lymph-node metastases in prostate cancer*. New England Journal of Medicine **348**, 2491–U5 (2003).

12. J. S. Wyatt, D. T. Delpy, M. Cope, S. Wray and E. O. R. Reynolds. *Quantification of Cerebral Oxygenation and Hemodynamics In Sick Newborn-infants By Near-infrared Spectrophotometry*. Lancet **2**, 1063–1066 (1986).

13. V. Ntziachristos and B. Chance. *Probing physiology and molecular function using optical imaging: applications to breast cancer*. Breast Cancer Research **3**, 41–46 (2001).

14. V. Ntziachristos, A. G. Yodh, M. Schnall and B. Chance. *Concurrent MRI and diffuse optical tomography of breast after indocyanine green enhancement.* Proceedings of the National Academy of Sciences of the United States of America **97**, 2767–2772 (2000).

15. D. J. Hawrysz and E. M. Sevick-Muraca. *Developments toward diagnostic breast cancer imaging using near-infrared optical measurements and fluorescent contrast agents.* Neoplasia **2**, 388–417 (2000).

16. L. Spinelli, A. Torricelli, A. Pifferi, P. Taroni, G. Danesini and R. Cubeddu. *Characterization of female breast lesions from multi-wavelength time-resolved optical mammography.* Physics In Medicine and Biology **50**, 2489–2502 (2005).

17. Ralph Weissleder and Vasilis Ntziachristos. *Shedding light onto live molecular targets.* Nature Medicine **9**, 123–128 (2003).

18. V Ntziachristos, J Ripoll, LHV Wang and R Weissleder. *Looking and listening to light: the evolution of whole-body photonic imaging.* Nature Biotechnology **23**, 313–320 (2005).

19. R. Weissleder, C. H. Tung, U. Mahmood and A. Bogdanov. *In vivo imaging of tumors with protease-activated near-infrared fluorescent probes.* Nature Biotechnology **17**, 375–378 (1999).

20. R. M. Hoffman. *The multiple uses of fluorescent proteins to visualize cancer in vivo.* Nature Reviews Cancer **5**, 796–806 (2005).

21. A. Petrovsky, E. Schellenberger, L. Josephson, R. Weissleder and A. Bogdanov. *Near-infrared fluorescent imaging of tumor apoptosis.* Cancer Research **63**, 1936–1942 (2003).

22. V. Ntziachristos, E. A. Schellenberger, J. Ripoll, D. Yessayan, E. Graves, A. Bogdanov, L. Josephson and R. Weissleder. *Visualization of antitumor treatment by means of fluorescence molecular tomography with an annexin V-Cy5.5 conjugate.* Proceedings of the National Academy of Sciences of the United States of America **101**, 12294–12299 (2004).

23. S. R. Cherry. *Multimodality in vivo imaging systems: Twice the power or double the trouble?* Annual Review of Biomedical Engineering **8**, 35–62 (2006).

24. D. W. Townsend and S. R. Cherry. *Combining anatomy and function: the path to true image fusion.* European Radiology **11**, 1968–1974 (2001).

25. M. S. Judenhofer, H. F. Wehrl, D. F. Newport, C. Catana, S. B. Siegel, M. Becker, A. Thielscher, M. Kneilling, M. P. Lichy, M. Eichner, K. Klingel, G. Reischl, S. Widmaier, M. Rocken, R. E. Nutt, H. J. Machulla, K. Uludag, S. R. Cherry, C. D. Claussen and B. J. Pichler. *Simultaneous PET-MRI: a new approach for functional and morphological imaging.* Nature Medicine **14**, 459–465 (2008).

26. D. Hyde, R. de Kleine, S. A. MacLaurin, E. Miller, D. H. Brooks, T. Krucker and V. Ntziachristos. *Hybrid FMT-CT imaging of amyloid-beta plaques in a murine Alzheimer's disease model.* Neuroimage **44**, 1304–1311 (2009).

27. Yuting Lin, William C. Barber, Jan S. Iwanczyk, Werner W. Roeck, Orhan Nalcioglu and Gultekin Gulsen. *Quantitative fluorescence tomography using a trimodality system: in vivo validation.* Journal of Biomedical Optics **15** (2010).

28. S. C. Davis, B. W. Pogue, R. Springett, C. Leussler, P. Mazurkewitz, S. B. Tuttle, S. L. Gibbs-Strauss, S. S. Jiang, H. Dehghani and K. D. Paulsen. *Magnetic resonance-coupled fluorescence tomography scanner for molecular imaging of tissue.* Review of Scientific Instruments **79**, 064302 (2008).

29. S. W. Hell. *Far-field optical nanoscopy.* Science **316**, 1153–1158 (2007).

30. J. Sharpe, U. Ahlgren, P. Perry, B. Hill, A. Ross, J. Hecksher-Sorensen, R. Baldock and D. Davidson. *Optical projection tomography as a tool for 3D microscopy and gene expression studies.* Science **296**, 541–545 (2002).

31. W. DENK, J. H. STRICKLER and W. W. WEBB. *2-photon Laser Scanning Fluorescence Microscopy Rid B-5905-2011.* Science **248**, 73–76 (1990).

32. Vasilis Ntziachristos. *Fluorescence Molecular Imaging.* Annual Review of Biomedical Engineering **8**, 1–33 (2006).

33. M. Chalfie, Y. Tu, G. Euskirchen, W. W. Ward and D. C. Prasher. *Green Fluorescent Protein As A Marker For Gene-expression.* Science **263**, 802–805 (1994).

34. B. N. G. Giepmans, S. R. Adams, M. H. Ellisman and R. Y. Tsien. *Review - The fluorescent toolbox for assessing protein location and function.* Science **312**, 217–224 (2006).

35. G. Grynkiewicz, M. Poenie and R. Y. Tsien. *A New Generation of Ca-2+ Indicators With Greatly Improved Fluorescence Properties.* Journal of Biological Chemistry **260**, 3440–3450 (1985).

36. W. Stummer, U. Pichlmeier, T. Meinel, O. D. Wiestler, F. Zanella and R. Hans-Jurgen. *Fluorescence-guided surgery with 5-aminolevulinic acid for resection of malignant glioma: a randomised controlled multicentre phase III trial.* Lancet Oncology **7**, 392–401 (2006).

37. F Auzel. *Upconversion and anti-stokes processes with f and d ions in solids.* Chemical Reviews **104**, 139–173 (2004). upconversion.

38. S Andersson-Engels and B C Wilson. *In vivo fluorescence in clinical oncology: fundamental and practical issues.* Journal of Cellular Pharmacology **3**, 66–79 (1992).

39. S. Prahl. Optical Absorption of Indocyanine Green (ICG) (2012). URL http://omlc.ogi.edu/spectra/icg/index.html.

40. Dyomics. Absorption and emission of DY-781 (2012). URL http://www.dyomics.com/dy-781.html.

41. X. Michalet, F. F. Pinaud, L. A. Bentolila, J. M. Tsay, S. Doose, J. J. Li, G. Sundaresan, A. M. Wu, S. S. Gambhir and S. Weiss. *Quantum dots for live cells, in vivo imaging, and diagnostics.* Science **307**, 538–544 (2005).

42. S Heer, K Kompe, HU Gudel and M Haase. *Highly efficient multicolour upconversion emission in transparent colloids of lanthanide-doped NaYF4 nanocrystals.* Advanced Materials **16**, 2102+ (2004).

43. RH Page, KI Schaffers, PA Waide, JB Tassano, SA Payne, WF Krupke and WK Bischel. *Upconversion-pumped luminescence efficiency of rare-earth-doped hosts sensitized with trivalent ytterbium.* Journal of The Optical Society of America B - Optical Physics **15**, 996–1008 (1998).

44. G. Engholm, J. Ferlay, N. Christensen, F. Bray, M. L. Gjerstorff, A. Klint, J. E. Kotlum, E. Olafsdottir, E. Pukkala and H. H. Storm. *NORDCAN - a Nordic tool for cancer information, planning, quality control and research.* Acta Oncologica **49**, 725–736 (2010).

45. Jerry A. Shields, Arman Mashayekhi, R. A. Seong and Carol l. Shields. *Pseudomelanomas of the posterior uveal tract - The 2006 Taylor R. Smith Lecture.* Retina **25**, 767–771 (2005).

46. IG Rennie. *Things that go bump in the light. The differential diagnosis of posterior uveal melanomas.* Eye **16**, 325–346 (2002).

47. Andrew P. Ferry. *Lesions Mistaken for Malignant Melanoma of the Posterior Uvea: A Clinicopathologic Analysis of 100 Cases With Ophthalmoscopically Visible Lesions.* Arch Ophthalmol **72**, 463–469 (1964).

48. Jerry A. Shields and P. Robb McDonald. *Improvements in the Diagnosis of Posterior Uveal Melanomas.* Arch Ophthalmol **91**, 259–264 (1974).

49. Ocular Melanoma Study Group Collaborative. *Accuracy of diagnosis of choroidal melanomas in the Collaborative Ocular Melanoma Study.* Arch Ophthalmol **108**, 1268–1273 (1990).

50. B. Sobottka, T. Schlote, H.G. Krumpaszky and I. Kreissig. *Choroidal metastases and choroidal melanomas: comparison of ultrasonographic findings.* Br. J. Ophthalmology **82**, 159–161 (1998).

51. J. A. Shields, C. L. Shields and L. A. Donoso. *Management of Posterior Uveal Melanoma.* Survey of Ophthalmology **36**, 161–195 (1991).

52. J. D. Ferris, P. A. Bloom, P. R. Goddard and C. Collins. *Quantification of Melanin and Iron Content In Uveal Malignant Melanomas and Correlation With Magnetic-resonance Image.* British Journal of Ophthalmology **77**, 297–301 (1993).

53. A. J. Lemke, N. Hosten, T. Wiegel, R. D. Prinz, M. Richter, N. E. Bechrakis, P. I. Foerster and R. Felix. *Intraocular metastases: differential diagnosis from uveal melanomas with high resolution MRI using a surface coil.* European Radiology **11**, 2593–2601 (2001).

54. J. J. Augsburger, R. G. Peyster, A. M. Markoe, E. G. Guillet, J. A. Shields and M. E. Haskin. *Computed-tomography of Posterior Uveal Melanomas.* Archives of Ophthalmology **105**, 1512–1516 (1987).

55. G.A. Peyman and M.F. Mafee. *Uveal melanoma and similar lesions: the role of magnetic resonance imaging and computed tomography.* Radiol. Clin. North Am **25**, 471–486 (1987).

56. A. D. Singh, P. Bhatnagar and B. Bybel. *Visualization of primary uveal melanoma with PET/CT scan.* Eye **20**, 938–940 (2006).

57. R. Richards-Kortum and E. Sevick-Muraca. *Quantitative optical spectroscopy for tissue diagnosis.* Annual Review of Physical Chemistry **47**, 555–606 (1996).

58. J.W.S. Rayleigh. *On the light from the sky, its polarization and colour.* Phil. Mag. **41**, 107–120, 274–279 (1871).

59. J.W.S Rayleigh. *On the scattering of light by small particles.* Phil. Mag. **41**, 447–454 (1871).

60. G. Mie. *Articles on the optical characteristics of turbid tubes, especially colloidal metal solutions.* Annalen Der Physik **25**, 377–445 (1908).

61. Scott Prahl. Mie Scattering Calculator (2012). URL http://omlc.ogi.edu/calc/mie_calc.html.

62. A. M. K. Nilsson, C. Sturesson, D. L. Liu and S. Andersson-Engels. *Changes in spectral shape of tissue optical properties in conjunction with laser-induced thermotherapy.* Applied Optics **37**, 1256–1267 (1998).

63. J. R. Mourant, T. Fuselier, J. Boyer, T. M. Johnson and I. J. Bigio. *Predictions and measurements of scattering and absorption over broad wavelength ranges in tissue phantoms.* Applied Optics **36**, 949–957 (1997).

64. X. Wang, B. W. Pogue, S. D. Jiang, X. M. Song, K. D. Paulsen, C. Kogel, S. P. Poplack and W. A. Wells. *Approximation of Mie scattering parameters in near-infrared tomography of normal breast tissue in vivo.* Journal of Biomedical Optics **10**, 051704 (2005).

65. I. S. Saidi, S. L. Jacques and F. K. Tittel. *Mie and Rayleigh Modeling of Visible-light Scattering In Neonatal Skin.* Applied Optics **34**, 7410–7418 (1995).

66. L. G. Henyey and J. L. Greenstein. *Diffuse radiation in the galaxy.* Astrophysical Journal **93**, 70–83 (1941).

67. G. Zijlstra, Willem, Anneke Buursma and Onno W. van Assendelft. *Visible and Near Infrared Absorption Spectra of Human and Animal Haemoglobin - determination and application.* VSP (2000).

68. George M. Hale and Marvin R. Querry. *Optical Constants of Water in the 200-nm to 200-µm Wavelength Region.* Applied Optics **12**, 555–563 (1973).

69. S.L. Jacques. Optical absorption of melanins (2012). URL http://omlc.ogi.edu/spectra/melanin/index.html.

70. N. Kollias and A. Baqer. *On the Assessment of Melanin In Human-skin Invivo.* Photochemistry and Photobiology **43**, 49–54 (1986).

71. N. Kollias, R. M. Sayre, L. Zeise and M. R. Chedekel. *Photoprotection By Melanin.* Journal of Photochemistry and Photobiology B - Biology **9**, 135–160 (1991).

72. H. Fedorow, F. Tribl, G. Halliday, A. Gerlach, P. Riederer and K. L. Double. *Neuromelanin in human dopamine neurons: Comparison with peripheral melanins and relevance to Parkinson's disease.* Progress In Neurobiology **75**, 109–124 (2005).

73. Joseph R. Lakowicz. *Principles of Fluorescence Spectroscopy.* Springer (2006).

74. H. Du, R. C. A. Fuh, J. Z. Li, L. A. Corkan and J. S. Lindsey. *PhotochemCAD: A computer-aided design and research tool in photochemistry.* Photochemistry and Photobiology **68**, 141–142 (1998).

75. S. Andersson-Engels, Å Elner, J. Johansson, S. Karlsson, L. Salford, L. Strömblad, K. Svanberg and S. Svanberg. *Clinical recording of laser-induced fluorescence spectra for evaluation of tumour demarcation feasibility in selected clinical specialities.* Lasers in Medical Science **6**, 415–424 (1991).

76. N. Ramanujam. *Fluorescence spectroscopy of neoplastic and non-neoplastic tissues.* Neoplasia **2**, 89–117 (2000).

77. S. Andersson-Engels, C. af Klinteberg, K. Svanberg and S. Svanberg. *In vivo fluorescence imaging for tissue diagnostics.* Physics in Medicine and Biology **42**, 815–824 (1997).

78. K. Konig and I. Riemann. *High-resolution multiphoton tomography of human skin with subcellular spatial resolution and picosecond time resolution.* Journal of Biomedical Optics **8**, 432–439 (2003).

79. M. J. Koehler, K. Konig, P. Elsner, R. Buckle and M. Kaatz. *In vivo assessment of human skin aging by multiphoton laser scanning tomography.* Optics Letters **31**, 2879–2881 (2006).

80. B. R. Masters, P. T. C. So and E. Gratton. *Multiphoton excitation fluorescence microscopy and spectroscopy of in vivo human skin.* Biophysical Journal **72**, 2405–2412 (1997).

81. R. Drezek, K. Sokolov, U. Utzinger, I. Boiko, A. Malpica, M. Follen and R. Richards-Kortum. *Understanding the contributions of NADH and collagen to cervical tissue fluorescence spectra: Modeling, measurements, and implications.* Journal of Biomedical Optics **6**, 385–396 (2001).

82. J. V. Frangioni. *In vivo near-infrared fluorescence imaging.* Current Opinion in Biotechnology **7**, 626–634 (2003).

83. J. Caesar, S. Sherlock, S. Shaldon, L. Chiandussi and L. Guevara. *Use of Indocyanine Green In Measurement of Hepatic Blood Flow and As A Test of Hepatic Function.* Clinical Science **21**, 43–& (1961).

84. R. C. Benson and H. A. Kues. *Fluorescence Properties of Indocyanine Green As Related To Angiography.* Physics in Medicine and Biology **23**, 159–163 (1978).

85. J. C. Rasmussen, I. C. Tan, M. V. Marshall, C. E. Fife and E. M. Sevick-Muraca. *Lymphatic imaging in humans with near-infrared fluorescence.* Current Opinion in Biotechnology **20**, 74–82 (2009).

86. Gisbert Richard, Gisèle Soubrane and Lawrence A. Yannuzzi. *Fluorescein and ICG angiography: textbook and atlas.* Thieme (1998).

87. J. H. Rao, A. Dragulescu-Andrasi, H. Q. Yao and H. Q. Yao. *Fluorescence imaging in vivo: recent advances.* Current Opinion in Biotechnology **18**, 17–25 (2007).

88. E. M. Sevick-Muraca, J. P. Houston and M. Gurfinkel. *Fluorescence-enhanced, near infrared diagnostic imaging with contrast agents.* Current Opinion in Biotechnology **6**, 642–650 (2002).

89. A. Pelegrin, S. Folli, F. Buchegger, J. P. Mach, G. Wagnieres and H. Vandenbergh. *Antibody Fluorescein Conjugates For Photoimmunodiagnosis of Human Colon-carcinoma In Nude-mice.* Cancer **67**, 2529–2537 (1991).

90. S. Folli, P. Westermann, D. Braichotte, A. Pelegrin, G. Wagnieres, H. Vandenbergh and J. P. Mach. *Antibody-indocyanin Conjugates For Immunophotodetection of Human Squamous-cell Carcinoma In Nude-mice.* Cancer Research **54**, 2643–2649 (1994).

91. S. Folli, G. Wagnieres, A. Pelegrin, J. M. Calmes, D. Braichotte, F. Buchegger, Y. Chalandon, N. Hardman, C. Heusser, J. C. Givel, G. Chapuis, A. Chatelain, H. Vandenbergh and J. P. Mach. *Immunophotodiagnosis of Colon Carcinomas In Patients Injected With Fluoresceinated Chimeric Antibodies Against Carcinoembryonic Antigen.* Proceedings of the National Academy of Sciences of the United States of America **89**, 7973–7977 (1992).

92. S. Ke, X. X. Wen, M. Gurfinkel, C. Charnsangavej, S. Wallace, E. M. Sevick-Muraca and C. Li. *Near-infrared optical imaging of epidermal growth factor receptor in breast cancer xenografts.* Cancer Research **63**, 7870–7875 (2003).

93. X. H. Gao, Y. Y. Cui, R. M. Levenson, L. W. K. Chung and S. M. Nie. *In vivo cancer targeting and imaging with semiconductor quantum dots.* Nature Biotechnology **22**, 969–976 (2004).

94. R. Y. Tsien. *The green fluorescent protein.* Annual Review of Biochemistry **67**, 509–544 (1998).

95. R. E. Campbell, O. Tour, A. E. Palmer, P. A. Steinbach, G. S. Baird, D. A. Zacharias and R. Y. Tsien. *Live tissue intrinsic emission microscopy using multiphoton-excited native fluorescence and second harmonic generation.* Proceedings of the National Academy of Sciences of the United States of America **99**, 7877–7882 (2002).

96. N. C. Shaner, R. E. Campbell, P. A. Steinbach, B. N. G. Giepmans, A. E. Palmer and R. Y. Tsien. *Improved monomeric red, orange and yellow fluorescent proteins derived from Discosoma sp red fluorescent protein.* Nature Biotechnology **22**, 1567–1572 (2004).

97. N. C. Shaner, P. A. Steinbach and R. Y. Tsien. *A guide to choosing fluorescent proteins.* Nature Methods **2**, 905–909 (2005).

98. I. L. Medintz, H. T. Uyeda, E. R. Goldman and H. Mattoussi. *Quantum dot bioconjugates for imaging, labelling and sensing.* Nature Materials **4**, 435–446 (2005).

99. X. H. Gao, L. L. Yang, J. A. Petros, F. F. Marshal, J. W. Simons and S. M. Nie. *In vivo molecular and cellular imaging with quantum dots.* Current Opinion in Biotechnology **16**, 63–72 (2005).

100. R. Hardman. *A toxicologic review of quantum dots: Toxicity depends on physicochemical and environmental factors.* Environmental Health Perspectives **114**, 165–172 (2006).

101. S. R. Arridge. *Optical tomography in medical imaging.* Inverse Problems **15**, R41–R93 (1999).

102. B. C. Wilson and G. Adam. *A Monte-carlo Model For the Absorption and Flux Distributions of Light In Tissue.* Medical Physics **10**, 824–830 (1983).

103. L. H. Wang, S. L. Jacques and L. Q. Zheng. *Mcml - Monte-carlo Modeling of Light Transport In Multilayered Tissues.* Computer Methods and Programs In Biomedicine **47**, 131–146 (1995).

104. D. A. Boas, J. P. Culver, J. J. Stott and A. K. Dunn. *Three dimensional Monte Carlo code for photon migration through complex heterogeneous media including the adult human head.* Optics Express **10**, 159–170 (2002).

105. A. Kienle and M. S. Patterson. *Determination of the optical properties of turbid media from a single Monte Carlo simulation.* Physics in Medicine and Biology **41**, 2221–2227 (1996).

106. A. Pifferi, P. Taroni, G. Valentini and S. Andersson-Engels. *Real-time method for fitting time-resolved reflectance and transmittance measurements with a Monte Carlo model.* Applied Optics **37**, 2774–2780 (1998).

107. E. Alerstam, S. Andersson-Engels and T. Svensson. *White Monte Carlo for time-resolved photon migration.* Journal of Biomedical Optics **13**, 041304 (2008).

108. Erik Alerstam, Stefan Andersson-Engels and Tomas Svensson. *Improved accuracy in time-resolved diffuse reflectance spectroscopy.* Optics Express **16**, 10440–10454 (2008).

109. Q. Q. Fang and D. A. Boas. *Monte Carlo Simulation of Photon Migration in 3D Turbid Media Accelerated by Graphics Processing Units.* Optics Express **17**, 20178–20190 (2009).

110. N. N. Ren, J. M. Liang, X. C. Qu, J. F. Li, B. J. Lu and J. Tian. *GPU-based Monte Carlo simulation for light propagation in complex heterogeneous tissues.* Optics Express **18**, 6811–6823 (2010).

111. S. Wright, M. Schweiger and S. R. Arridge. *Reconstruction in optical tomography using the P(N) approximations.* Measurement Science & Technology **18**, 79–86 (2007).

112. A. Liemert and A. Kienle. *Analytical solution of the radiative transfer equation for infinite-space fluence.* Physical Review A **83**, 015804 (2011).

113. A. Liemert and A. Kienle. *Analytical Green's function of the radiative transfer radiance for the infinite medium.* Physical Review E **83**, 036605 (2011).

114. T. Durduran, A. G. Yodh, B. Chance and D. A. Boas. *Does the photon-diffusion coefficient depend on absorption?* Journal of the Optical Society of America A - Optics Image Science and Vision **14**, 3358–3365 (1997).

115. M. Schweiger, S. R. Arridge, M. Hiraoka and D. T. Delpy. *The Finite-element Method For the Propagation of Light In Scattering Media - Boundary and Source Conditions.* Medical Physics **22**, 1779–1792 (1995).

116. M. Keijzer, W. M. Star and P. R. M. Storchi. *Optical Diffusion In Layered Media.* Applied Optics **27**, 1820–1824 (1988).

117. M. S. Patterson, B. Chance and B. C. Wilson. *Time Resolved Reflectance and Transmittance For the Noninvasive Measurement of Tissue Optical-properties.* Applied Optics **28**, 2331–2336 (1989).

118. A. Liemert and A. Kienle. *Light diffusion in N-layered turbid media: steady-state domain.* Journal of Biomedical Optics **15**, 025003 (2010).

119. A. Liemert and A. Kienle. *Light diffusion in N-layered turbid media: frequency and time domains.* Journal of Biomedical Optics **15**, 025002 (2010).

120. TOAST. Time-resolved Optical Absorption and Scattering Tomography (2012). URL http://web4.cs.ucl.ac.uk/research/vis/toast/index.html.

121. S. R. Arridge, M. Schweiger, M. Hiraoka and D. T. Delpy. *A Finite-element Approach For Modeling Photon Transport In Tissue.* Medical Physics **20**, 299–309 (1993).

122. Nirfast. Near Infrared Frequency Domain Absorption and Scatter Tomography (2012). URL www.nirfast.org.

123. H. Dehghani, M. E. Eames, P. K. Yalavarthy, S. C. Davis, S. Srinivasan, C. M. Carpenter, B. W. Pogue and K. D. Paulsen. *Near infrared optical tomography using NIRFAST: Algorithm for numerical model and image reconstruction.* Communications in Numerical Methods in Engineering **25**, 711–732 (2009).

124. B. Dogdas, D. Stout, A. F. Chatziioannou and R. M. Leahy. *Digimouse: a 3D whole body mouse atlas from CT and cryosection data.* Physics in Medicine and Biology **52**, 577–587 (2007).

125. V. Ntziachristos, C. Bremer and R. Weissleder. *Fluorescence imaging with near-infrared light: new technological advances that enable in vivo molecular imaging.* European Radiology **13**, 195–208 (2003).

126. Frederic Leblond, Scott C. Davis, Pablo A. Valdes and Brian W. Pogue. *Pre-clinical whole-body fluorescence imaging: Review of instruments, methods and applications.* Journal of Photochemistry and Photobiology B - Biology **98**, 77–94 (2010).

127. Robert R. Alfano, Tata Darayashb, Julius Corderop, Hilip Tomashefsky, Frankw.longo and Michele A. Alfano. *Laser Induced Fluorescence Spectroscopy from Native Cancerous and Normal Tissue.* IEEE Journal of Quantum Electronics **20**, 1507–1511 (1984).

128. S. Montan, K. Svanberg and S. Svanberg. *Multicolor Imaging and Contrast Enhancement In Cancer-tumor Localization Using Laser-induced Fluorescence In Hematoporphyrin-derivative-bearing Tissue.* Optics Letters **10**, 56–58 (1985).

129. P. S. Andersson, S. Montan and S. Svanberg. *Multispectral System For Medical Fluorescence Imaging.* IEEE Journal of Quantum Electronics **23**, 1798–1805 (1987).

130. M. A. OLeary, D. A. Boas, B. Chance and A. G. Yodh. *Reradiation and Imaging of Diffuse Photon Density Waves Using Fluorescent Inhomogeneities.* Journal of Luminescence **60-1**, 281–286 (1994).

131. J. H. Chang, H. L. Graber and R. L. Barbour. *Imaging of fluorescence in highly scattering media.* IEEE Transactions On Biomedical Engineering **44**, 810–822 (1997).

132. P. I. H. Bastiaens and A. Squire. *Fluorescence lifetime imaging microscopy: spatial resolution of biochemical processes in the cell.* Trends In Cell Biology **9**, 48–52 (1999).

133. M. A. OLeary, D. A. Boas, X. D. Li, B. Chance and A. G. Yodh. *Fluorescence lifetime imaging in turbid media.* Optics Letters **21**, 158–160 (1996).

134. D. Y. Paithankar, A. U. Chen, B. W. Pogue, M. S. Patterson and E. M. SevickMuraca. *Imaging of fluorescent yield and lifetime from multiply scattered light reemitted from random media.* Applied Optics **36**, 2260–2272 (1997).

135. J. S. Reynolds, T. L. Troy, R. H. Mayer, A. B. Thompson, D. J. Waters, K. K. Cornell, P. W. Snyder and E. M. Sevick-Muraca. *Imaging of spontaneous canine mammary tumors using fluorescent contrast agents.* Photochemistry and Photobiology **70**, 87–94 (1999).

136. A. T. N. Kumar, J. Skoch, B. J. Bacskai, D. A. Boas and A. K. Dunn. *Fluorescence-lifetime-based tomography for turbid media.* Optics Letters **30**, 3347–3349 (2005).

137. V. Y. Soloviev, K. B. Tahir, J. McGinty, D. S. Elson, M. A. A. Neil, P. M. W. French and S. R. Arridge. *Fluorescence lifetime imaging by using time-gated data acquisition.* Applied Optics **46**, 7384–7391 (2007).

138. E. A. Jares-Erijman and T. M. Jovin. *FRET imaging.* Nature Biotechnology **21**, 1387–1395 (2003).

139. J. McGinty, V. Y. Soloviev, K. B. Tahir, R. Laine, D. W. Stuckey, J. V. Hajnal, A. Sardini, P. M. W. French and S. R. Arridge. *Three-dimensional imaging of Forster resonance energy transfer in heterogeneous turbid media by tomographic fluorescent lifetime imaging.* Optics Letters **34**, 2772–2774 (2009).

140. F. Gao, J. A. Li, L. M. Zhang, P. Poulet, H. J. Zhao and Y. Yamada. *Simultaneous fluorescence yield and lifetime tomography from time-resolved transmittances of small-animal-sized phantom.* Applied Optics **49**, 3163–3172 (2010).

141. V. Gaind, S. Kularatne, P. S. Low and K. J. Webb. *Deep-tissue imaging of intramolecular fluorescence resonance energy-transfer parameters.* Optics Letters **35**, 1314–1316 (2010).

142. L. Feng, K. M. Yoo and R. R. Alfano. *Ultrafast Laser-pulse Transmission and Imaging Through Biological Tissues.* Applied Optics **32**, 554–558 (1993).

143. S Andersson-Engels, R Berg, S Svanberg and O Jarlman. *Time-Resolved Transillumination for medical diagnostics.* Optics Letters **15**, 1179–1181 (1990).

144. Tomas Svensson, Erik Alerstam, Dmitry Khoptyar, Jonas Johansson, Staffan Folestad and Stefan Andersson-Engels. *Near-infrared photon time-of-flight spectroscopy of turbid materials up to 1400 nm.* Review of Scientific Instruments **80** (2009).

145. A. Torricelli, A. Pifferi, P. Taroni, E. Giambattistelli and R. Cubeddu. *In vivo optical characterization of human tissues from 610 to 1010 nm by time-resolved reflectance spectroscopy.* Physics in Medicine and Biology **46**, 2227–2237 (2001).

146. Frederic Leblond, Hamid Dehghani, Dax Kepshire and Brian W. Pogue. *Early-photon fluorescence tomography: spatial resolution improvements and noise stability considerations.* Journal of the Optical Society of America A - Optics Image Science and Vision **26**, 1444–1457 (2009).

147. Mark J. Niedre, Ruben H. de Kleine, Elena Aikawa, David G. Kirsch, Ralph Weissleder and Vasilis Ntziachristos. *Early photon tomography allows fluorescence detection of lung carcinomas and disease progression in mice in vivo.* Proceedings of the National Academy of Sciences of the United States of America **105**, 19126–19131 (2008).

148. AJ Chaudhari, F Darvas, JR Bading, RA Moats, PS Conti, DJ Smith, SR Cherry and RM Leahy. *Hyperspectral and multispectral bioluminescence optical tomography for small animal imaging.* Physics in Medicine And Biology **50**, 5421–5441 (2005).

149. H Dehghani, SC Davis, SD Jiang, BW Pogue, KD Paulsen and MS Patterson. *Spectrally resolved bioluminescence optical tomography.* Optics Letters **31**, 365–367 (2006).

150. G Zavattini, S Vecchi, G Mitchell, U Weisser, RM Leahy, BJ Pichler, DJ Smith and SR Cherry. *A hyperspectral fluorescence system for 3D in vivo optical imaging.* Physics in Medicine and Biology **51**, 2029–2043 (2006).

151. Abhijit J. Chaudhari, Sangtae Ahn, Richard Levenson, Ramsey D. Badawi, Simon R. Cherry and Richard M. Leahy. *Excitation spectroscopy in multispectral optical fluorescence tomography: methodology, feasibility and computer simulation studies.* Physics in Medicine and Biology **54**, 4687–4704 (2009).

152. Alexander D. Klose and Thomas Poeschinger. *Excitation-resolved fluorescence tomography with simplified spherical harmonics equations.* Physics in Medicine and Biology **56**, 1443–1469 (2011).

153. A. D. Klose. *Hyperspectral excitation-resolved fluorescence tomography of quantum dots.* Optics Letters **34**, 2477–2479 (2009).

154. D. K. Chatterjee, L. S. Fong and Y. Zhang. *Nanoparticles in photodynamic therapy: An emerging paradigm.* Advanced Drug Delivery Reviews **60**, 1627–1637 (2008).

155. Can T. Xu, Johan Axelsson and Stefan Andersson-Engels. *Fluorescence diffuse optical tomography using upconverting nanoparticles.* Applied Physics Letters **94** (2009).

156. Claudio Vinegoni, Daniel Razansky, Scott A. Hilderbrand, Fangwei Shao, Vasilis Ntziachristos and Ralph Weissleder. *Transillumination fluorescence imaging in mice using biocompatible upconverting nanoparticles.* Optics Letters **34**, 2566–2568 (2009).

157. H. Xu, L. Cheng, C. Wang, X. X. Ma, Y. G. Li and Z. Liu. *Polymer encapsulated upconversion nanoparticle/iron oxide nanocomposites for multimodal imaging and magnetic targeted drug delivery.* Biomaterials **32**, 9364–9373 (2011).

158. A. Xia, Y. Gao, J. Zhou, C. Y. Li, T. S. Yang, D. M. Wu, L. M. Wu and F. Y. Li. *Core-shell NaYF(4):Yb(3+),Tm(3+)@Fe(x)O(y) nanocrystals for dual-modality T(2)-enhanced magnetic resonance and NIR-to-NIR upconversion luminescent imaging of small-animal lymphatic node.* Biomaterials **32**, 7200–7208 (2011).

159. L. A. Cheng, K. Yang, M. W. Shao, S. T. Lee and Z. A. Liu. *Multicolor In Vivo Imaging of Upconversion Nanopaticles with Emissions Tuned by Luminescence Resonance Energy Transfer.* Journal of Physical Chemistry C **115**, 2686–2692 (2011).

160. T. Y. Cao, Y. Yang, Y. A. Gao, J. Zhou, Z. Q. Li and F. Y. Li. *High-quality water-soluble and surface-functionalized upconversion nanocrystals as luminescent probes for bioimaging.* Biomaterials **32**, 2959–2968 (2011).

161. J. Zhou, Y. Sun, X. X. Du, L. Q. Xiong, H. Hu and F. Y. Li. *Dual-modality in vivo imaging using rare-earth nanocrystals with near-infrared to near-infrared (NIR-to-NIR) upconversion luminescence and magnetic resonance properties.* Biomaterials **31**, 3287–3295 (2010).

162. L. Q. Xiong, T. S. Yang, Y. Yang, C. J. Xu and F. Y. Li. *Long-term in vivo biodistribution imaging and toxicity of polyacrylic acid-coated upconversion nanophosphors.* Biomaterials **31**, 7078–7085 (2010).

163. L. Q. Xiong, Z. G. Chen, M. X. Yu, F. Y. Li, C. Liu and C. H. Huang. *Synthesis, characterization, and in vivo targeted imaging of amine-functionalized rare-earth up-converting nanophosphors.* Biomaterials **30**, 5592–5600 (2009).

164. L. Q. Xiong, Z. G. Chen, Q. W. Tian, T. Y. Cao, C. J. Xu and F. Y. Li. *High Contrast Upconversion Luminescence Targeted Imaging in Vivo Using Peptide-Labeled Nanophosphors.* Analytical Chemistry **81**, 8687–8694 (2009).

165. Qiuqiang Zhan, Jun Qian, Huijuan Liang, Gabriel Somesfalean, Dan Wang, Sailing He, Zhiguo Zhang and Stefan Andersson-Engels. *Using 915 nm Laser Excited Tm3+/Er3+/Ho3+-Doped NaYbF4 Upconversion Nanoparticles for in Vitro and Deeper in Vivo Bioimaging without Overheating Irradiation.* Acs Nano **5**, 3744–3757 (2011).

166. Haichun Liu, Can T. Xu and Stefan Andersson-Engels. *Multibeam fluorescence diffuse optical tomography using upconverting nanoparticles.* Optics Letters **35**, 718–720 (2010).

167. E. M. C. Hillman and A. Moore. *All-optical anatomical co-registration for molecular imaging of small animals using dynamic contrast.* Nature Photonics **1**, 526–530 (2007).

168. Xin Liu, Daifa Wang, Fei Liu and Jing Bai. *Principal component analysis of dynamic fluorescence diffuse optical tomography images.* Optics Express **18**, 6300–6314 (2010).

169. E. M. C. Hillman, C. B. Amoozegar, T. Wang, A. F. H. McCaslin, M. B. Bouchard, J. Mansfield and R. M. Levenson. *In vivo optical imaging and dynamic contrast methods for biomedical research.* Philosophical Transactions of the Royal Society A - Mathematical Physical and Engineering Sciences **369**, 4620–4643 (2011).

170. X. Liu, F. Liu, Y. Zhang and J. Bai. *Unmixing Dynamic Fluorescence Diffuse Optical Tomography Images With Independent Component Analysis.* IEEE Transactions On Medical Imaging **30**, 1591–1604 (2011).

171. S. V. Patwardhan, S. R. Bloch, S. Achilefu and J. P. Culver. *Time-dependent whole-body fluorescence tomography of probe bio-distributions in mice.* Optics Express **13**, 2564–2577 (2005).

172. E. E. Graves, J. Ripoll, R. Weissleder and V. Ntziachristos. *A submillimeter resolution fluorescence molecular imaging system for small animal imaging.* Medical Physics **30**, 901–911 (2003).

173. N. Deliolanis, T. Lasser, D. Hyde, A. Soubret, J. Ripoll and V. Ntziachristos. *Free-space fluorescence molecular tomography utilizing 360 degrees geometry projections.* Optics Letters **32**, 382–384 (2007).

174. Yuting Lin, William C. Barber, Jan S. Iwanczyk, Werner Roeck, Orhan Nalcioglu and Gultekin Gulsen. *Quantitative fluorescence tomography using a combined tri-modality FT/DOT/XCT system.* Optics Express **18**, 7835–7850 (2010).

175. R. B. Schulz, A. Ale, A. Sarantopoulos, M. Freyer, E. Soehngen, M. Zientkowska and V. Ntziachristos. *Hybrid System for Simultaneous Fluorescence and X-Ray Computed Tomography.* IEEE Transactions On Biomedical Engineering **29**, 465–473 (2010).

176. A. Godavarty, M. J. Eppstein, C. Y. Zhang, S. Theru, A. B. Thompson, M. Gurfinkel and E. M. Sevick-Muraca. *Fluorescence-enhanced optical imaging in large tissue volumes using a gain-modulated ICCD camera.* Physics in Medicine and Biology **48**, 1701–1720 (2003).

177. D. J. Cuccia, F. Bevilacqua, A. J. Durkin and B. J. Tromberg. *Modulated imaging: quantitative analysis and tomography of turbid media in the spatial-frequency domain.* Optics Letters **30**, 1354–1356 (2005).

178. A. Kim, M. Roy, F. N. Dadani and B. C. Wilson. *Topographic mapping of subsurface fluorescent structures in tissue using multiwavelength excitation.* Journal of Biomedical Optics **15**, 066026 (2010).

179. A. Mazhar, D. J. Cuccia, S. Gioux, A. J. Durkin, J. V. Frangioni and B. J. Tromberg. *Structured illumination enhances resolution and contrast in thick tissue fluorescence imaging.* Journal of Biomedical Optics **15**, 010506 (2010).

180. V. Venugopal, J. Chen, F. Lesage and X. Intes. *Full-field time-resolved fluorescence tomography of small animals.* Optics Letters **35**, 3189–3191 (2010).

181. V. Ntziachristos and R. Weissleder. *Experimental three-dimensional fluorescence reconstruction of diffuse media by use of a normalized Born approximation.* Optics Letters **26**, 893–895 (2001).

182. A. Soubret, J. Ripoll and V. Ntziachristos. *Accuracy of fluorescent tomography in the presence of heterogeneities: Study of the normalized born ratio.* IEEE Transactions On Biomedical Engineering **24**, 1377–1386 (2005).

183. S. R. Arridge and J. C. Hebden. *Optical imaging in medicine .2. Modelling and reconstruction.* Physics in Medicine and Biology **42**, 841–853 (1997).

184. B. W. Pogue, T. O. McBride, J. Prewitt, U. L. Osterberg and K. D. Paulsen. *Spatially variant regularization improves diffuse optical tomography.* Applied Optics **38**, 2950–2961 (1999).

185. Johan Axelsson, Jenny Svensson and Stefan Andersson-Engels. *Spatially varying regularization based on spectrally resolved fluorescence emission in fluorescence molecular tomography.* Optics Express **15**, 13574–13584 (2007).

186. J Swartling, J Svensson, D Bengtsson, K Terike and S Andersson-Engels. *Fluorescence spectra provide information on the depth of fluorescent lesions in tissue.* Applied Optics **44**, 1934–1941 (2005). Biomedical Topical Meeting, Miami Beach, FL, APR, 2004.

187. Damon Hyde, Eric L. Miller, Dana H. Brooks and Vasilis Ntziachristos. *Data Specific Spatially Varying Regularization for Multimodal Fluorescence Molecular Tomography.* IEEE Transactions on Medical Imaging **29**, 365–374 (2010).

188. Angelique Ale, Ralf B. Schulz, Athanasios Sarantopoulos and Vasilis Ntziachristos. *Imaging performance of a hybrid x-ray computed tomography-fluorescence molecular tomography system using priors.* Medical Physics **37**, 1976–1986 (2010).

189. S. C. Davis, H. Dehghani, J. Wang, S. Jiang, B. W. Pogue and K. D. Paulsen. *Image-guided diffuse optical fluorescence tomography implemented with Laplacian-type regularization.* Optics Express **15**, 4066–4082 (2007).

190. R. Weissleder, K. Kelly, E. Y. Sun, T. Shtatland and L. Josephson. *Cell-specific targeting of nanoparticles by multivalent attachment of small molecules.* Nature Biotechnology **23**, 1418–1423 (2005).

191. W. B. Cai, D. W. Shin, K. Chen, O. Gheysens, Q. Z. Cao, S. X. Wang, S. S. Gambhir and X. Y. Chen. *Peptide-labeled near-infrared quantum dots for imaging tumor vasculature in living subjects.* Nano Letters **6**, 669–676 (2006).

192. R. Paulmurugan, Y. Umezawa and S. S. Gambhir. *Noninvasive imaging of protein-protein interactions in living subjects by using reporter protein complementation and reconstitution strategies.* Proceedings of the National Academy of Sciences of the United States of America **99**, 15608–15613 (2002).

193. M. Yang, E. Baranov, A. R. Moossa, S. Penman and R. M. Hoffman. *Visualizing gene expression by whole-body fluorescence imaging.* Proceedings of the National Academy of Sciences of the United States of America **97**, 12278–12282 (2000).

194. C. Vinegoni, I. Botnaru, E. Aikawa, M. A. Calfon, Y. Iwamoto, E. J. Folco, V. Ntziachristos, R. Weissleder, P. Libby and F. A. Jaffer. *Indocyanine Green Enables Near-Infrared Fluorescence Imaging of Lipid-Rich, Inflamed Atherosclerotic Plaques.* Science Translational Medicine **3**, 84ra45 (2011).

195. V. Ntziachristos, J. Ripoll and R. Weissleder. *Would near-infrared fluorescence signals propagate through large human organs for clinical studies?* Optics Letters **27**, 333–335 (2002).

196. A. Corlu, R. Choe, T. Durduran, M. A. Rosen, M. Schweiger, S. R. Arridge, M. D. Schnall and A. G. Yodh. *Three-dimensional in vivo fluorescence diffuse optical tomography of breast cancer in humans.* Optics Express **15**, 6696–6716 (2007).

197. E. M. Sevick-Muraca, R. Sharma, J. C. Rasmussen, M. V. Marshall, J. A. Wendt, H. Q. Pham, E. Bonefas, J. P. Houston, L. Sampath, K. E. Adams, D. K. Blanchard, R. E. Fisher, S. B. Chiang, R. Elledge and M. E. Mawad. *Imaging of lymph flow in breast cancer patients after microdose administration of a near-infrared flurophore: Feasibility study.* Radiology **246**, 734–741 (2008).

198. F. Wang and X. G. Liu. *Recent advances in the chemistry of lanthanide-doped upconversion nanocrystals.* Chemical Society Reviews **38**, 976–989 (2009).

199. H. S. Mader, P. Kele, S. M. Saleh and O. S. Wolfbeis. *Upconverting luminescent nanoparticles for use in bioconjugation and bioimaging.* Current Opinion in Biotechnology **14**, 582–596 (2010).

200. F. Wang, D. Banerjee, Y. S. Liu, X. Y. Chen and X. G. Liu. *Upconversion nanoparticles in biological labeling, imaging, and therapy.* Analyst **135**, 1839–1854 (2010).

201. Xiaoxiao He, Kemin Wang and Zhen Cheng. *In vivo near-infrared fluorescence imaging of cancer with nanoparticle-based probes.* Wiley Interdisciplinary Reviews-nanomedicine and Nanobiotechnology **2**, 349–366 (2010).

202. Dev K. Chatterjee, Muthu Kumara Gnanasammandhan and Yong Zhang. *Small Upconverting Fluorescent Nanoparticles for Biomedical Applications.* Small **6**, 2781–2795 (2010).

203. N. Bloembergen. *Solid State Infrared Quantum Counters.* Physical Review Letters **2**, 84–85 (1959).

204. F. Auzel. *Compteur Quantique Par Transfert Denergie Entre Deux Ions De Terres Rares Dans Un Tungstate Mixte Et Dans Un Verre.* Comptes Rendus Hebdomadaires Des Seances De L Academie Des Sciences Serie B **262**, 1016–& (1966).

205. V. V. Ovsyakin and P. P. Feofilov. *Cooperative Sensitization of Luminescence In Crystals Activated With Rare Earth Ions.* Jetp Letters - USSR **4**, 317–& (1966).

206. S. Heer, O. Lehmann, M. Haase and H. U. Gudel. *Blue, green, and red upconversion emission from lanthanide-doped LuPO4 and YbPO4 nanocrystals in a transparent colloidal solution.* Angewandte Chemie-international Edition **42**, 3179–3182 (2003).

207. K. W. Kramer, D. Biner, G. Frei, H. U. Gudel, M. P. Hehlen and S. R. Luthi. *Hexagonal sodium yttrium fluoride based green and blue emitting upconversion phosphors.* Chemistry of Materials **16**, 1244–1251 (2004).

208. G. S. Yi and G. M. Chow. *Synthesis of hexagonal-phase NaYF4 : Yb,Er and NaYF4 : Yb,Tm nanocrystals with efficient up-conversion fluorescence.* Advanced Functional Materials **16**, 2324–2329 (2006).

209. Z. Q. Li and Y. Zhang. *Monodisperse silica-coated polyvinylpyrrolidone/NaYF4 nanocrystals with multicolor upconversion fluorescence emission.* Angewandte Chemie-international Edition **45**, 7732–7735 (2006).

210. J. C. Boyer, L. A. Cuccia and J. A. Capobianco. *Synthesis of colloidal upconverting NaYF4 : Er3+/Yb3+ and Tm3+/Yb3+ monodisperse nanocrystals.* Nano Letters **7**, 847–852 (2007).

211. Z. Q. Li, Y. Zhang and S. Jiang. *Multicolor Core/Shell-Structured Upconversion Fluorescent Nanoparticles.* Advanced Materials **20**, 4765–+ (2008).

212. F. Wang, J. A. Wang and X. G. Liu. *Direct Evidence of a Surface Quenching Effect on Size-Dependent Luminescence of Upconversion Nanoparticles.* Angewandte Chemie-international Edition **49**, 7456–7460 (2010).

213. H. S. Qian and Y. Zhang. *Synthesis of Hexagonal-Phase Core-Shell NaYF4 Nanocrystals with Tunable Upconversion Fluorescence.* Langmuir **24**, 12123–12125 (2008).

214. P. Ayyub, V. R. Palkar, S. Chattopadhyay and M. Multani. *Effect of Crystal Size-reduction On Lattice Symmetry and Cooperative Properties.* Physical Review B **51**, 6135–6138 (1995).

215. F. Wang, Y. Han, C. S. Lim, Y. H. Lu, J. Wang, J. Xu, H. Y. Chen, C. Zhang, M. H. Hong and X. G. Liu. *Simultaneous phase and size control of upconversion nanocrystals through lanthanide doping.* Nature **463**, 1061–1065 (2010).

216. R. Kumar, M. Nyk, T. Y. Ohulchanskyy, C. A. Flask and P. N. Prasad. *Combined Optical and MR Bioimaging Using Rare Earth Ion Doped NaYF(4) Nanocrystals.* Advanced Functional Materials **19**, 853–859 (2009).

217. Z. Q. Li, Y. Zhang, B. Shuter and N. M. Idris. *Hybrid Lanthanide Nanoparticles with Paramagnetic Shell Coated on Upconversion Fluorescent Nanocrystals.* Langmuir **25**, 12015–12018 (2009).

218. G. Y. Chen, T. Y. Ohulchanskyy, W. C. Law, H. Agren and P. N. Prasad. *Monodisperse NaYbF(4): Tm(3+)/NaGdF(4) core/shell nanocrystals with near-infrared to near-infrared upconversion photoluminescence and magnetic resonance properties.* Nanoscale **3**, 2003–2008 (2011).

219. D. K. Chatterjee, Abdul J. Rufalhah and Yong Zhang. *Upconversion fluorescence imaging of cells and small animals using lanthanide doped nanocrystals.* Biomaterials **29**, 937–943 (2008).

220. H. Kobayashi, N. Kosaka, M. Ogawa, N. Y. Morgan, P. D. Smith, C. B. Murray, X. C. Ye, J. Collins, G. A. Kumar, H. Bell and P. L. Choyke. *In vivo multiple color lymphatic imaging using upconverting nanocrystals.* Journal of Materials Chemistry **19**, 6481–6484 (2009).

221. L. A. Cheng, K. Yang, S. A. Zhang, M. W. Shao, S. T. Lee and Z. A. Liu. *Highly-Sensitive Multiplexed in vivo Imaging Using PEGylated Upconversion Nanoparticles.* Nano Research **3**, 722–732 (2010).

222. Sounderya Nagarajan and Yong Zhang. *Upconversion fluorescent nanoparticles as a potential tool for in-depth imaging.* Nanotechnology **22** (2011).

223. L. Zhang, H. F. Hu, C. H. Qi and F. Y. Lin. *Spectroscopic properties and energy transfer in Yb3+/Er3+-doped phosphate glasses.* Optical Materials **17**, 371–377 (2001).

224. Li Ching Ong, Muthu Kumara Gnanasammandhan, Sounderya Nagarajan and Yong Zhang. *Upconversion: road to El Dorado of the fluorescence world.* Luminescence **25**, 290–293 (2010).

225. J. F. Suyver, J. Grimm, M. K. van Veen, D. Biner, K. W. Kramer and H. U. Gudel. *Upconversion spectroscopy and properties of NaYF4 doped with Er (3+), Tm3+ and/or Yb3+.* Journal of Luminescence **117**, 1–12 (2006).

226. JF Suyver, A Aebischer, D Biner, P Gerner, J Grimm, S Heer, KW Kramer, C Reinhard and HU Gudel. *Novel materials doped with trivalent lanthanides and transition metal ions showing near-infrared to visible photon upconversion.* Optical Materials **27**, 1111–1130 (2005).

227. Guang-Shun Yi and Gan-Moog Chow. *Water-soluble NaYF4 : Yb,Er(Tm)/NaYF4/polymer core/shell/shell nanoparticles with significant enhancement of upconversion fluorescence.* Chemistry of materials **19**, 341–343 (2007).

228. John-Christopher Boyer and Frank C. J. M. van Veggel. *Absolute quantum yield measurements of colloidal NaYF(4): Er(3+), Yb(3+) upconverting nanoparticles.* Nanoscale **2**, 1417–1419 (2010).

229. M. Pollnau, D. R. Gamelin, S. R. Luthi, H. U. Gudel and M. P. Hehlen. *Power dependence of upconversion luminescence in lanthanide and transition-metal-ion systems.* Physical Review B **61**, 3337–3346 (2000).

230. P. Ayyub, V. R. Palkar, S. Chattopadhyay and M. Multani. *Anomalous power dependence of sensitized upconversion luminescence.* Physical Review B **71**, 125123 (2005).

231. F. E. Auzel. *Materials and Devices Using Double-pumped Phosphors With Energy-transfer.* Proceedings of the IEEE **61**, 758–786 (1973).

232. C. Y. Chien, G. Korn, J. S. Coe, J. Squier and G. Mourou. *Highly Efficient 2nd-harmonic Generation of Ultraintense Nd-glass Laser-pulses.* Optics Letters **20**, 353–355 (1995).

233. A. Bril, J. L. Sommerdijk and A. W. D. Jager. *Efficiency of Yb3+-er3+ Activated Up-conversion Phosphors.* Journal of the Electrochemical Society **122**, 660–663 (1975).

234. O. Ehlert, R. Thomann, M. Darbandi and T. Nann. *A four-color colloidal multiplexing nanoparticle systems.* Acs Nano **2**, 120–124 (2008).

235. Q. Q. Dou and Y. Zhang. *Tuning of the Structure and Emission Spectra of Upconversion Nanocrystals by Alkali Ion Doping.* Langmuir **27**, 13236–13241 (2011).

236. H. H. Gorris, R. Ali, S. M. Saleh and O. S. Wolfbeis. *Tuning the Dual Emission of Photon-Upconverting Nanoparticles for Ratiometric Multiplexed Encoding.* Advanced Materials **23**, 1652–+ (2011).

237. L. Cheng, K. Yang, M. W. Shao, X. H. Lu and Z. Liu. *In vivo pharmacokinetics, long-term biodistribution and toxicology study of functionalized upconversion nanoparticles in mice.* Nanomedicine **6**, 1327–1340 (2011).

238. S. F. Lim, R. Riehn, C. K. Tung, W. S. Ryu, R. Zhuo, J. Dalland and R. H. Austin. *Upconverting nanophosphors for bioimaging.* Nanotechnology **20**, 405701 (2009).

239. S. H. Nam, Y. M. Bae, Y. Il Park, J. H. Kim, H. M. Kim, J. S. Choi, K. T. Lee, T. Hyeon and Y. D. Suh. *Long-Term Real-Time Tracking of Lanthanide Ion Doped Upconverting Nanoparticles in Living Cells.* Angewandte Chemie-international Edition **50**, 6093–6097 (2011).

240. Z. Q. Li and Y. Zhang. *An efficient and user-friendly method for the synthesis of hexagonal-phase NaYF(4): Yb, Er/Tm nanocrystals with controllable shape and upconversion fluorescence.* Nanotechnology **19**, 345606 (2008).

241. TW Olsen, SY Aaberg, DH Geroski and HF Edelhauser. *Human sclera: Thickness and surface area.* American Journal of Ophthalmology **125**, 237–241 (1998).

242. Y. Ikuno, K. Kawaguchi, T. Nouchi and Y. Yasuno. *Choroidal Thickness in Healthy Japanese Subjects.* Investigative Ophthalmology & Visual Science **51**, 2173–2176 (2010).

243. M Hammer, A Roggan, D Schweitzer and G Müller. *Optical properties of ocular fundus tissues - an in vitro study using the double-integrating-sphere technique and inverse Monte Carlo simulation.* Physics in Medicine and Biology **40**, 963–978 (1995).

244. A. N. Bashkatov, E. A. Genina, V. I. Kochubey and V. V. Tuchin. *Optical properties of human sclera in spectral range 370-2500 nm.* Optics and Spectroscopy **109**, 197–204 (2010).

245. B. Nemati, H. G. Rylander and A. J. Welch. *Optical properties of conjunctiva, sclera, and the ciliary body and their consequences for transscleral cyclophotocoagulation.* Applied Optics **35**, 3321–3327 (1996).

246. Brian W. Pogue and Michael S. Patterson. *Review of tissue simulating phantoms for optical spectroscopy, imaging and dosimetry.* Journal of Biomedical Optics **11** (2006).

247. T Sarna and Rc Sealy. *Photoinduced oxygen-consumption in melanin systems - action spectra and quantum yields for eumelanin and synthetic melanin.* Photochemistry and Photobiology **39**, 69–74 (1984).

248. S. L. Jacques and D. J. Mcauliffe. *The Melanosome - Threshold Temperature For Explosive Vaporization and Internal Absorption-coefficient During Pulsed Laser Irradiation.* Photochemistry and Photobiology **53**, 769–775 (1991).

249. S. L. Jacques, R. D. Glickman and J. A. Schwartz. Internal absorption coefficient and threshold for pulsed laser disruption of melanosomes isolated from retinal pigment epithelium. (1996).

250. N Kollias and A Baqer. *Spectroscopic characteristics of human melanin invivo.* Journal of Investigative Dermatology **85**, 38–42 (1985).

251. G. Zonios, J. Bykowski and N. Kollias. *Skin melanin, hemoglobin, and light scattering properties can be quantitatively assessed in vivo using diffuse reflectance spectroscopy.* Journal of Investigative Dermatology **117**, 1452–1457 (2001).

252. George Zonios, Aikaterini Dimou, Ioannis Bassukas, Dimitrios Galaris, Argyrios Tsolakidis and Efthimios Kaxiras. *Melanin absorption spectroscopy: new method for noninvasive skin investigation and melanoma detection.* Journal of Biomedical Optics **13** (2008).

253. Renato Marchesini, Aldo Bono and Mauro Carrara. *In vivo characterization of melanin in melanocytic lesions: spectroscopic study on 1671 pigmented skin lesions.* Journal of Biomedical Optics **14** (2009).

254. M. Wolf, M. Ferrari and V. Quaresima. *Progress of near-infrared spectroscopy and topography for brain and muscle clinical applications.* Journal of Biomedical Optics **12**, 062104 (2007).

255. A. P. Gibson, J. C. Hebden and S. R. Arridge. *Recent advances in diffuse optical imaging.* Physics in Medicine And Biology **50**, R1–R43 (2005).

256. P. Rolfe. *In vivo near-infrared spectroscopy.* Annual Review of Biomedical Engineering **2**, 715–754 (2000).

257. M. Ferrari, L. Mottola and V. Quaresima. *Principles, techniques, and limitations of near infrared spectroscopy.* Canadian Journal of Applied Physiology-revue Canadienne De Physiologie Appliquee **29**, 463–487 (2004).

258. F. F. Jobsis. *2-photon Laser Scanning Fluorescence Microscopy.* Science **198**, 1264–1267 (1977).

259. G. Strangman, J. P. Culver, J. H. Thompson and D. A. Boas. *A quantitative comparison of simultaneous BOLD fMRI and NIRS recordings during functional brain activation.* Neuroimage **17**, 719–731 (2002).